University of Twente

Faculty of
Science and Technology

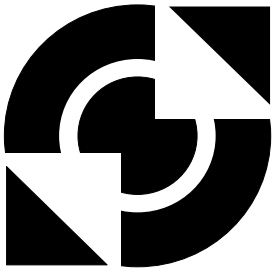

Development of an Experimental Method to Investigate the Hydrodynamics in a Fluidized Bed using PIV and DIA

I. Roghair

Enschede, May 2007

Development of an Experimental Method to Investigate the Hydrodynamics in a Fluidized Bed using PIV and DIA

Fundamentals of Chemical Reaction Engineering

Faculty of Science and Technology

University of Twente

D-Committee

Chairman:	Prof. dr. ir. J.A.M. Kuipers
Mentor:	Ir. J.A. Laverman
CT-i Mentor:	Dr. ir. B.H.L. Betlem
Members:	Dr. ir. M. van Sint Annaland
	Dr. ir. G.B. Meier (Basell)
	Ir. W. Godlieb

Ivo Roghair

D-Colloquium:
May 25th, 2007, 15.00u.

Abstract

An experimental investigation has been performed, studying bubble phase and emulsion phase behavior in a gas-solid fluidized bed using non-invasive optical techniques. The fluidized bed setup, consisting of two pseudo-2D beds, was operated at various conditions, varying both the bed aspect ratio and the superficial gas velocity. The bed consists of Geldart B glass beads. Experiments were performed by recording images of the bed with a high-speed camera. The images were analyzed by commercial (PIV) and in-house developed software (DIA).
Particle Image Velocimetry has been used to analyze the behavior of the emulsion phase. A method has been implemented to verify that the image recording scheme yielded reproducible time-averaged flow patterns. Also, a vector field stitching program was delivered. In addition, a method is developed to correct for raining particles through bubbles, which severely influence the time-averaged emulsion phase flow pattern. The correction algorithm showed an obvious upward particle flow, whereas the raw PIV results barely yielded any upflow of particles at all. Even after correction, upflow of particles is less pronounced than the downflow. Adaptations of the correction algorithm have been proposed to solve this issue.
Corrected time-averaged emulsion phase flow patterns were obtained at 28 different operating conditions. It was shown that the upflow of particles is found along the bubble path, from the lower wall region to the top-center region in the bed. The velocity of the particles increased severely with increasing gas flow.
A Digital Image Analysis (DIA) algorithm has been developed, capable of measuring bubble properties from an image series. The program was validated and yields accurate and reproducible results.
The DIA program was used to investigate relations for bubble size, velocity and aspect ratio. A theoretical relation, predicting the bubble diameter in a pseudo-2D bed was adapted to include the bed width. The velocity of the bubbles in a pseudo-2D bed can be described as $u_b = K_B\sqrt{gd_b}$, in which K_B is a value between 0.6 and 0.7. Moreover, a relation between the bubble aspect ratio and the rise velocity has been observed.
An attempt has been made to describe the bubble-particle phase interaction. By accounting for the average bubble rise velocity, diameter, aspect ratio and frequency of bubbles, it was shown that the trend of the lateral velocity distribution at a single height of the emulsion phase can be predicted. More studies are required to adapt the proposed correlation to yield the expected absolute emulsion phase velocity.

Voorwoord

Na zeven jaar studie ligt hier het verslag van mijn afstudeeropdracht. Iets meer dan een jaar geleden begon ik met veel enthousiasme bij de vakgroep FCRE aan een onderzoek naar gefluïdiseerde bedden. Ik heb met veel plezier bij de groep gewerkt, onderzocht gepokerd en geborreld, en ben dus ook van plan dat te blijven doen.
Het afgelopen jaar is er een hoop veranderd. Veel van mijn vrienden zijn afgestudeerd, en zijn verspreid over het land. Mijn vriendin woont nu in het westen, en ikzelf ga nu ook echt op mezelf wonen. Ook ik heb mij moeten beraden op wat ik nou 'later' wil gaan doen, omdat later naderde. Hier heb ik het met heel veel mensen over gehad, en in de eerste plaats wil ik hen bedanken dat ik met mijn gezeur bij hen terecht kon.
Daarnaast wil ik graag de mensen bedanken die mij hebben geholpen om iets moois van mijn afstuderen te maken. Van Christiaan heb ik veel nuttige tips gekregen over het reilen en zeilen met de PIV opstelling. Willem stond altijd klaar als ik extra resources op het computercluster nodig had en de kennis van Wouter met betrekking tot programmeren heb ik ook goed kunnen gebruiken. Wim heeft superwerk gedaan door de camerastandaard te maken, en tevens omdat hij de door mij gesloopte kolom weer heeft gerepareerd. Bij Niels kon ik ook altijd aankloppen, die het elke keer voor elkaar kreeg om mijn vragen heel helder uit te leggen. Martin wil ik bedanken omdat hij mij na mijn stage heeft gewezen op de mogelijkheden van afstuderen bij FAP. Ook Hans ben ik erkentelijk dat ik de opdracht hier kon uitvoeren. Tevens wil ik alle commissieleden bedanken voor hun ideeën en de discussies die we hebben gevoerd.
Jan Albert wil ik heel erg bedanken voor de gezelligheid, advies en begeleiding gedurende het project. Naast het feit dat je prima gezelschap op borrels bent, heb je me ook enorm geholpen door zoveel teksten van mij te corrigeren. En vele zelfs meerdere malen, waarin je de zaken die ik niet had verbeterd stug nog een keer aanstreepte.
Met dit verslag en de komende presentatie rond ik als het goed is ook mijn studie Chemische Technologie af. Het leven in Enschede was een geweldige tijd, en dat is te danken aan een groot aantal mensen.
Beste vrienden, door jullie zijn de afgelopen zeven jaar onvergetelijk! Vakanties, borrels, studiereis, feesten en wijnproefavonden. Jullie zijn toppers, bedankt!! Martin en Bas wil ik hier trouwens nog even uitlichten. Jullie zijn een stelletje toffe knullen, en ik zal onze idiote gesprekken en het –zo mogelijk– nog vreemder aangeklede huis erg missen.
Er is één iemand die mij met haar lach weer uit een dip kan halen, die me verteld wanneer ik moet stoppen met werken, waarmee ik al mijn geluksmomentjes deel en waarbij ik mijn hart kan uitstorten. Lieve Suzanne, dank je wel voor al deze geweldige momenten!
Bovenal mag ik me gelukkig prijzen met mijn ouders. Naast natuurlijk de financiële steun gedurende mijn studie, waar ik erg dankbaar voor ben, ben ik ook heel blij met de vaste thuisbasis in Zoetermeer waar ik altijd kan aankloppen. Bedankt voor jullie support de afgelopen jaren, voor de adviezen en gesprekken die we hebben gehad, en voor de motivatie die ik soms nodig had. Jullie zijn wereldouders!

Ivo Roghair,
Enschede, May 22, 2007.

Contents

Symbols and Abbreviations

Symbols		
A_0	Catchment area	m^2
A_b	Aspect ratio of a bubble	—
A_{bed}	Cross sectional area of the bed	m^2
AF	Acceleration factor	—
Ar	Archimedes number	—
c	Proportionality constant (~ 2)	—
d_{32}	Sauter mean diameter	m
d_b	Bubble diameter	m
$d_{b,0}$	Initial bubble diameter	m
$d_{b,max}$	Maximum bubble diameter	m
d_p	Particle diameter	m
d_{bed}	Bed diameter / width	m
d_x, d_y	Horizontal, vertical span of a bubble	m
d_v, d_s	Volume, surface diameter	m
f_b	Bubble frequency	s^{-1}
f_t	Fraction of tracer particles ($\equiv 1$)	—
F_I	In-plane particle loss correction factor	—
F_O	Out-of-plane particle loss correction factor	—
F_T	Parameter for particle shape	—
F_Δ	Velocity gradient in interrogation area	—
g	Gravitational constant	$m{\cdot}s^{-2}$
h, h_{bed}	Fixed (unfluidized) bed height	m
i	Position on digital image	px
I	Intensity matrix	—
I', I''	First, second image	—
$\langle I \rangle$	Overall/Average image intensity	—
j	Position on digital image	px
k	Position on digital image	px
K_B	Bubble rise velocity constant	—
ℓ	Emulsion phase velocity vector (identical to $\mathbf{u}$	$m{\cdot}s^{-1}$
M	Conversion factor px $\longrightarrow$ mm	$mm{\cdot}px^{-1}$
n	Number of bubbles, number of classes	—
N	Interrogation zone size	px
N_1, N_2	Position of bubble nose	—
N_f	Number of vector fields	—
N_I	Number of particles in interrogation area	—
N_x, N_y	Total number of pixels in horizontal, vertical direction	px
P	Perimeter	m
r	Lateral or radial position	m

Symbols *(continued)*

r_a	Range for local average	px
$r_{b,2D/3D}$	2D, 3D radius of bubble	m
$\hat{R}$	Correlation peak	—
R_D	Displacement peak	—
S_b	Surface of bubble in a pseudo-2D bed	m^2
SF	Collin's Size Factor	—
t	Pseudo-2D bed thickness	m
T	Threshold intensity	—
u_0	Superficial gas velocity	$m{\cdot}s^{-1}$
u_b	Bubble rise velocity	$m{\cdot}s^{-1}$
$u_{g,p}$	Gas velocity through the particle phase	$m{\cdot}s^{-1}$
u_{mb}	Minimum bubble superficial gas velocity	$m{\cdot}s^{-1}$
u_{mf}	Minimum fluidization gas velocity	$m{\cdot}s^{-1}$
u_p	Predicted particle velocity	$m{\cdot}s^{-1}$
u_z	Vertical particle phase velocity	$m{\cdot}s^{-1}$
$\mathbf{u}$	Bubble velocity vector	$m{\cdot}s^{-1}$
x, z	Lateral, Axial position	px, mm
x_c, y_c	Average horizontal, vertical displacement	px
z	Vertical position above distributor	m

Greek Symbols

ε^*	Binary porosity matrix	—
ε_m	Porosity of a fixed bed	—
ε_{mf}	Porosity at minimum fluidization gas velocity	—
$\varepsilon_{2D,3D}$	Porosity in a pseudo-2D / 3D bed	—
ϕ_s	Sphericity factor	—
$\phi_{v,b}$	Volumetric bubble flow, Visible bubble flow	$m^3{\cdot}s^{-1}$
λ	Bulk viscosity	$kg{\cdot}m^{-1}{\cdot}s^{-1}$
μ_g	Gas viscosity	$kg{\cdot}m^{-1}{\cdot}s^{-1}$
ψ	Ratio between observed bubble flow and excess gas flow	—
ρ_g	Density of gas	$kg{\cdot}m^{-3}$
ρ_p	Density of particle	$kg{\cdot}m^{-3}$
σ	Standard deviation	—
ϑ	Wall influence parameter	—
θ_d	Angle between leading and trailing bubble	°

Abbreviations

DBM	Discrete Bubble Model
CARPT	Computer Aided Radioactive Particle Tracking
DIA	Digital Image Analysis
DPM	Discrete Particle Model
CRiB	Counter Raining in Bubbles
FBR	Fluidized Bed Reactor
GB	Glass Beads
MFC	Mass Flow Controllers
PE	Polyethylene
PEPT	Positron Emission Particle Tracking
PIV	Particle Image Velocimetry
RMS	Root Mean Square
SMD	Sauter Mean Diameter
TFM	Two-Fluid Model
VIA	Validation of Image Acquisition sequence

Chapter 1

Introduction

In this chapter, first the basic principles of fluidization will be discussed. Then, the use of fluidization in industry is outlined, followed by the scope of the project. The last section of this chapter defines the goals of this project.

1.1 Gas-Solid Fluidization

Fluidization is a phenomenon transforming a fixed bed of particles, which has static behavior, to a dynamic state. This is done with an upward fluid flow through the bed. In industry, fluidization is performed in Fluidized Bed Reactors (FBR). These are used in a wide field, e.g. for the polymerization of olefins, drying of starch and combustion of coal, but even the cinema popcorn machine uses the principle of fluidization[1;2]. A particle system in fluidized behaves like a liquid. For example, the surface remains horizontally when the bed is tilted, and objects with a higher density than that of the bed sink into the bed.
Fluidized bed reactors show an excellent mass and heat transfer due to rapid mixing of the particles. Therefore, it is often used in large scale operations. Moreover, it responds slowly to changes in temperature and provides an excellent gas-solid contact.
Its disadvantages are nonuniform particle residence time, erosion of the vessel and internals due to the solid phase and a low gas conversion rate[3].
In this thesis, gas-solid fluidization is considered. Gas is distributed over the column in which the particle bed is present. Although depending on the process, this is normally done by a bottom plate with gas inlets distributed over the surface of the distributor. The particles experience a drag force induced by the gas flow. At low gas flow rates, the gas flows through the interstitial volume between the particles (packed bed state, figure 1.1a). Increasing the superficial gas velocity makes the particles to move further apart; the bed expands as the voidage between the particles grows larger. Bed expansion continues until the gas flow rate reaches a certain value. When the gravitational force equals the drag force of the gas on the particles, particles start to float (figure 1.1b). This gas flow rate is called the minimum fluidization gas velocity, u_{mf}.
At gas flow rates above u_{mf}, bubbles start to form above the distributor as shown in figure 1.1c. The bubbles rise through the particle phase due to the buoyancy force. Bubbles grow larger while rising due to gas entrainment and coalescence. Depending on the particle classification, bubbles may also break-up. The existence of bubbles in a fluidized bed causes mixing of the particles. The bubbles induce a stirring action and convective particle transport through the bed. More on this topic will be discussed in chapter 2.
Different forms of fluidization are known. Increasing the gas flow beyond minimum fluidization velocity results in a bubbling fluidized bed. However, if the column size causes

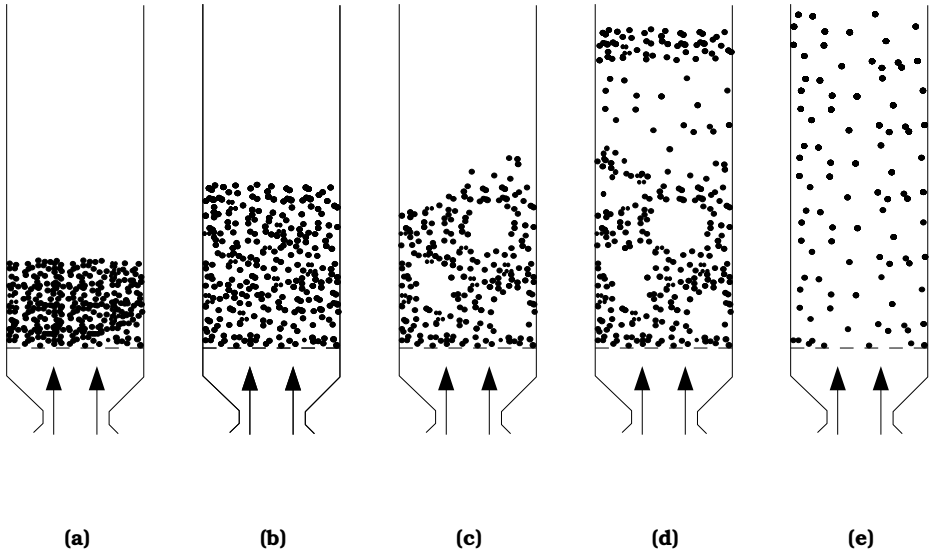

Figure 1.1: **(a)** Fixed bed state **(b)** Expanded bed at minimum fluidization gas velocity **(c)** Bubbling fluidized bed **(d)** Slugging regime **(e)** Entrainment of particles[3]

the bubbles to be restricted by the walls, another regime is reached, called slugging (figure 1.1d). The wide bubbles reach almost from wall to wall, while particles mainly rain down the wide bubbles. Entrainment of particles by the gas flow is shown in figure 1.1e. This work investigates the bubbling fluidization regime.

1.2 Project Scope

Gas-solid fluidized beds are widely employed in the (petro) chemical industry. This research is performed in the scope of polymerization reactor systems. Together with the liquid slurry process and the solution process, the fluidized bed process is commonly used. An example of a gas phase olefin polymerization process is the so-called UNIPOL^{TM} process, depicted in figure 1.1. The gas phase polymerization process produces polyethylene (PE) with large ranges of both product densities and molecular weight distribution[4]. Monomer gas is fed trough the bottom of the column, fluidizing the polymer particles and acting as a reagent. Heat removal is an important issue for this process, because the polymerization reaction is highly exothermic and the temperature should not exceed the melting point of PE. The produced heat is transported through the reactor by solids mixing (convective heat transport), and can be removed by emerging gas and cooling at the walls. Alternatively, it is possible to remove heat by operating FBR in condensed mode, i.e. the monomer is partly added to the reactor as a liquid, which is evaporated by the heat of the polymerization reaction. Despite this solution, heat transfer through the solids phase is a key factor to further improve heat removal. Insight in the macroscopic circulation patterns will be beneficious for a higher efficiency heat removal, and therefore the production can be optimized.
One way to obtain information on the detailed behavior of fluidized beds is modelling the particle- and gas phase behavior. In the field of computational fluid dynamics, large steps are made in the creation of a model which predicts industrial scale fluidized bed behavior. Apart from its industrial relevance, these models provide a fundamental understanding of the different phenomena in the fluidized bed reactor. Despite the enor-

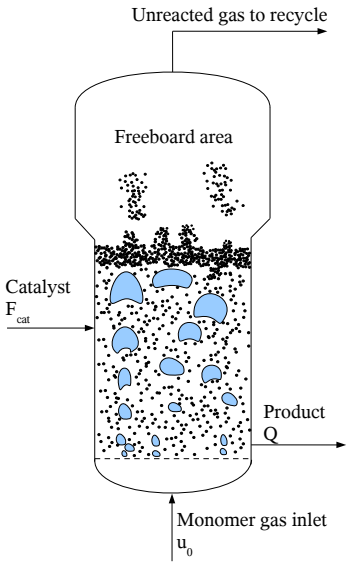

Figure 1.2: UNIPOL^{TM} process[4]

mous progression in computing power, models of a full-scale reactor predicting the flow in the smallest detail are still outside limits. However, closure relations of the detailed flow structures can be obtained by small-scale simulations, and provided to large-scale models.
Different approaches of modelling the two-phase flow are therefore performed. At the highest detail level, lattice-Boltzmann simulations are performed to provide closure relations for the drag force of the gas on the particles[5]. Small systems can be simulated in the Discrete Particle Model (DPM), which is used to model the trajectories of individual particles by Newton's second law of motion (e.g. Van Der Hoef *et al.*[6]). Particles are the discrete entities, through which the gaseous phase flow is solved using the volume-averaged Navier-Stokes equations. A larger scale approach involves modelling of the particle phase as a continuum. A Two-Fluid Model was designed by Kuipers *et al.*[7], considering the particle phase and the gaseous phase as interpenetrating Newtonian fluids. A Discrete Bubble Model (DBM) of a bubble column was adapted to model fluidized bed hydrodynamics[4;8]. In this model, the bubbles are modelled as the discrete entities which can collide and coalesce. The particle phase flow is solved using the Navier-Stokes equations.
In order to validate the models, experiments must be performed to verify the hydrodynamics predicted by the models with experimental data. The qualitative flow pattern of the particle phase is already known, but quantitative information on particle phase flow is still scarce. The interaction between the two phases has also not been quantified yet. Raising the question, what influence bubble movement has on the particle phase.

1.3 Project Goals

To improve our understanding of macroscopic circulation patterns of the particulate phase and the coupling between the two phases, a thorough investigation on both particle and bubble phase is required. Experiments are performed using Particle Image Velocimetry (PIV), used to obtain time-averaged circulation patterns of the particle phase. Parameters of interest here are the superficial gas velocity and bed aspect ratio.

The flow patterns can be used to obtain the particle flow through the bed in axial and lateral directions.
Bubble behavior and the influence of the bubbles on the particle phase is investigated using a newly developed computer program. This program detects bubbles and extracts bubble properties from images of a pseudo-2D fluidized bed. Bubble properties of primary interest are position, size and velocity.
The project goals can be summarized into the creation and combination of two non-invasive analysis techniques (PIV and DIA) to study particle and bubble behavior in a pseudo-2D fluidized bed simultaneously. The focus will lay on understanding these phases and their influence on each other.

Chapter 2

Theory

2.1 Introduction

This project focuses on obtaining fundamental information on the hydrodynamics of the emulsion phase, the behavior of the bubble phase and bubble-emulsion phase interaction in a bubbling gas-solid fluidized bed. Literature available on these subjects will be discussed here.
Two parts can be distinguished in this chapter. The first part discusses parameters which influence the emulsion phase behavior, followed by an outline of the experimental method (PIV) used to measure the hydrodynamics of the emulsion phase. The second part concerns correlations predicting the behavior of the bubble phase. Consequently, a method to experimentally acquire bubble phase behavior non-invasively (DIA) is discussed. At the end of this chapter a short outline on 2D - 3D conversion is given.

2.2 Emulsion phase behavior

2.2.1 Hydrodynamics

The particulate phase in a bubbling fluidized bed can be considered as a flowing continuum. The flow is induced by bubble movement. In the wake behind a bubble, particles are dragged upward along the bubble path as shown in figure 2.1a. Particles stream down along the sides of the bubble. Because bubbles mainly form at the lower wall region and have the tendency to move towards the center of the bed as they rise, the main upward flow of particles is expected between the core and the wall region.
Various flow patterns have been defined for different bed aspect ratios and superficial gas velocities. For example, it is stated[3] that at low gas flow rates and shallow beds, particles flow upward along the wall and down through the center of the bed. This pattern is reversed at higher gas flow rates and aspect ratios which approach unity. Moreover, in deep beds a second vortex ring emerges which, especially at high gas flow rates, dominates the overall particle circulation pattern[1;3;9]. This pattern can be found in figure 2.1b.

Particle classification

In 1973, Geldart[10] proposed a method to classify particles based on their size (diameter, d_p) and the difference between the density of the gas and the particles, $(\rho_p - \rho_g)$, based on experimental data. Four groups are distinguished, conveniently named Geldart A, B, C and D particles, which are displayed in figure 2.2.1. Particles of class C are cohesive powders, and are difficult to fluidize due to the strong interparticle force.

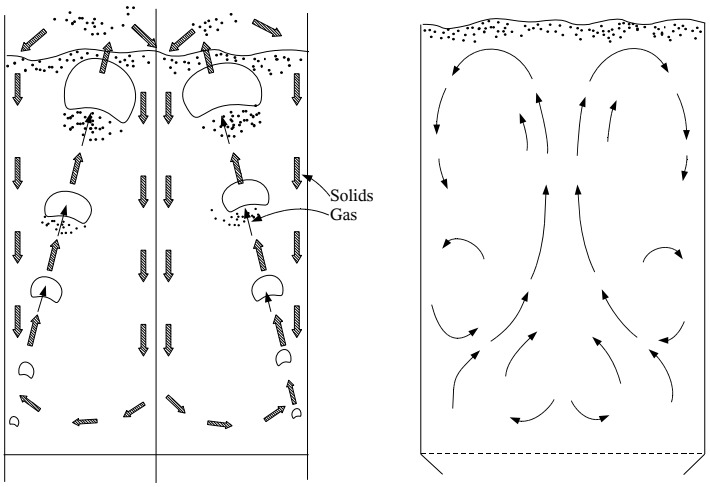

Figure 2.1: **(a)** The path of the bubbles starting at the walls and moving towards the center of the bed, hereby taking the particles upward along their path. The emulsion phase downflow can be found in the center and at the walls of the bed. **(b)** The general particle flow pattern in deep beds. From Kunii and Levenspiel (1991)[3]

Channeling of gas is likely to occur in these particle systems. Class A consists of small and/or low density particles. They are easily fluidized. Geldart B particles are sand-like, and are also easy to fluidize. The main difference between class A and B particle types is that bubbles in Geldart A particle systems are restricted in their size due to break-up. The largest particles are grouped as Geldart D particles, which are difficult to fluidize, particularly in deep beds[3;10].
Besides, the gas flow through bubbles is different in these particle systems. In Geldart A and B particles, gas flow through the bubbles circulates and forms a cloud around the bubbles. In Geldart D systems, the gas mainly goes through the bubbles, and flows upward.
The scope of this project comprises olefin polymerization reactors, in which the particle size depends on the residence time of a catalytic particle in the reactor. Particles in these types of reactors range typically from 0.25 to 1.0 mm[1]. The polyolefin particles are therefore mainly found in the Geldart B region.
The minimum fluidization gas velocity depends strongly on the chosen particles. To calculate the minimum fluidization velocity u_{mf}, the following relation is proposed in Kunii and Levenspiel (1991)[3;11]:

$$u_{mf} = \left(\frac{\mu_g}{\rho_g d_p}\right)\left(\sqrt{(27.2)^2 + 0.0408Ar} - 27.2\right) \tag{2.1}$$

where the Archimedes number Ar is defined as:

$$Ar = \frac{d_p^3 \rho_g (\rho_p - \rho_g) g}{\mu_g^2} \tag{2.2}$$

In this project, u_{mf} is determined experimentally in a pseudo-2D bed by a pressure drop experiment. This is discussed in section 4.2.4.

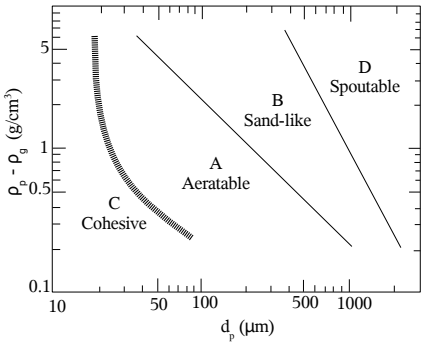

Figure 2.2: The Geldart classification of particles for air at ambient conditions (from Kunii and Levenspiel (1991)[3].

Particle Tracking

The measurement of emulsion phase flow in a fluidized bed can be performed with particle tracking techniques. These techniques are non-intrusive, and can be performed in relatively large 3D beds. Positron Emission Particle Tracking (PEPT) and Radioactive Particle Tracking (RPT) methods are most often used in this respect. In RPT, a γ-ray emitting particle is followed through the emulsion phase in three direction by γ-ray detectors. PEPT uses particles which emit positrons due to β-decay. When a positron and an electron meet, they annihilate and convert their masses into energy, which is released by electromagnetic radiation. Two γ-rays are emitted almost exactly back-to-back. The trajectory is called the annihilation vector. If two γ-rays are detected within the resolving time window, this vector is determined. The particle is positioned at the intersection of several vectors.
Apart from its radioactive properties, a tracer particle is identical to the other particles in the bed. By recording the trajectory of the particle, time averaged results can be obtained, as well as the fluctuations in particle position in relatively large setups. However, instantaneous total flow behavior cannot be studied, as only a single particle is labelled[12]. Stein *et al.*[13] performed PEPT experiments in cylindrical beds with Geldart B particles. They found ascending particles in the core region, downflow at the wall region and particles in the bubble trajectory, move both up and downward. They also mention that the average emulsion phase upward velocity is about half of the bubble velocity, independent of the superficial gas velocity. This conclusion however, is based on the calculated bubble velocity and diameter, using theoretical equations.
This result was confirmed by Mostoufi and Chaouki[14]. They performed RPT experiments in order to investigate particle flow structures in a fluidized bed, and they too found ascending particle clusters in the center of the bed, whereas descending clusters were mostly found in the wall region. The authors also related emulsion phase motion to the velocity of a rising bubble. It was noted that particles in the wake of the bubble ascend proportional to the velocity of the bubble. The bubble velocity however, was not measured directly, but rather obtained from theoretical relations.

The hydrodynamics of the emulsion phase, and parameters of influence, were discussed in this section. Particle tracking experiments are able to visualize aspects of particle phase flow in a non-intrusive way. Bubble properties, necessary to classify the interaction between the phases, are often obtained with relations from literature.

2.2.2 Particle Image Velocimetry

Particle Image Velocimetry (PIV) is an experimental method to obtain instantaneous macroscopic flow patterns of a system. PIV is a non-intrusive, optical technique, originally developed to study flows in liquid or liquid-gas systems. These systems usually work with tracer particles that are injected in the flow of interest. In this case, PIV is performed to study the flow of the emulsion phase, first performed by Bokkers[4] and later by Link[15]. In the case of PIV on granular media, tracer particles are not always needed as the particles themselves are being tracked[16–18]. A drawback of using an opaque system such as a fluidized bed, is that visual access can only be obtained at the wall. Hence, a pseudo-2D bed is required to measure the macroscale circulation patterns in the fluidized bed.
The emerging instantaneous patterns can be used to obtain the time-averaged particle circulation pattern through the whole bed. In addition, instantaneous flow fields can be used to gain detailed insight in other complex phenomena, such as the flow around rising bubbles. In this project, PIV calculations are performed using DaVis software from LaVision. This section covers the basics of PIV. Appendix A discusses design rules that have to be taken into account, which are specified in literature.
The basic principle of PIV consists of spatial cross-correlation of two consecutive images. Thereby an instantaneous flow pattern is obtained of the entire photographed area. To obtain good resolution, the images are divided in so-termed interrogation zones. For each interrogation zone, individual correlation between the two images is performed. An example is given in figure 2.3a, where a pattern on the first image (solid area) is compared to three equal sized areas on the second image (the solid, dashed and fine-dashed areas). This results in spatial cross-correlation peaks (figure 2.3b) for every interrogation zone. The highest value indicates the most likely displacement of that particular interrogation zone. There are several parameters that influence the displacement peak $R_D(x, y)$:

$$R_D(x,y) = N_I \cdot F_I(x,y) \cdot F_O \cdot F_T(x,y) \cdot F_\Delta(x,y) \tag{2.3}$$

PIV only determines the movement in a 2D plane. Therefore, particles moving out of the plane (i.e. perpendicular to the field of view, F_O) and particles moving out of the interrogated area parallel to the field of view ($F_I(x, y)$) account for a loss of correlation. The error caused by these parameters can be minimized by decreasing the delay between the two images. The shape of the peak is influenced by the shape of the particles ($F_T(x, y)$) and the velocity distribution in the interrogation zone ($F_\Delta(x, y)$). The spatial cross-correlation of the images is calculated with equation 2.4.

$$\hat{R}\,[x,y] = \frac{1}{N_x N_y} \sum_{i=1}^{N_x} \sum_{j=1}^{N_y} \left(I'[i,j] - \langle I \rangle\right) \left(I''[i+x, j+y] - \langle I \rangle\right) \tag{2.4}$$

Note that the overall image intensity $\langle I \rangle$ is subtracted from both images before cross-correlation takes place. This reduces the background correlation.
Obviously, PIV can only be used to obtain information on particle phase flow. The coupling between the two phases is accomplished by separate measurements to investigate the bubble phase flow under identical conditions. Analogue to the discussion of the particle phase, the next sections will outline bubble phase behavior, followed by a description of the measurement method.

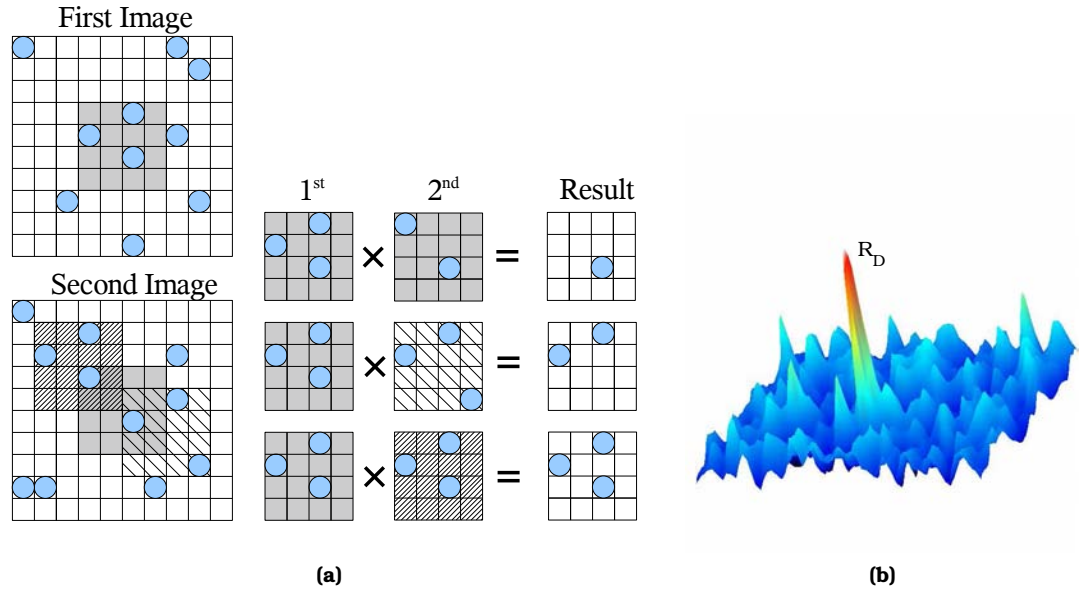

Figure 2.3: **(a)** correlation of two images using a 4x4 interrogation area. Three correlation instances are shown, of which the bottom window shift shows the most likely particle relocation. **(b)** spatial cross-correlation plot. The most likely displacement is given by the high peak, called the dislocation peak R_D.

2.3 Bubble behavior

2.3.1 Gas phase transport

When the superficial velocity is raised above the minimum bubble superficial gas velocity u_{mb}, bubbles start to form just above the distributor. In the case of Geldart B particles, u_{mb} is found at a superficial gas velocity u_0 slightly exceeding the minimum fluidization velocity. At these conditions, bubbles start to form, causing circulation patterns of the solids[3]. On average, bubbles move as depicted in figure 2.1a, from the lower wall regions towards the center of the bed as they rise.
The two-phase theory of fluidization states that the excess gas flow, i.e. $(u_0 - u_{mf})$, is visible as rising bubbles. The observed bubble flow ratio to the two-phase expected bubble flow can be expressed as:

$$\psi = \left(\frac{\text{observed bubble flow}}{\text{excess flow from 2 phase theory}} \right) = \frac{\phi_{v,b}}{(u_0 - u_{mf})\, A_{bed}} \tag{2.5}$$

However, numerous experiments have shown that the observed bubble flow is less than the excess flow. Hence, the transport of gas through the bed must be described by additional means besides bubbles. Geldart[19] proposes three mechanisms by which the gas moves through the bed; interstitial gas flow through the particle phase, gas flow by the rising bubbles and superimposed gas flow through bubbles. Gera *et al.*[20] have investigated the through flow of gas between two interacting bubbles. They also found that the path between two bubbles taken by the gas has a lower porosity than elsewhere in the bed, which is attributed to the superimposed gas flow. For Geldart B particles and $h/d_{bed} \cong 1$, the ratio of eq. 2.5 is therefore not 1, but is rather determined at $\psi = 0.65$[1;3].

2.3.2 Bubble properties

Several relations have been proposed to describe bubble properties in a fluidized bed. Besides its size, the velocity of a bubble can be predicted, as well as parameters which define the shape of a bubble.

Bubble size

Bubbles grow due to gas entrainment and coalescence. Bubbles shrink due to gas leakage and break up. Bubble size and growth depend strongly on the particle type that is used. Using very small particles restricts the maximum size of the bubbles rigorously (the roof collapses in small particle systems), whereas bubbles in Geldart B and D particle systems seem to grow without limits[3].
The bubble diameter is commonly expressed as the equivalent diameter of a spherical bubble (for 3D beds) or a circular shape (in pseudo-2D systems). A number of correlations are found in literature to describe the bubble diameter d_b in a fluidized bed[3;11;21]. The Darton relation gives the bubble diameter as a function of the height above the distributor plate:

$$d_b = 0.54\,(u_0 - u_{mf})^{0.4}\left(z + 4\sqrt{A_0}\right)^{0.8} g^{-0.2} \tag{2.6}$$

in which $4\sqrt{A_0} = 0.03$ m for a porous plate. This correlation is derived for 3D fluidized beds and Geldart B particle types. Mori and Wen describe bubble growth as[3;11]:

$$d_b = d_{b,max} - (d_{b,max} - d_{b,0}) \cdot e^{\frac{-0.3z}{d_{bed}}} \tag{2.7a}$$

in which the maximum bubble diameter $d_{b,max}$ can be calculated with eq. 2.7b:

$$d_{b,max} = 0.65\left[\frac{\pi}{4} d_{bed}^2\,(u_0 - u_{mf})\right]^{0.4} \tag{2.7b}$$

and the initial bubble diameter $d_{b,0}$ above a porous plate distributor is expressed as:

$$d_{b,0} = 0.376\,(u_0 - u_{mf})^2 \tag{2.7c}$$

Alternatively, the Hilligardt-Werther correlation is described as followed:

$$d_b = d_{b,0}\,(1 + 27\,(u_0 - u_{mf}))^{1/3}\,(1 + 6.4z)^{1.2} \tag{2.8}$$

where $d_{b,0} = 0.0085$ for Geldart B particles in a 3D bed[21]. Lim *et al.*[22] suggest:

$$d_b = \left[\frac{8\,(u_0 - u_{mf})\left(2^{3/4} - 1\right)}{\pi c g^{1/2}} z + d_{b,0}^{3/2}\right]^{2/3} \tag{2.9a}$$

using an initial bubble size of:

$$d_{b,0} = \left[\frac{8\,(u - u_{mf})\,A_0}{\sqrt{\pi\lambda g}}\right]^{2/3} \tag{2.9b}$$

with $A_0 = 5.6 \cdot 10^{-5}$ for a porous plate distributor. The Darton (2.6), Mori-Wen (2.7) and Hilligardt-Werther (2.8) equations are valid for a 3D bubbling fluidized bed. Alternatively, one could use the relation of Shen *et al.*[23]. This relation is valid for a pseudo-2D fluidized bed, and was obtained from DIA experiments. Note that the equation is analogue to the Darton relation with a higher coefficient and different powers. Their experimental data and the proposed relation is given in figure 2.4a. The correlation is given as:

$$d_b = 0.89\,[(u_0 - u_{mf})(z + 3.0A_0/t)]^{2/3}\,g^{-1/3} \tag{2.10}$$

in which t equals the thickness of the pseudo-2D bed.

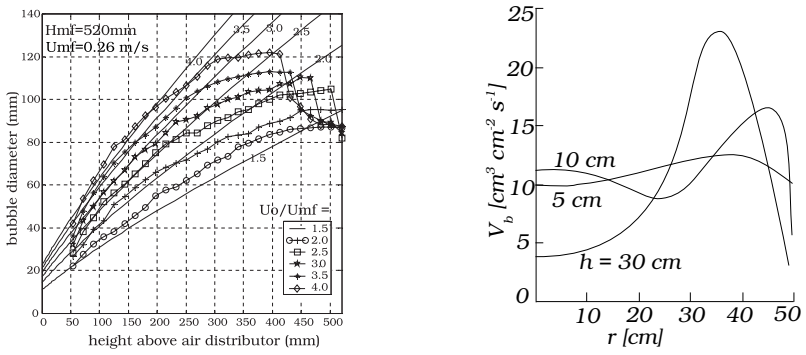

(a) **(b)**

Figure 2.4: (a) The relation of Shen *et al.*[23] fitted to experimental data **(b)** The radial distribution of bubble-gas flow. From Werther (2002)[1].

Bubble Rise Velocity

As bubbles grow, they rise faster through the bed. Depending on the bubble diameter, the terminal velocity of a single unhindered spherical-cap gas bubble can be expressed with the Davies and Taylor expression[3]:

$$u_b = K_B \sqrt{g d_b} \tag{2.11}$$

In 3D beds, the value of the bubble rise velocity constant K_B is commonly set to 0.711. The value for K_B is still under debate for 2D cases. It is reported that $K_B \approx 0.50$ or even 0.41 for 2D bubbles[24;25]. However, also higher constants are obtained, e.g. by Shen *et al.* who derived a value of 0.8 - 1.0[23]. It is found that equation 2.11 describes bubble velocities within a 30% range. The large range is due to breakup and coalescence which alters the bubble diameter significantly[25].
The velocity of a swarm of bubbles can be described with an extended form of the Davies–Taylor expression (eq. 2.11):

$$u_b = (u_0 - u_{mf}) + K_B \sqrt{g d_b} \tag{2.12}$$

In order to account for wall effects, Werther[1] proposed a relation that includes the bed diameter:

$$K_B = 0.71 * \vartheta \tag{2.13a}$$

where:

$$\vartheta = \begin{cases} 3.2 d_{bed}^{0.33} & 0.05 \leq d_{bed} \leq 1\text{m} \qquad \text{for Geldart A particles} \\ \sqrt{2.0 d_{bed}} & 0.1 \leq d_{bed} \leq 1\text{m} \qquad \text{for Geldart B particles} \end{cases} \tag{2.13b}$$

Another way to incorporate wall influences on the bubble rise velocity is to include a size-factor (SF) in the Davies–Taylor relation (2.11), as proposed by Collins (1967)[26]:

$$u_b = K_B \sqrt{g d_b} (SF) \tag{2.14a}$$

which represents the rise velocity of a single, isolated bubble[27]. The size factor decreases as the ratio between the bubble diameter d_b and bed diameter d_{bed} increases:

$$\mathrm{SF} = \begin{cases} 1 & \text{for } \dfrac{d_b}{d_{bed}} < 0.125 \\ 1.13 \exp\left(-\dfrac{d_b}{d_{bed}}\right) & \text{for } 0.125 < \dfrac{d_b}{d_{bed}} < 0.6 \\ 0.496\sqrt{\dfrac{d_b}{d_{bed}}} & \text{for } \dfrac{d_b}{d_{bed}} > 0.6 \end{cases} \tag{2.14b}$$

The velocity of a bubble is also dependent on the presence of other bubbles. Krishna and Van Baten (2001) proposed a relation to include bubble acceleration imposed on a bubble by using the Davies-Taylor-Collins equation (2.14a) as a basis.

$$u_b = u_b^0 \, (AF) = K_B \sqrt{g d_b} (SF)(AF) \tag{2.15a}$$

In this equation AF is the acceleration factor expressed as:

$$AF = 1.64 + 2.7722(u_0 - u_{g,p}) \tag{2.15b}$$

Here, $u_{g,p}$ equals the gas velocity through the particle phase interstitially. It is worth mentioning that the interstitial gas flow apparently does not depend on the size of the bubbles and distance between the bubbles. However, one would expect it based on the superimposed gas flow as discussed by Gera *et al.*[20].

Bubble shape

In A and B types of particles, the shape of a bubble is usually a spherical cap (at atmospheric pressure)[9]. Interaction between bubbles is known to change the properties of a bubble. Besides common bubble parameters such as velocity, direction and size, the shape of a bubble is also distorted as a result of its presence close to another bubble. A tailing bubble accelerates under influence of a leading bubble in the direction of the leader. In this process, the leading bubble is flattened whereas the tailing bubble is elongated in the direction of the leader as a result of increased gas flow in that direction.

The shape of a bubble can be characterized with two different parameters. The first one is the aspect ratio A_b, that can be described by the horizontal and vertical span d_x and d_y, as shown in figure 2.5:

$$A_b = \frac{d_y}{d_x} \tag{2.16}$$

The second shape characteristic parameter is the sphericity factor S. The sphericity is obtained by dividing the circumference of a circle with equivalent diameter d_b by the detected circumference (perimeter) P of a bubble.:

$$S = \frac{\pi d_b}{P} \tag{2.17}$$

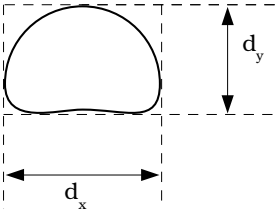

Figure 2.5: Bubble aspect ratio

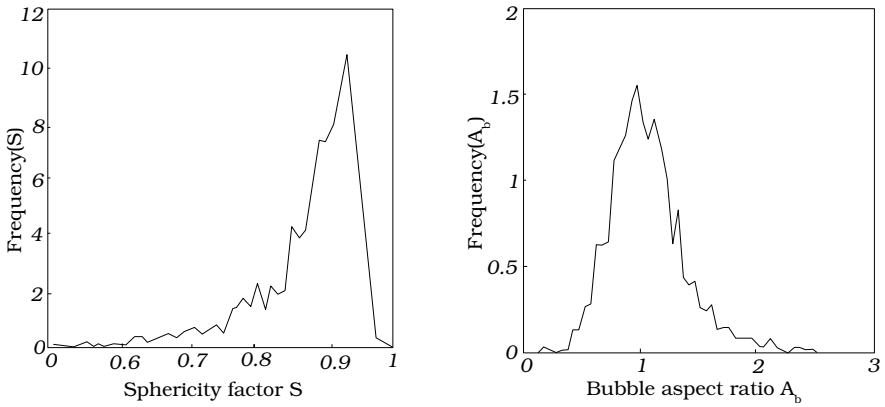

Figure 2.6: **(a)** Sphericity distribution results of Lim *et al.*[28] **(b)** Aspect ratio distribution results of Lim *et al.*[28]

The distribution of these parameters was investigated by Lim *et al.*[28] and Caicedo *et al*[29]. Results of Lim *et al.* are given in figure 2.6. This figure shows that the majority of the bubbles have an aspect ratio of 1, whereas the mean sphericity is found to be about 0.9. These parameters were measured at 10 cm above the distributor plate at a superficial gas velocity of $4u_{mf}$. Caicedo *et al.* however, find lower sphericity values of about 0.7 and aspect ratios mainly above 1. The difference with the work of Lim *et al.* is the superficial velocity, which Caicedo *et al.* set to $1.4u_{mf}$. Apparently, a lower superficial gas velocity gives rise to vertically stretched bubbles. However, this would not be expected as bubble-bubble interaction is more likely to occur in systems with higher superficial gas velocity. Various bubble properties have been discussed in this section. These properties can be investigated by digital image analysis; an algorithm capable of analyzing a series of images in order to extract the information needed. Main issues on digital image analysis algorithms described in literature are outlined in the following section.

2.3.3 Digital Image Analysis

Digital image analysis (DIA) is performed to investigate bubble parameters such as the position, velocity and size from a series of digital images in a freely bubbling pseudo-2D fluidized bed. The obtained data are used to determine relations describing the bubble behavior by statistical analysis.
A DIA program generally obtains an image and preprocesses it. Consequently, it segmentates the two phases (emulsion and bubble phase) by comparing the gray level of every pixel with a threshold value. In a postprocessing step, bubble properties are determined.
The advantage of DIA is that it is capable of measuring at a high resolution, has a potential high degree of automation and the flow pattern is not disturbed by probes or sensors. However, similar to PIV, visual access to the bed is required. Therefore, images are taken from a pseudo-2D fluidized bed.
Pioneers in the field of DIA on fluidized beds are Lim and Agarwal *et al.*[28;30;31]. But also other groups[23;25] have described their algorithm in literature. This section outlines important characteristics of DIA programs described in literature. Of particular interest are the definitions of bubble position and the method of bubble tracking on subse-

quent frames. The development of the DIA software used in this research is described in section 3.2.

Phase segmentation step

Lim and Agarwal *et al.* place the light source behind a pseudo-2D bed. The bubbles they record are therefore seen as light objects, whereas the opaque particle phase is not illuminated. They used a threshold for the segmentation process, which was defined as the minimum between the peaks of a bimodal gray value histogram. For their algorithm, images should have high contrast between the phases and homogeneous lighting. Shen *et al.*[23] determined a constant threshold by analysis of a whole image series. Mudde *et al.*[25] used an adaptive threshold value, determined by analysis of the variation of gray values in the image. They preprocessed the images before segmentation is performed.

DIA postprocessing

The position of a bubble is usually set to the center of gravity and the size (projected area of the bubble) is equivalent to the adjacent bubble pixels. The position of a bubble on subsequent frames is used to measure the velocity. The bubble velocity measurement is based on the shift of the center of gravity between two consequent frames. The displacement of a bubble must be within a predescribed range. If multiple bubbles fulfill this criteria, the smallest positive displacement is used for the velocity measurement[25]. In most cases in literature, a video camera was used, which had a fixed frame rate of 25 fps (frames per second) with a fixed delay between the images of 40 ms or 20 ms. Between 2000[28] and 10000[23] images were used for statistical analysis.
Other parameters, such as the gas hold-up, the aspect ratio and the shape factor were also detected in the algortihms discussed[23;25;30]. As mentioned in section 2.3.2, the distribution of the shape factor and aspect ratio was measured[28;29]. However, the velocity dependence of the aspect ratio is not yet investigated, although it is proposed that the aspect ratio might be of significant influence on the bubble velocity[30]. It was also found that bubbles smaller than the depth of the pseudo-2D bed are not fully visible because they do not stretch from the front to the back wall, as pointed out by Lim *et al.*[28]. Therefore, bubbles that are smaller than the bed depth, are not taken into account.

DIA and PIV are used with images that are obtained from a pseudo-2D fluidized bed. In order to interpretate results for three dimensional reactor systems, the wall effects in a pseudo-2D systems are outlined in the following section.

2.4 Pseudo-2D to 3D

The geometry of a pseudo-2D fluidized bed restricts the multiphase flow in one dimension, which influences the flow behavior. For example, bubbles in a pseudo-2D bed rise slower as compared to identical frontal diameter bubbles in a 3D bed[10;25]. Also, the observed u_{mf} is usually larger for a 2D bed as compared to a 3D bed. In this section, first the effect on the particle phase will be discussed. Then a number of methods are given to convert bubble properties between the two geometries.

Particle phase

Compared to a cylindrical (3D) reactor, a pseudo-2D fluidized bed has a large internal surface area to volume ratio. Using a two-fluid model, Kobayashi *et al.*[32] showed that the circulation of solids in a rectangular bed is similar to the circulation in a cylindrical

bed. Villa-Briongos *et al.*[33] provide a scaling method that is based on deterministic chaos theory. They define a geometry independent Kolmogorov entropy based on fluctuations at the bed surface, under the assumption that these fluctuations provide a measure for the hydrodynamics throughout the entire bed. It was found that for Geldart B and D type particles, the hydrodynamics of 2D and 3D systems are qualitatively comparable.
Concerning the porosity of the particle phase, Link assumes a relation to calculate the porosity in a 3D fluidized bed with data obtained from a pseudo-2D bed by:

$$\varepsilon_{3D} = (\varepsilon_{2D})^{\frac{3}{2}} \tag{2.18}$$

This relation is obtained analytically by assuming that the particle configuration in a 3D bed is equivalent to the particle configuration at the front plate of a 2D bed.

Bubble phase

Predicting the diameter of a bubble in a 3D bed with experimental pseudo-2D data is modelled in several ways. First of all, the Sauter Mean Diameter (SMD) of a pseudo-2D bubble could be used to transform the volume/surface ratio to a spherical bubble. The SMD is defined as:

$$\text{SMD} = \overline{d_{32}} = \sum_i \frac{d_v^3}{d_s^2} \tag{2.19a}$$

in which i is the number of bubbles, d_s is the surface diameter and d_v is the volume diameter. In the case of bubbles in a pseudo-2D bed, it is argued that bubbles are of cylindrical shape, with the 'top' and 'bottom' of the cylinder found at the frontal and back plate. The surface area which is able to expand is the curved surface of this cylinder. The surface diameter d_s can therefore be set to the area allowed to expand through the bed:

$$d_s = \sqrt{\frac{S_b}{\pi}} = \sqrt{\frac{\pi d_b t}{\pi}} = \sqrt{d_b t} \tag{2.19b}$$

in which t equals the depth of the column, and d_b the diameter of the 2D bubble. The volume diameter d_v can now be described as:

$$d_v = \left(\frac{6V_p}{\pi}\right)^{\frac{1}{3}} = \left(\frac{6(\frac{1}{4}\pi d_b^2 t)}{\pi}\right)^{\frac{1}{3}} = \left(1.5 d_b^2 t\right)^{\frac{1}{3}} \tag{2.19c}$$

Geldart (1970)[19] has found that due to out-of-line coalescence, bubbles in a 3D bed typically grow larger than in a 2D bed under comparable conditions. The diameter can be calculated for an idealized case, without accounting for side-wall effects and out-of-line coalescence, with the data obtained from a pseudo-2D fluidized bed using images and probes simultaneously. The bubble concentration in a 2D bed and the point bubble frequency obtained from the probes describe a relation for the bubble concentration in a 3D bed:

$$(n_{3D})_{ideal} = 1.5 \frac{n_{2D}^2}{f_{2D}} \tag{2.20}$$

$$(d_b)_{3D} = \left(\frac{u_g - u_{mf}}{(n_{3D})_{ideal}} \frac{8}{\pi}\right)^{1/3} \tag{2.21}$$

It follows that the number of bubbles in 2D and 3D geometries are related to each other.

This section has shown that information obtained from pseudo-2D could be used to predict 3D bed behavior. The hydrodynamics have been investigated by simulations and by studying the bed surface fluctuations, whereas bubble size can be transformed using the SMD, or by adopting the technique used by Geldart, measuring the bubble number in a certain region and the bubble point frequency measured by a probe.

Chapter 3

Application Development

3.1 Introduction

Several programs have been developed to analyze, validate and post-process the experimental results. The programs are written in the C programming language. This chapter will discuss the development of these program and describe the way they programs work.
First, the development of the Digital Image Analysis (DIA) program is described in section 3.2. DIA is used to analyze digital images of the bed, separate the bubbles from the emulsion phase and determine bubble properties such as size, location and velocity. A post-processing method to correct PIV measurements is proposed in section 3.3. In section 3.4 the Stitch program is discussed. This program combines multiple time-averaged PIV vector plots for cases in which the bed could not be recorded as a whole. In section 3.5, a program is described, which is able to determine if the proposed camera settings for PIV are adequate.
Because of the large amount of programs and methods used in this research, a Data Flow Diagram is given in the final section, presenting the strong interaction between the different programs.

3.2 Digital Image Analysis

Digital Image Analysis (DIA) is widely used to obtain detailed bubble property information in fluidized beds[23;25;28;30;31]. The obtained data, such as size, position and velocity, are used to determine correlations for bubble size, growth and velocity. Besides distinguishing between the bubble and emulsion phase, the program accounts for wall detection and removal, detection of the freeboard and eliminating distortions such as shadows and/or inhomogeneous lighting. In this section the main functions are discussed.

3.2.1 Preprocessing and phase segmentation

The basic function of the DIA program is its capability to separate the emulsion phase and bubble phase. DIA processes images in which the emulsion phase has a higher intensity and bubbles (background) have a lower intensity. The actual separation is performed by an adaptive intensity threshold, i.e. a cutoff value which determines for every pixel whether it represents the bubble or emulsion phase.
Before the separation is performed, the images need to be preprocessed. It was found that after preprocessing, the gray values in the images consist of a bimodal intensity

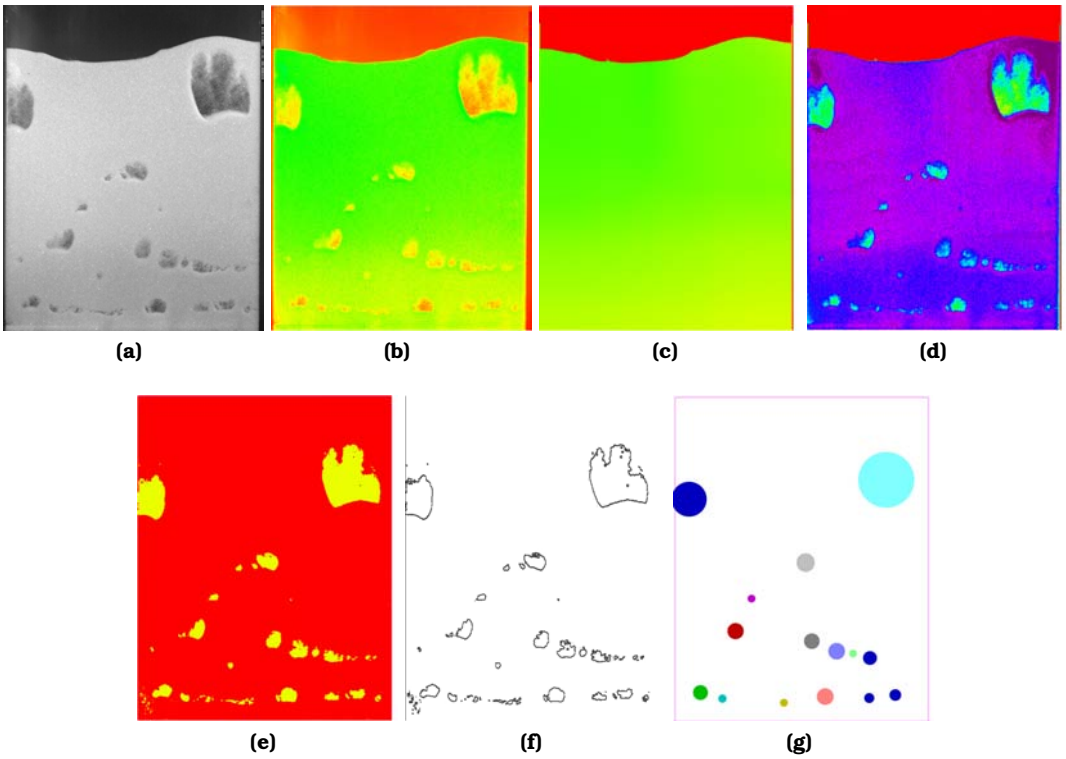

Figure 3.1: **(a)** An example of an original grayscale input image, **(b)** the representation of the image by the program after normalization **(c)** detection of the local average, **(d)** the original image corrected for inhomogeneous illumination **(e)** the binary frame resulting from phase segmentation, **(f)** edge detection to obtain the circumference of a bubble **(g)** representation of the equivalent bubble diameter as circles

distribution, which is necessary for reliable phase separation. Note that, on the contrary to most DIA algorithms described in literature, the light source is not behind the bed, but in front of it. The reason is that the DIA program must also be able to process images obtained for PIV analysis and therefore, it is required that the dense phase is illuminated thoroughly.
DIA starts with importing a bitmap (.bmp) image into an intensity matrix $I_{i,j}$. Color images are transformed to grayscale, and the intensity of the image is normalized to $0.0 \leq I_{i,j} \leq 1.0$. As an example, the photograph shown in figure 3.1a is imported into DIA. For a better visualization, a full color spectrum is assigned to numbers between 0 and 1 (i.e. after normalization), instead of the grayscale spectrum. The result is given in figure 3.1b.
The walls of the reactor on the picture are automatically detected or manually assigned, and removed from the image, leaving the bed and freeboard for further analysis. The freeboard above the bed is automatically detected by a discrete edge detection algorithm (see figure 3.1c, for further explanation see appendix B). This part of the image will be marked and disregarded in functions calculating the (local) average or normalization.
An intensity gradient can be seen in figure 3.1b, caused by inhomogeneous lighting. This effect is removed by subtracting a (semi)-local average from the image, resulting in figure 3.1d. Pixels within a predefined range r_a are averaged. See the expression below.

$$\mathrm{Avg}_{i,j} = \frac{\sum_{x=i-r_a}^{x=i+r_a} \sum_{y=j-r_a}^{y=j+r_a} I_{x,y}}{r_a^2} \tag{3.1a}$$

in which currently r_a is set to:

$$r_a = 0.25N_x \tag{3.1b}$$

in which i and j are the pixel coordinates and N_x is the image width in pixels. Note that for certain pixels near the edge of the image, it is inevitable that x or y points to a location outside the image borders. Of course, pixels outside the image borders are disregarded. Also, pixels on the freeboard are disregarded in this function.
The final preprocessing step accounts for smoothing the granular phase. The image is blurred using a 5×5 mask. This results in a more uniform phase separation because the edges of particles are filtered out. The histogram of the image is now bimodal due to the preprocessing steps.
Segmentation can take place, using an image dependent threshold $T = 0.9 \times \langle I \rangle$, in which $\langle I \rangle$ is the average image intensity. Pixel intensities below T represent a bubble and are set to 0, other pixels are set to 1. Different threshold values were tested to obtain the best performance in phase segmentation. The result of phase segmentation is shown in figure 3.1e.
The walls of the reactor display a shadow at the walls and bottom, causing these areas to be mistaken as bubbles. A function is implemented to remove these shadows. Now the phase segmentation is completed.

3.2.2 Bubble properties

Obtaining bubble information is performed in a postprocessing step. First, bubbles are numbered by tagging adjacent bubble pixels. By counting the total amount of pixels in a single bubble, the program determines the visible surface area S_b. The equivalent bubble diameter is then determined by (see e.g. Mudde *et al.*[25]):

$$d_b = \sqrt{4S_b/\pi} \tag{3.2}$$

The d_b can be used to draw equivalent circular bubbles (figure 3.1g). The position of a bubble is placed at its center of gravity. Using consecutive images, the velocity of a bubble can be determined if the bubble is also present on a previous image. Two bubbles on subsequent images are linked if the change in position and size of the bubble fulfills the following criteria: the bubble cannot grow or shrink more than 50% of its original size, and the bubble cannot move more than $0.5d_b$. If a bubble breaks up or if bubbles coalesce, the velocity of the new bubbles is set to zero.
The aspect ratio and sphericity of the bubbles are determined as discussed in section 2.3.2. A Sobel edge detection algorithm is used to obtain the bubble edges (figure 3.1f), which are equivalent to the perimeter, needed for the sphericity. It was found that a 5×5 convolution mask performed much better than a smaller mask.
The final step is to write the data to a text file which is used for further analysis.

3.2.3 Validation of DIA

To validate the DIA measurements of bubble size, position, velocity, aspect ratio, perimeter and the bubble tracking system, four image series were created and imported into DIA. DIA should be able to detect numerous shapes. Circles and rectangles were drawn on the images to verify that these shapes were being detected correctly. For these particular shapes it is easy to obtain the surface area and circumference, needed for further validation.
In three series the bubble was not only moving, but was also changing in size. The estimated diameter of the bubble are presented in a parity plot (figure 3.2b). The other parameters discussed in figure 3.2 are validated using the same method. It was found that the size, position and velocity are determined successfully.

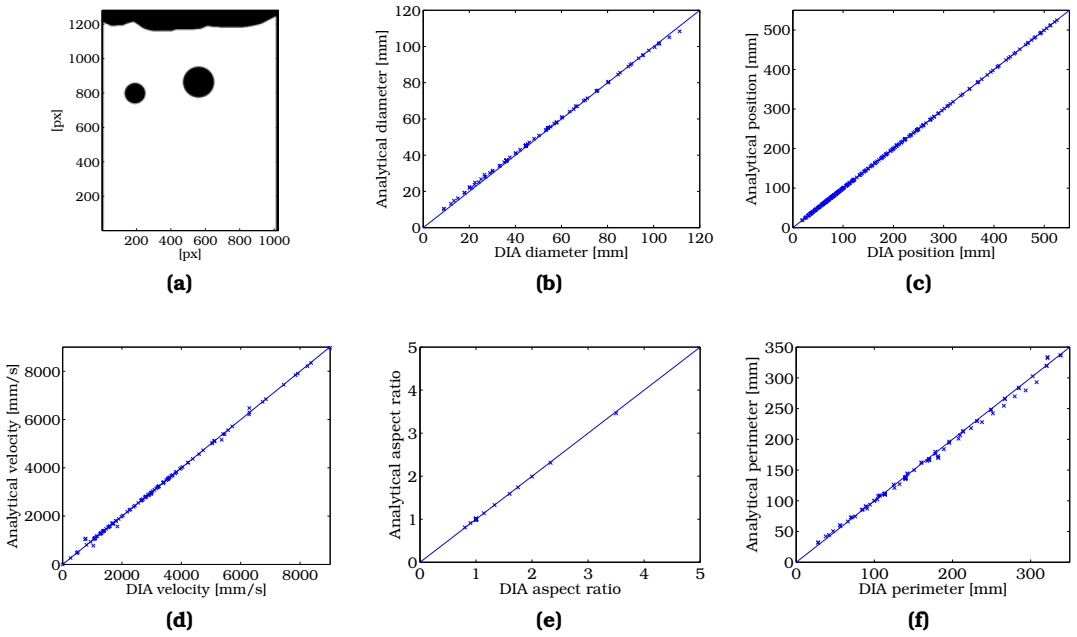

Figure 3.2: **(a)** An example of a synthetic image with known bubble properties to validate DIA. The other images are parity plots: **(b)** diameter; **(c)** Bubble position; **(d)** Bubble velocity; **(e)** Bubble aspect ratio; **(f)** Perimeter (circumference).

3.3 PIV Raining Particles Correction

PIV produces instantaneous vector fields, based on the particle movement inside an interrogation zone. PIV however, does not determine *how many* particles are actually correlated in the interrogation zone, i.e. the amount of particles flowing in that particular interrogation zone. A PIV post processing method is proposed in this section, correcting the original instantaneous PIV flow fields for the amount of particles in this interrogation zone.
For the correction, results of the DIA program (described in section 3.2) are used. The program combining called CRiB, which is an acronym for "Correction for Raining In Bubbles".

3.3.1 Particle raining

For the time-averaged emulsion phase velocity, PIV results for high packed areas of the bed are of more importance for the macroscopic circulation patterns than areas with few particles. The problem becomes apparent when one studies particles falling through the bubbles (raining); relatively to the emulsion phase, few particles fall through a bubble. The particles falling through the bubble have a large downward velocity whereas the high packed emulsion phase moves quite slower. This can be seen in figure 3.3b. These large downward velocities have a vast impact on the time-averaged result. A correction is therefore necessary to eliminate vectors based on relatively few particles, to obtain experimental results with a higher reliability. The PIV software has several functions to filter the data. Vectors which point in a different direction than its neighbors can be changed in order to yield a smooth vector field, e.g. a median filter. Also, it is possible to disregard vectors which deviate substantially from the average. For example, a vector at a location i, j can be ignored in the time-average calculation when its length is outside

the limits of $\text{AVG}_{i,j} \pm 2 \cdot \text{RMS}_{i,j}$. However, it is argued that this type of filtering is uncontrolled, because the filter only depends on the velocity, and not the amount of particles on which the velocity is based. Therefore, valuable data may be disregarded or, perhaps even worse, erroneous vectors are still taken into account for the time-averaged result.

3.3.2 Correction outline

In order to determine whether a vector must be accounted for in the time-average result, the particle density must be determined for every PIV interrogation zone. Link[15] used a particle detection system to obtain the porosity of a spout-fluid bed using coarse particles. A similar approach is used here, however the used particle type is much smaller. Although the particles on PIV images have to be individually distinguishable, the exact number of particles is hard to determine automatically for small particle systems. One may suggest using the average intensity of an interrogation zone as an estimate for the number of particles in that particular zone. However, a linear relation between the intensity and the packing degree cannot be assumed.
On the contrary, the binary frame provided by DIA can be used to classify every pixel in a single phase (figure 3.1e). The frame is denoted as a matrix $\varepsilon^*_{i,j}$, in which 0 represents the bubble phase, and 1 the emulsion phase. (Note that the values of $\varepsilon^*_{i,j}$ are swapped as compared to the conventional porosity $\varepsilon_{i,j}$.) The matrix is used as a reference to determine for every instantaneous vector whether it belongs to the bubble phase, and should thus be disregarded, or to the emulsion phase in which case no correction is needed, or somewhere in between.
This correction algorithm basically assumes that there are no particles present in a bubble. Also, it assumes that the emulsion phase has a constant density.

3.3.3 Correction algorithm

PIV vectors are computed based on an interrogation zone of size $N \times N$ pixels. All the pixels in that zone are averaged to obtain the correction factor $\overline{\varepsilon}^*$ using the DIA information. The correction factor is multiplied with vector $\mathbf{u}$:

$$\mathbf{u}^*_{i,j} = \mathbf{u}_{i,j} \times \overline{\varepsilon}^*_{i,j} \tag{3.3a}$$

in which

$$\overline{\varepsilon}^*_{i,j} = \frac{1}{N^2} \times \sum_{p=i-\frac{N}{2}}^{i+\frac{N}{2}} \sum_{q=j-\frac{N}{2}}^{j+\frac{N}{2}} \varepsilon^*_{p,q} \tag{3.3b}$$

In this equation, $\mathbf{u}^*_{i,j}$ represents the corrected vector, and $\mathbf{u}_{i,j}$ the original vector. By using the average of the entire interrogation zone, vectors based on the bubble-particle interface are still partly considered, whereas the correction factor of an interrogation zone completely within a bubble is set to zero. On the other hand, an interrogation zone consisting of solely emulsion phase pixels leaves the original vector untouched.
Not all vectors on the corrected vector fields should account as a complete vector in the time-averaged result. For instance, imagine a vector based on an interrogation zone with $\varepsilon^*_{i,j} = 0$ (i.e. a bubble). The corrected velocity for the emulsion phase then gives $\mathbf{u}^*_{i,j} = 0$. It is undesired that this velocity is accounted in the time averaged result, because the emulsion phase is not present in the interrogation zone. Therefore, the corrected vectors participate in the time average only for the amount of particle phase pixels they represent. Vectors in bubbles should not be included in the time-averaged result and vectors based on the emulsion phase should be taken into account fully. But, if only a part of the interrogation zone consists of particles, the vector should be

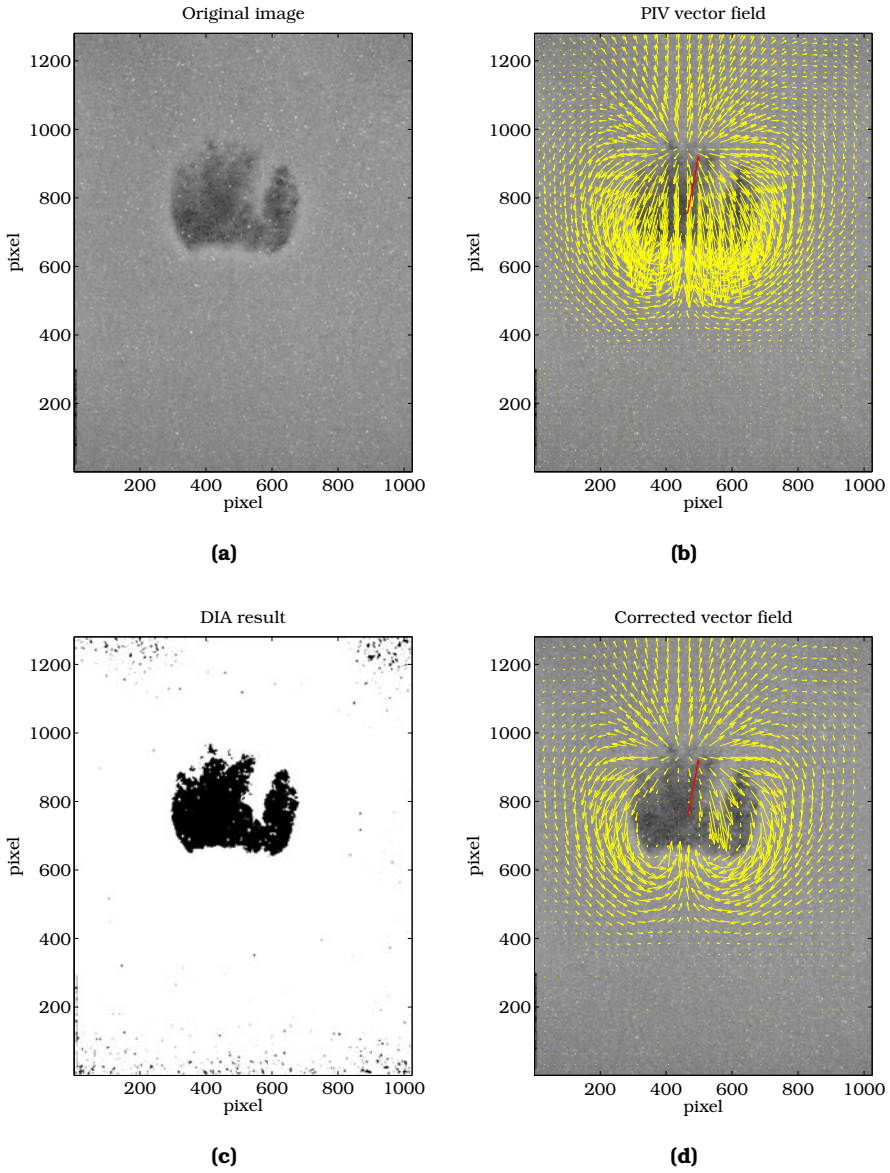

Figure 3.3: The yellow arrows denote particle phase movement. As a reference, the velocity of the bubble (0.34 m/s) is given in red. **(a)** An image pair of a single bubble is used to perform PIV calculations, **(b)** gives the PIV velocity vectors for the image pair, **(c)** shows the result of phase discretization by DIA and **(d)** the instantaneous flow field after correction. PIV was performed using interrogation zones of 64 pixels, with an overlap of 50% and the median filter turned on.

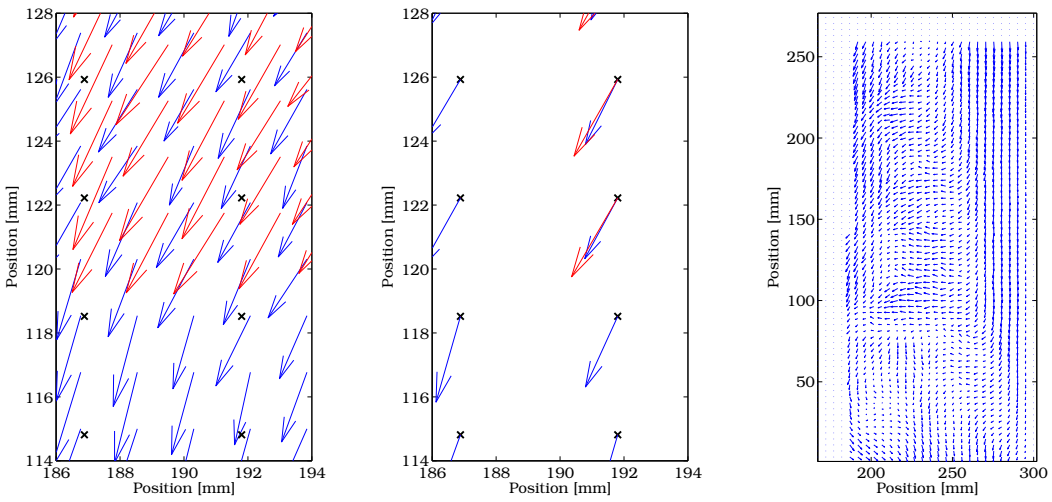

Figure 3.4: **(a)** A part of the overlap area of two time-averaged PIV sessions. The crosses indicate the interpolation grid points. **(b)** Based on four surrounding points of the same time-averaged vector field, vectors are calculated on the interpolation grid. If an interpolated vector can be derived from more than one time-averaged vector field, the resulting vectors are averaged. **(c)** The combination of two interpolated vector fields. The grid points at the left and top side cannot be calculated with these two time-averaged results.

considered partially in the time-averaged result. Therefore, the corrected time-averaged velocity **u** on position i, j over N_f vector fields is calculated by:

$$\overline{\mathbf{u}}^*_{i,j} = \frac{\frac{1}{N_f}\sum_{f=1}^{N_f} \overline{\varepsilon}^*_{f,i,j} \cdot \mathbf{u}_{f,i,j}}{\frac{1}{N_f}\sum_{f=1}^{N_f} \overline{\varepsilon}^*_{f,i,j}} \tag{3.4}$$

3.4 Stitch program

The Stitch program combines multiple PIV time-averaged flow fields. This is necessary in situations in which the bed cannot be photographed as a whole, due to restrictions on the spatial resolution (see Appendix A). In these cases, PIV image series have to be recorded sequentially of different areas of the bed, which in total cover the full bed area.
Seemless stitching can only be performed when the time-averaged vector fields are fully developed. A new vector grid is created by bilinear interpolation of the original results. Multiple vectors on the interpolated grid, due to overlap of the original series, are averaged.

3.4.1 Outline of the Stitch Program

The macroscopic particle circulation pattern of a large bed area is obtained by recording several PIV image series. The camera is moved perpendicular to the bed in order to obtain a full overview. The grid of vectors on two adjoining time-averaged flow patterns, each of a different part of the bed, are not necessarily in line with each other due to

shifting of the camera. Therefore, the stitch program initializes by defining a new grid over the entire bed domain. A part of the overlap area is shown in figure 3.4a, and it can be seen that the two time-averaged results provide their vectors on a different grid. The program uses a bilinear interpolation scheme to derive vectors on the interpolated grid. This is performed for all original time-averaged vector plots independently. Overlapping vectors are now defined at the same location on the interpolated grid. After interpolation, the program determines which interpolation grid vectors are defined more than once (overlap), and averages their velocity components. The new vectors in the overlap area is given in figure 3.4b. Figure 3.4c gives the result of stitching two vector fields.
The result of the Stitch program was validated by synthetic vector plots. Furthermore, it must be mentioned that the bilinear interpolation algorithm used by the stitch program may not be used to obtain a higher resolution than originally obtained by PIV. Throughout this thesis, the number of vectors was significantly reduced.

3.5 Verification of Image Acquisition scheme

In this research, PIV is performed to obtain a time-averaged flow field of the emulsion phase. The time-averaged result can be obtained from multiple instantaneous flow fields. These flow fields emerge from PIV image pairs. The Verification of Image Acquisition scheme-program (VIA) determines whether the number of image pairs, and timer and shutter settings used for PIV experiments are sufficient to produce reproducible time-averaged results. Basically, the program compares the accumulating average vector length of an increasing number of frames, and compares it to an independently determined long-term average. The emerging instantaneous flow patterns all together must yield a constant time-averaged result, and should not be subject to change when taking more instantaneous flow patterns into account.

3.5.1 Algorithm

Instantaneous vector plots (frames) are obtained from the DaVis program after it has performed the PIV calculations. These files are loaded into a matrix with a size of N_i frames times N_j vectors (frames are numbered with i, vectors are numbered with j). The vector length $\ell_{i,j}$ is calculated with vector components in the x-direction (u) and z-direction (v):

$$\ell_{i,j} = \sqrt{u_{i,j}^2 + v_{i,j}^2} \tag{3.5}$$

The accumulating average of the length of vector j is the average of the length at current frame i_c, and all preceding frames $\{i_c - 1, i_c - 2, \ldots, 1\}$.

$$\overline{\ell}_{i_c,j} = \frac{\sum_{i=1}^{i_c} \ell_{i,j}}{i_c} \tag{3.6}$$

The deviation of this average value $\overline{\ell}_{i_c,j}$ from a long term time-average (here denoted by $\overline{\ell}_{\infty,j}$) is used to estimate the reliability of the measurement series. $\overline{\ell}_{\infty,j}$ should be measured *independently* at identical experimental conditions and over a *sufficiently long period*, it accounts for the 'true' average velocity for vectors at position j. The standard deviation of the time average of frames $\{i_c - 1, i_c - 2, \ldots, 1\}$ compared to the long-term average velocity can be defined as:

$$\sigma_{i_c,j} = \sqrt{\frac{1}{i_c} \cdot \sum_{i=1}^{i_c} \left(\overline{\ell}_{i,j} - \overline{\ell}_{\infty,j}\right)^2} \tag{3.7}$$

The program calculates the sum of standard deviations of all vectors in a frame i_c, and divides it by the number of vectors on that frame (N_j), yielding the average standard deviation up to a frame i_c.

$$\overline{\sigma}_{i_c} = \sum_{j=1}^{N_j} \frac{\sigma_{i_c,j}}{N_j} \tag{3.8}$$

The program yields a file containing $\overline{\sigma}_{i_c}$ for all i, which can be plotted as a function of i. Note that this involves the deviation of the vector length, similar to the RMS value, and does not contain information on the direction of the vector.

3.5.2 Example

Two PIV experiments at different conditions were analyzed by the VIA program. In both cases, 4 image series were taken of 700 image pairs each. The superficial gas velocity was set at $1.5u_{mf}$ and $3.5u_{mf}$. Other parameters can be found in table 3.1. From the four imaging series, an average of three times 700 instantaneous vector fields was used to obtain the long term average flow pattern, and one series was used to calculate the accumulating average. Image pairs were taken at 4Hz, resulting in a total measurement time of 3 minutes.
It is shown that 700 instantaneous vector fields are yielding accurate time-averaged results with a low standard deviation from the long-term average at different conditions. The evolution of the standard deviation over an increasing number of instantaneous vector plots, is given in figure 3.5.
Figure 3.5 also gives the deviation from the long-term average of the $3.5u_{mf}$ measurement series corrected for raining particles. It was shown that the deviation decreases. This confirms the expectations because the relatively large velocity vectors of raining particles are filtered out, hence the vectors taken into account are of more uniform length.
It can be expected that for image series from the top of the bed (i.e. with the freeboard in the field of view), the standard deviation will be higher due to more rigorous particle displacement when a bubble erupts at the surface. For the experiments however, we are not interested in the movement of the particles in the freeboard area. Besides, the fact that the standard deviation does not vary much after a certain amount of images is of more importance than the absolute value of the eventual standard deviation, provided that the standard deviation is of course reasonably low (preferably in the magnitude of mm/s).

3.6 Data Flow Diagram

The Data Flow Diagram, given in figure 3.6 shows the exchange of data between the programs. The first entity is the camera (1), which records images using the exposure and time delay settings. The images are saved on a harddisk. The images are generally created for a single purpose: either emulsion phase or bubble information measurements can be performed. Therefore, the data flow can go in two directions from here.
PIV images are imported into the DaVis program (2) which calculates velocity vectors with an image pair. The images are also imported into a stripped version of the DIA program (5), which creates binary frames from the first image of a PIV image pair. The instantaneous velocity vector field and the binary frame are imported into the CRiB program (6), which requires both data series to correct for raining particles. After the correction, the time-averaged result is exported from the CRiB program. These frames can be stitched (4), if necessary, to obtain the time-averaged flow field of the entire bed. Note that the Stitch program can also handle time-averaged results directly exported

Property	Series #1	Series #2
Superficial gas velocity	$1.5u_{mf}$	$3.5u_{mf}$
Bed width	0.15 m	0.30 m
Aspect ratio	3.0	1.0
Time delay within image pair	5.0 ms	3.0 ms
Exposure time	1 ms	0.8 ms
Area of reactor photographed	Bottom	Left bottom
Particles	400-600μm glass beads	400-600μm glass beads
Number of vectors / frame	1280	5120
Average absolute velocity on long term average plot	0.104 m/s	0.261 m/s
Average standard deviation of frames #1 – #700 ($\overline{\sigma}_{700}$)	$0.43{\cdot}10^{-3}$ m/s	$0.29{\cdot}10^{-3}$ m/s
Relative standard deviation	0.41%	0.113 %

Table 3.1: Minimum PIV time test parameters

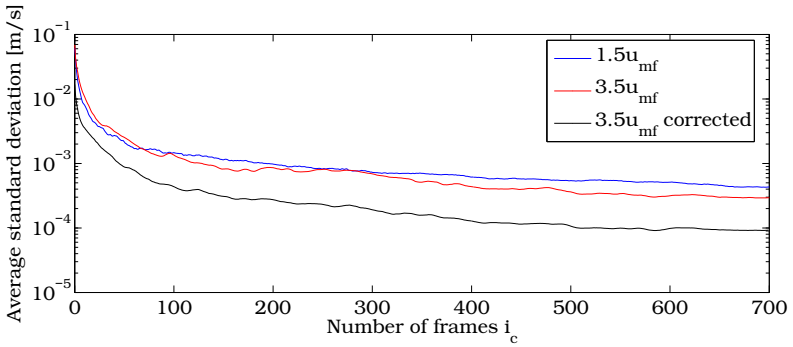

Figure 3.5: Evolution of the average standard deviation over an increasing number of instantaneous vector plots taken into account to derive the time-averaged result. The measurements were performed at $u_0 = 1.5u_{mf}$ and an aspect ratio of 3 in the 15 cm wide bed, and $3.5u_{mf}$ with an aspect ratio of 0.5 in the 30 cm wide bed, both with glass beads of size $d_p = 400 - 600\mu$m. Also, the effect of correcting for raining particles is shown for the $3.5u_{mf}$ case.

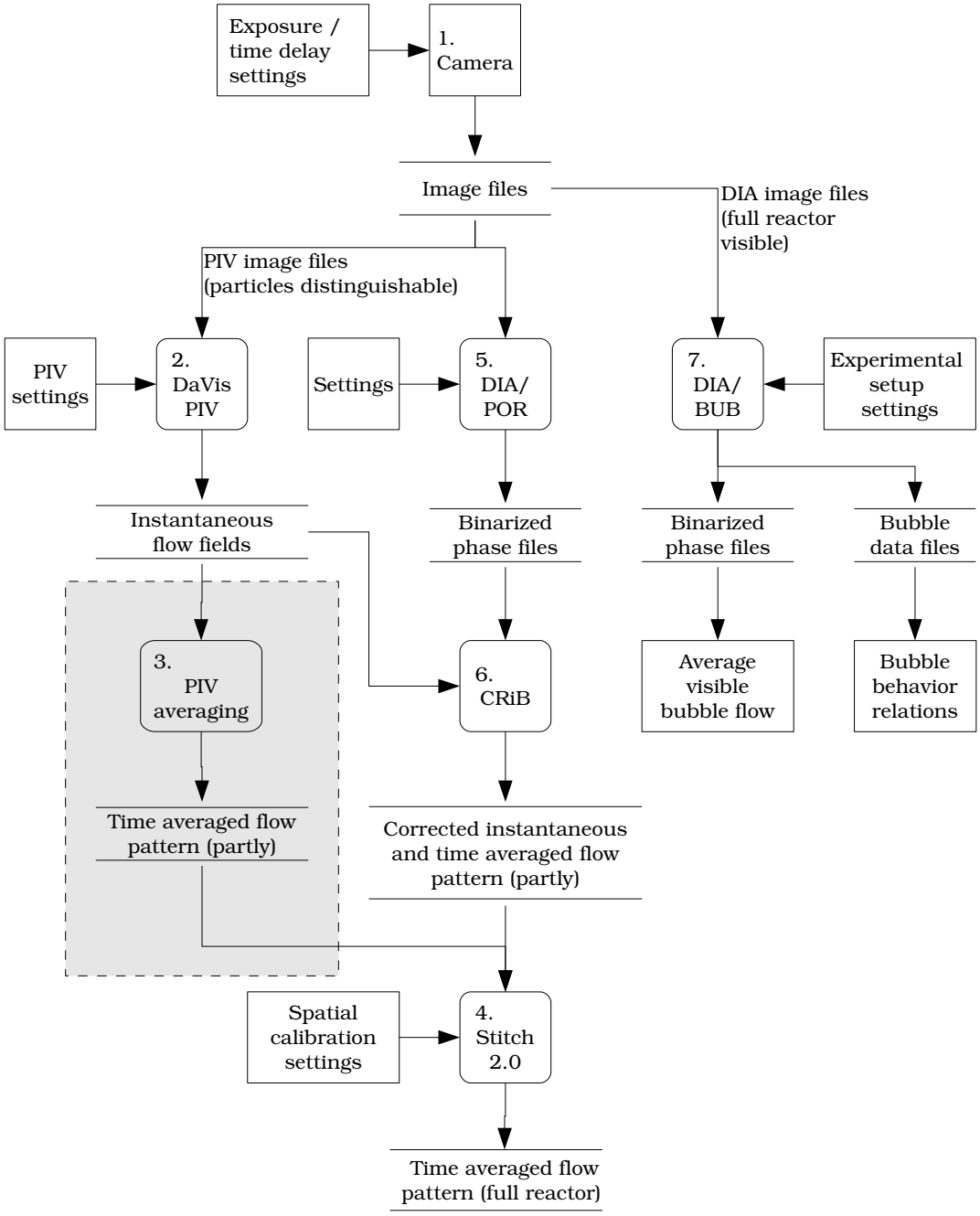

Figure 3.6: The Data Flow Diagram between the different programs

from DaVis program (3), i.e. without correcting for raining particles (gray area). However, this route is not used, as correction *has* to take place on current results.
The second path is used for images taken to investigate bubble phase behavior. The images are imported into the full version of the DIA program (7). The program is started after some experimental setup settings are assigned, e.g. the time delay between images and the reactor width. The exported data is used to obtain correlations of bubble phase behavior.

Chapter 4

Experiments

4.1 Introduction

Experimental data are acquired by photographing a pseudo-2D fluidized bed. The experimental setup will be discussed first in section 4.2.1. Obviously, the camera is an important part of the setup. The settings used for the camera are discussed in section 4.2.2. The images are imported into the appropriate program which performs the calculations. PIV calculations are performed using commercial software. The settings of the PIV software are discussed in section 4.2.3. The glass beads used in the experiments were analyzed. The result is given in section 4.2.4. Finally, an overview of the different investigated parameters is given in section 4.3.

4.2 Experimental setup

4.2.1 Pseudo-2D fluidized bed

The setup contains two pseudo-2D beds with different bed widths which are operated separately. The wide bed has a width of $d_{bed} = 0.30$ m, the small bed is 0.15 m wide. In both cases, the depth of the pseudo-2D bed is 0.015 m. The behavior of both phases is observed through the glass front plate.
The fluidizing gas is compressed air from the local air network. A buffer vessel is used to maintain a constant pressure. The gas inflow is supplied to the distributor by two inlets. Both inlet streams are controlled using two parallel mass flow controllers (MFC); for low gas flow rates, the 20 l/min MFCs are used. At higher superficial gas velocities, the 100 l/min MFCs are used. The MFC calibration was verified several times as experiments with the setup were spread over time and it was found that the calibration maintained to be valid during the experiments. In all cases, the left and right gas inlet were set at equal gas flow rates. The gas from both inlets is combined in a chamber below the fluidized bed, in which air is pre-distributed over the column width. At the top of this chamber, the distribution plate performs the actual gas distribution over the bed.
Steam is added to the gas stream before it reaches the inlet chamber. A relative humidity of $\sim$ 60% is necessary to prevent the formation of static electricity. Due to static electricity, particles start to clog, which influences the macroscopic behavior severely. The humidity of the gas at the top of the fluidized bed is measured after a few minutes of stabilization time. If the desired humidity is reached, measurements can be performed.

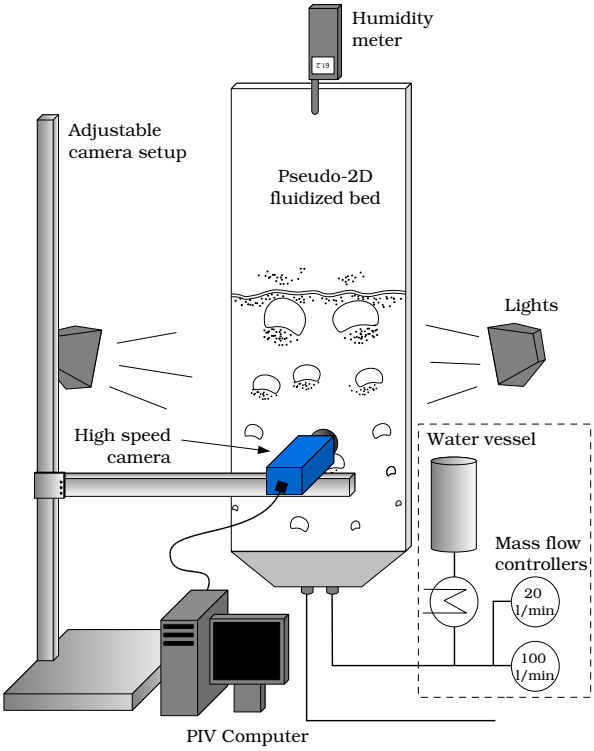

Figure 4.1: A schematic representation of the experimental setup. The gas feed is set by mass flow controllers. The camera is placed in front of the bed and can move parallel to the bed both horizontally and vertically. Direct lighting is required for high quality images.

Accuracy of the gas flow

An error is made in the superficial gas flow due to changes in the environment. A deviation of the air temperature of 2°C is found to cause an error in the gas flow of about 0.2%. Moreover, the MFCs can vary unknowingly by 0.1. This causes an error of about 0.3%. In total, the gas flow could therefore deviate by 0.5%.

4.2.2 Camera settings

A LaVision ImagerPro high-speed CCD (charge-coupled device) camera is used to record images from the bed. The camera has a maximum resolution of 1024×1280 pixels and contains 2GB of internal memory. An IEEE 1394 FireWire connection is used for data transfer. The camera shutter is controlled by an oscillator connected to the computer. Motion blurring can be prevented by setting a short exposure time. Consequently, the amount of light that reaches the sensor is reduces. Therefore, two 500 W Halogen lights on each side of the setup are used to illuminate the bed. Also, the aperture of the camera can be used to achieve a high contrast on the images, at the cost of a loss of depth of field.

PIV images

PIV image pairs are taken at 4 Hz, i.e. every second 4 image pairs are recorded. The exposure time is set to 0.8 ms, with an effective time delay of 3 ms between the images

of a pair. Using this scheme, the camera is able to record for 3 minutes. Whether the scheme yields a truthful time-average flow field was investigated in section (3.5).

DIA images

Bubble behavior experiments are recorded from a larger distance, to obtain a full view of the entire bed. Therefore, the CCD sensor size is adjusted to contain solely the bed. By declining the resolution of the sensor, images require less memory and therefore, more images can be recorded. The number of images recorded varies between 1424 images (full sensor utilized) up to over 10000 images. Most series are recorded twice under similar conditions. This data will be used to verify the reproducibility of the results.
In order to track bubbles, images are recorded with a uniform time delay rather than in pairs. The time delay was set to 10 ms. A delay of 50 ms causes bubbles to move too far between the images, which caused trouble with the tracking system in the DIA program. Using a delay of 2 ms on the other hand, results in a short total measurement time, which is not desired.

4.2.3 PIV Settings

PIV was performed using the DaVis software from LaVision. Correlation of interrogation windows was performed in multi-pass mode; first, a ballpark estimate is made by an interrogation window of 128×128 pixels. Consequently the window size was decreased to 32×32 pixels with 50% window overlap to obtain the eventual resolution. Spatial cross-correlation patterns (e.g. figure 2.3b) were checked visually in a random way to verify whether the correlation peak R_D exceeded the random correlation significantly, i.e. whether the dislocation could be determined with high precision.
For PIV measurements, the maximum resolution of the camera is used, to cover an area as large as possible whilst keeping particles distinguishable. As stated in the PIV design rules (Appendix A), a single particle has to be represented in diameter by at least 3-4 pixels. Although the photographed area may vary slightly due to repositioning the camera, the recordings generally cover 0.12 × 0.15 m. The number of image series for a single measurement varies between 1 and 15, depending on the size of the bed. For the wide bed, three image series were recorded in lateral direction and in axial direction, up to five series were required. The small bed could be recorded from wall to wall, but depending on the aspect ratio and superficial gas velocity, several image series above each other were required. The image series were recorded with an overlap area of at least 0.02 m. After correction for the overlap of image series, a single vector field attributes approximately 58×74 vectors to the whole flow field.

4.2.4 Particles

The particles used in the experiments are glass beads, considered as model-particles. The density of the particles is $\rho_{glass} = 2500$ kg m^{-3}, which indicates that a particle size as low as $\sim 100\mu$m could be chosen to remain in the Geldart B range (figure 2.2.1). Due to the fact that PIV images should encapsulate a single particle in at least 3–4 pixels (see appendix A), a diameter range of $400 \leq d_p \leq 600$ μ m is chosen. Particles in olefin polymerization reactors range from 0.25-1mm[1], and therefore these particles are within the range of the project scope.
The glass beads are produced by SiLibeads, with an indicated particle diameter range from 0.4 to 0.6 mm. This was verified by laser diffraction, using a Sympatec HELOS system. A cumulative distribution function shows the diameter of two samples in figure 4.2a. It is found that the average diameter is about 485 μm.
Equations 2.1 and 2.2 are used to obtain the theoretical minimum fluidization superficial gas velocity. For these glass beads fluidized with air, the Archimedes number is

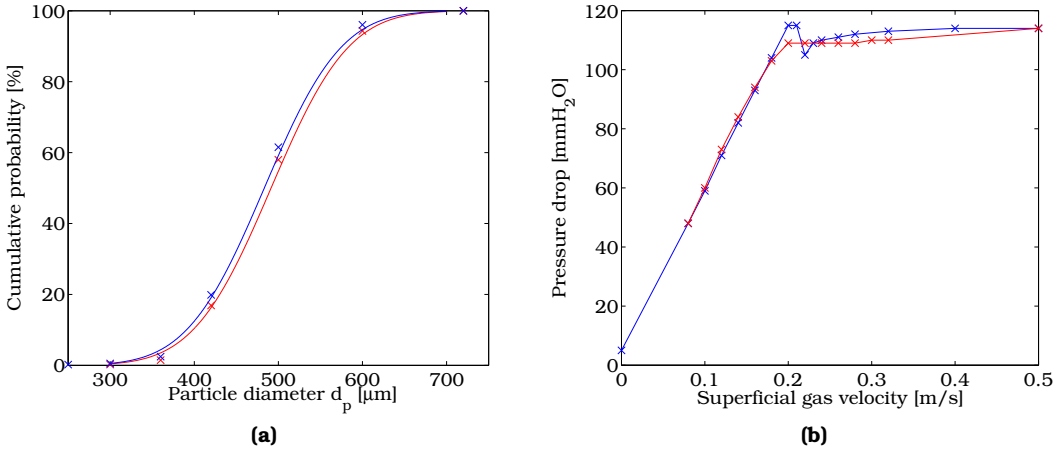

Figure 4.2: **(a)** Cumulative distribution function of the particle diameter of two samples analyzed by laser diffraction. The markers denote the actual measurements. It can be found that the average diameter is about 480 - 490 μm. **(b)** Experimental determination of u_{mf} by pressure drop experiment. The blue line was obtained at increasing u_0, the red line denotes the pressure drop for decreasing superficial gas velocity. The diagonal and horizontal lines cross at 0.18 m/s.

$Ar \approx 9805$, and the minimum fluidization velocity was found to be:

$$u_{mf} = \left(\frac{1.85 \cdot 10^{-5}}{1.2 \cdot (485 \cdot 10^{-6})}\right)\left(\sqrt{(27.2)^2 + 0.0408 \cdot 9805} - 27.2\right) = 0.20 \text{ m/s}$$

For pseudo-2D systems, the minimum fluidization velocity is normally found to be higher than in 3D systems at similar conditions[19]. Therefore, u_{mf} is determined experimentally by a pressure drop experiment. The results are given in figure 4.2b. The diagonal and horizontal data was used to obtain two linear relations, which cross at $u_{mf} = 0.18$ m/s. This is slightly lower than predicted by theory. The constants used in this calculation are based on experimental data of various particle systems, so the difference can be explained by the equation being very general. The experimental value of 0.18 m/s will be used as u_{mf} from now on. The terminal velocity of a single particle in air was calculated for the average particle diameter and was found to be 1.36 m/s, which is about 7.5 times higher than u_{mf}, a value also found in literature[34].

4.3 Summary of operating conditions

For both PIV and DIA experiments, the relative superficial gas velocity, u_0/u_{mf} is one of the key parameters. This ratio will be varied between $1.5 \leq u_0/u_{mf} \leq 3.5$. Two pseudo-2D fluidized beds with a diameter of $d_{bed} = 0.15$ m and $d_{bed} = 0.30$ m are operated. These beds are used to determine the influence of the bed width and the aspect ratio. The bed height will be varied between 0.075m and 0.45m. An overview of these parameters is given in table 4.3.

Parameter	Settings
Superficial gas velocity u_0	1.5u_{mf} 2.0u_{mf} 2.5u_{mf} 3.5u_{mf} (not at d_{bed} = 0.3 m and h/d_{bed} =1.5)
Bed diameter d_{bed}	0.15 m 0.30 m
Unfluidized bed height in the wide bed, $d_{bed} = 0.30$ m	0.010 m (h/d_{bed} =0.3) 0.150 m (h/d_{bed} =0.5) 0.300 m (h/d_{bed} =1.0) 0.450 m (h/d_{bed} =1.5)
Unfluidized bed height in the small bed, $d_{bed} = 0.15$ m	0.075 m (h/d_{bed} =0.5) (PIV only) 0.150 m (h/d_{bed} =1.0) 0.300 m (h/d_{bed} =2.0) 0.450 m (h/d_{bed} =3.0) (DIA only)

Table 4.1: Experimental Parameters

Chapter 5

Results and Discussion

This chapter presents the outcome of this investigation. The emulsion phase hydrodynamics are the topic in section 5.1, which includes an investigation of the proposed correction algorithm. Bubble phase data resulting from the DIA program is discussed in section 5.2, where the reproducibility of the results is explored, followed by an analysis of several correlations describing bubble properties. Section 5.3 discusses a proposal to describe the interaction between the two phases.

5.1 Hydrodynamics

A quantitative study of time-averaged particle phase flow patterns has been performed. The investigation comprises of 28 cases, varying bed diameter d_{bed}, unfluidized bed height h and superficial gas velocity u_0. The time-averaged PIV results are corrected for raining particles. First, this effect is investigated, presenting a single case. Then, the results of the other cases are presented and discussed.

5.1.1 Correction for Raining Particles

The instantaneous vector fields obtained from PIV are corrected for raining particles in the bubbles. The downward vectors resulting from falling particles are considered as not relevant in this approach. The time-averaged results are calculated with the new instantaneous vector plots.
Figure 5.1 shows a comparison between the original time-averaged result and the result after correction for raining particles. The figure displays the flow field in the wide bed (d_{bed} = 0.30 m) for a superficial gas flow of $2.5u_{mf}$. In order to obtain the flow pattern of the entire bed, 12 image series were measured and stitched.
On the left hand side of the figure, the time-averaged flow pattern of the entire reactor is given. Especially at the center of the top of the bed, the correction algorithm yields a more distinguished upward velocity. Also, an upward flow from the lower right is more pronounced after correction than it is in the original case.
On the right hand side, the vertical time-averaged emulsion phase velocity u_z is given as a function of lateral position (lateral velocity profile), for four different bed heights. The dashed lines mark the $u_z = 0$ line. In these figures, the difference is even more abundant; the original case barely shows an upflow of particles, whereas the corrected case does show an upward flow at all shown axial positions. Note that the downflow of particles at the wall region is barely influenced by the correction algorithm, which was expected as bubbles are mostly present in the center of the bed.
Although no aspirations can be made that this method determines the particle mass

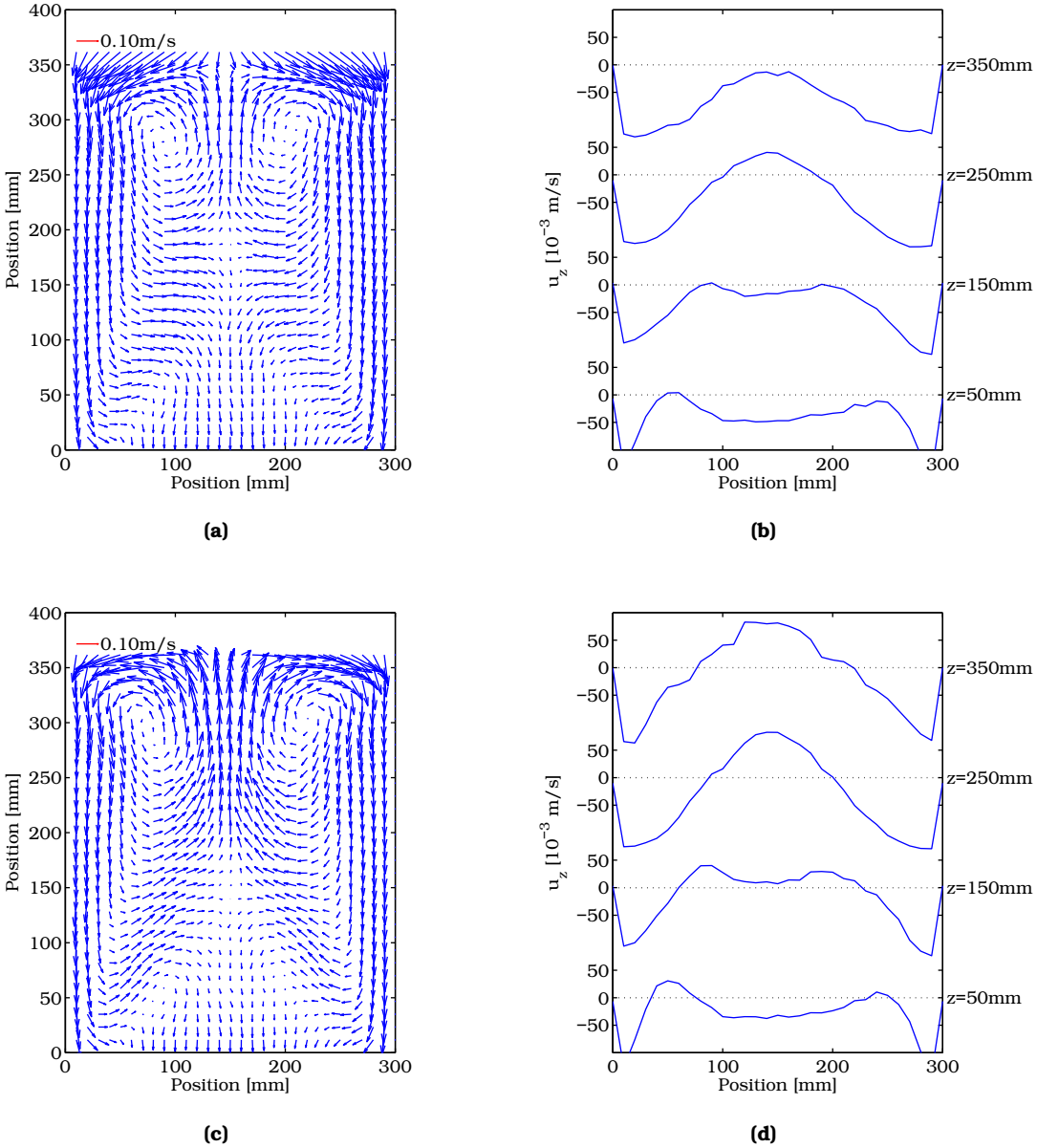

Figure 5.1: The effect of the correction for raining particles. The flow pattern of the entire bed is shown, accompanied by the vertical velocity component at 4 different heights in the bed. Parameters: d_{bed} = 0.30 m; u_0 = 2.5u_{mf}; h = 0.30 m; **(a)+(b)** The raw data from DaVis, no filters used **(c)+(d)** The result after correction for raining particles.

flux, the downflow of the particles in the corrected flow fields is in a much better equilibrium with the upward flow than the uncorrected result. Still, in the downward flow regions a higher velocity is observed than in the upflow regions. Also, downflow regions are encountered over approximately 2/3 of the bed area. To conserve continuity, the amount of particles flowing down should equal the amount of particles flowing up. The discrepancy here is probably caused by the current implementation of the correction algorithm. Velocity vectors based on interrogation zones consisting of both bubble phase and emulsion phase pixels are considered only partly. Vectors based on the wake of a bubble are pointed up. However, when a part of the bubble is also visible in the interrogation zone, the velocity of the upflowing particles in the wake is decreased. This can be prevented by using smaller interrogation zones for PIV analysis, or by adapting the correction algorithm. Test cases will have to be performed to investigate an adapted correction algorithm, to make sure that only the desired vectors are disregarded.
The most desirable way is to mark the bubbles on the images before PIV is performed. If the bubbles do not take part in the correlation, only the high packed emulsion phase is considered by PIV, and filtering will not be required anymore.
Other cases were also checked for the correction effect. Similar results were found, with an increased axial velocity of the particle phase from the lower wall region to the center-top region of the bed. The correction algorithm has yielded the expected results, and therefore it is concluded here that the proposed correction algorithm provides the high-packed emulsion phase velocity in a more truthful way.
Disregarding raining particles is only allowed when the particle density in high packed areas of the bed is significantly higher than the amount of particles falling through the bubbles. Based on visual inspection and the DIA program, this can be assumed for current experiments. However, for other particle types this might not be true. If many particles fall through the bubbles, the intensity differences between the two phases will disappear, and the correction algorithm will cease to work. If one then still feels the need to correct for falling particles, he has to resort to disregarding large vectors based on velocity rather than on the intensity. In addition, it has to be mentioned that vectors based on very small bubbles are not filtered out. The bubbles go unnoticed through the reactor until they have grown large enough to span from the front to the back plate. It was observed that bubbles reach the minimum diameter, in order to be visible, reasonably low in the bed.

5.1.2 Particle phase flow

The macroscopic particle circulation patterns are studied at different superficial gas velocities and bed aspect ratios. Three cases are presented in figure 5.2. On the left hand side of the figure, the time averaged emulsion phase flow patterns are given. For clarity, the number of vectors in the image has been reduced significantly. On the right hand side, the emulsion phase axial velocity as a function of the lateral position is given at different heights in the bed. The cases presented here are measured in the wide bed (d_{bed} = 0.30 m), with an unfluidized bed height of 0.45 m. The superficial gas velocity ranges from $1.5u_{mf}$ up to $2.5u_{mf}$. The other cases are given in appendix C, page 58.

Up- and downflow

Figures 5.2(b,d,e) give insight in the development of the lateral velocity profile as a function of height in the reactor. The trend of the lateral velocity profile does not change significantly at higher gas flows. As expected, most systems show a double peak near the distributor plate. This is the result of the bubbles mainly emerging from the lower wall region. At increasing height, the bubbles shift towards the center of the bed. It appears that variation of the unfluidized bed height and the superficial gas flow does not change the path of the bubbles. At low aspect ratios, the upflow through the center

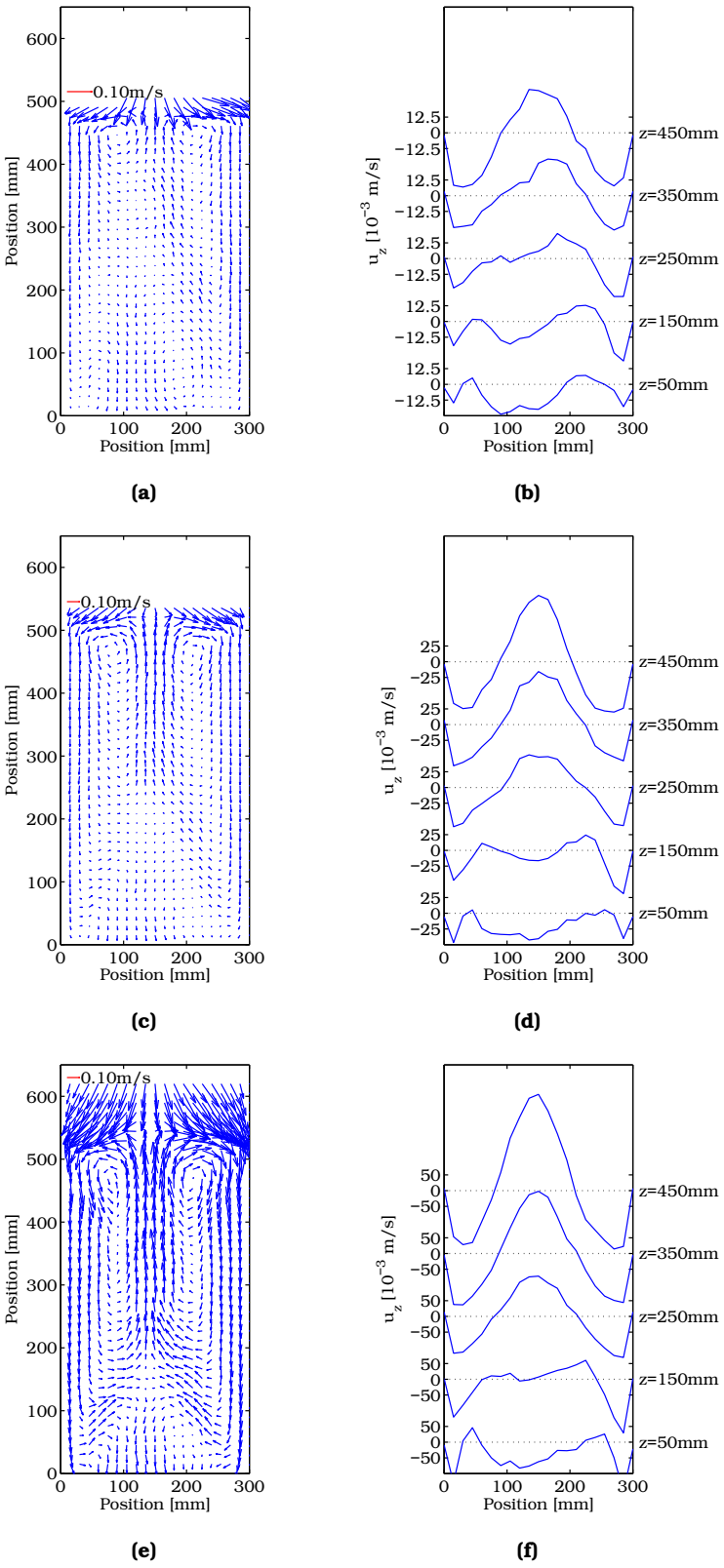

Figure 5.2: Parameters: d_{bed} = 0.30 m; h = 0.45 m; **(a)+(b)** $u_0 = 1.5u_{mf}$; **(c)+(d)** $u_0 = 2.0u_{mf}$; **(e)+(f)** $u_0 = 2.5u_{mf}$;

will not be encountered, as bubbles erupted at the surface before arriving in the center of the bed. This can be found in e.g. figures C.1 and C.2.
In the three cases presented in figure 5.2, the upflow of particles is encountered at lateral position $0.1 \leq x \leq 0.2$ m, i.e. between one third and two thirds of the bed width, for heights above $z \geq 0.25$ m. In this respect, it is remarkable that in the small bed (see figures C.6, C.7), the upflowing center of the bed seems relatively broader than in the wide bed. This range also approaches approximately 0.1 m. This is due to the relatively larger bubbles compared to the bed diameter. It will be shown later in this chapter that bubbles reach their maximum size (imposed by the bed width) in the small bed, whereas this is not the case in the wide bed.

Velocity

In figure 5.2, it is shown that the axial particle velocity increases significantly at increasing gas velocities. This effect is clearly seen in the higher regions in the bed. Not only the upward flow of particles through the center of the bed experiences a higher velocity, but also the downward velocity at the walls. The increased upward flow can be explained by the increasing number and size of bubbles, and the speed with which they travel through the bed. The downward flow at the walls also increases at higher superficial gas velocities.
Downflow of particles is also present at the lower center of the bed. One reason is that the main bubble path leads over the center, as found in literature (figure 2.1). But also, bubbles smaller than the bed thickness form here. The particles stream down along the frontal glass plate, unnoticed by the correction algorithm.
A slight asymmetric profile is observed at low superficial gas velocities. This effect is seen in both the small and the wide column. It is concluded that for low gas flows, the porous distributor plate displays a non-homogeneous gas flow distribution.
Besides, unexpected results are obtained using the small bed and an unfluidized bed height of 0.30 m (figures C.8 and C.9). The circulation profile is very asymmetric, and positive axial particle velocities (i.e. rising particles) are barely encountered at low u_0. During the experiments, bubbles high in the bed seemed to disappear due to excessive particle raining, a phenomenon which was not encountered previously at different operating conditions. An example is given in figure 5.3, together with bubbles that are usually encountered. In the cases at relatively high superficial gas velocities, the regime could be said to approach the slugging regime. However, a similar effect is observed at $1.5u_{mf}$. As of yet, the reason for sudden excessive raining at the top of the bed remains undetermined.

PIV measurements have the advantage that the entire flow field can be measured non invasively. It can be performed in-house, and is therefore easy to perform. Besides, the time of measurement is relatively short, which decreases the chance of fluctuations in operating conditions. However, at this point it cannot be determined whether the emerging particle phase velocity is also valid in a 3D bed. As mentioned in the theoretical section, hydrodynamics were found to be qualitatively comparable between 2D and 3D environments. Using PIV and the correction algorithm, the first step is made in a quantitative comparison between 2D and 3D beds. To obtain 3D data, PEPT or CARPT experiments have to be performed at identical conditions. The experimentally determined flow pattern in 3D can be used to quantify the differences between the geometries. Once insight is gained in the quantitative differences, experiments for bubble-particle interaction studies can be performed in a pseudo-2D bed using PIV and DIA.

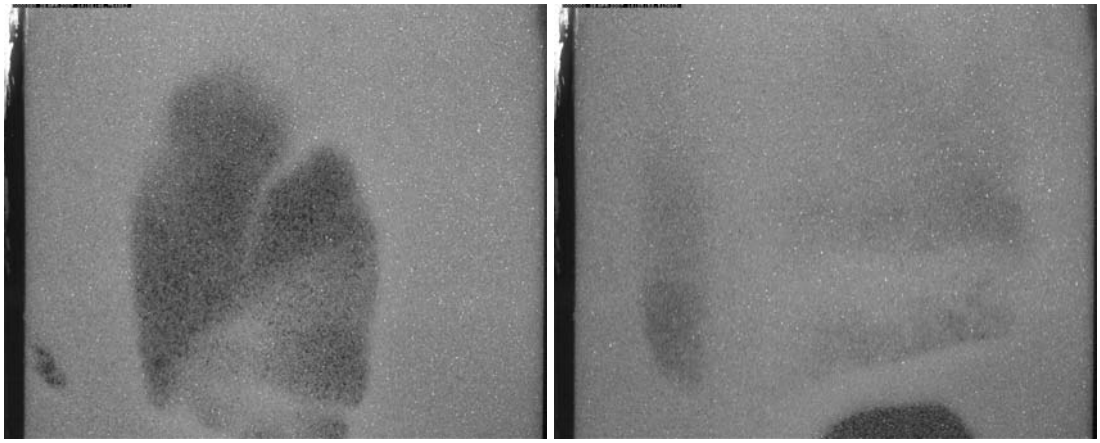

(a) (b)

Figure 5.3: Excessive raining through bubbles was observed in the small bed, at heights above 0.2 m. Images are taken of the small bed, visualizing the entire width of the column. The height ranges from 0.2 m to 0.32 m. **(a)** Normal raining through a bubble; **(b)** Excessive particle raining.

5.2 Bubble properties measurements

In this section, the data processing of DIA output files is outlined. Then, the reproducibility of the DIA experiments will be investigated. The section concludes with results concerning bubble properties, and the verification of theoretical correlations.
Experiments to obtain bubble properties are performed as discussed in the experimental chapter (4). The images were analyzed by DIA. For every image imported in the DIA program, an output file was generated, containing the parameters for every bubble on the image. All files were imported into MATLAB, which was used for further analysis. A script has been written, to analyze the dependence of two given parameters. It will be explained by using an example case, relating the bubble diameter d_b to the axial position z. For the independent parameter (in this case z), the minimum and maximum are determined. Then, this range is divided into equal sized classes $n(z)$, e.g. the horizontal rows in figure 5.4 (disregarding the division of the horizontal axis for now). Consequently, all bubbles are arranged into one of these rows according to the axial position of the bubbles (center of gravity). The average of the dependent variable d_b is obtained per row, yielding an *average* value for each class ($\overline{d}_b(n)$) and the *amount* of bubbles found in this class. The latter is needed to investigate the distribution of bubbles over the independent parameter.
The division of the independent parameter into classes can be done with any number of classes. However, when the size of a class decreases the amount of data in that class also decreases. Care must be taken that the amount of bubbles in any class is still above about approximately 200 in order to yield statistically reliable results.

5.2.1 Reproducibility

The reproducibility of the results is investigated by analyzing two independent measurement series obtained at identical fluidization conditions. Measurements of the 0.30 m wide bed are used for the analysis. The unfluidized bed height h in this case is 45 cm, and the superficial gas velocity u_0 was varied between 1.5, 2.0 and 2.5u_{mf}. A single measurement series consisted of 2110 images. The results are discussed below.

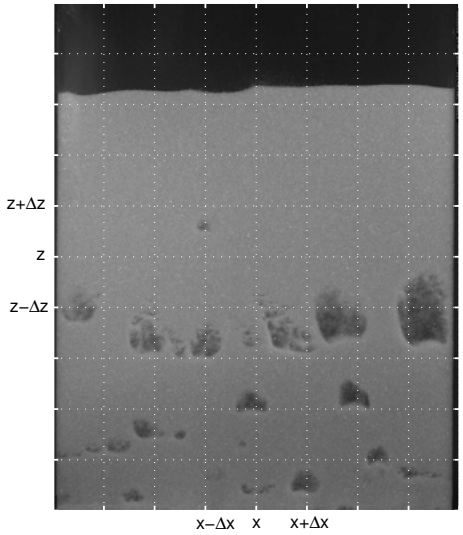

Figure 5.4: The independent parameter is divided into a number of classes. In this figure, the (lateral or axial) position of a bubble to is classified. Every detected bubble is placed in a single class.

Bubble size

Figure 5.5a shows the average bubble diameter $\overline{d}_b$ as a function of the height in the bed. For all u_0, the two measurement series do not show great variation up to 0.3 m high and show a steadily rising trend. Thereafter, $\overline{d}_b$ still follows an upward trend up to 0.5 m, but large peaks and gaps become visible at higher superficial gas velocities. This is caused by a low number of bubbles measured in the upper bed region, as can be seen in figure 5.5b. Barely 2% of the recorded bubbles is found at heights above 0.3 m.
The reproducibility of bubble diameter measurements has been confirmed, as long as enough data is provided. This has to be checked using the bubble distribution.

Bubble rise velocity

Figures 5.5c and 5.5d show the bubble rise velocity as a function of the diameter. Large fluctuations can be found for bubbles with an equivalent diameter larger than 80 mm. Once more, the answer to this phenomenon is found in the distribution diagram; the number of bubbles with an equivalent bubble diameter above 80 mm approaches zero. However, when comparing the duplicate cases, it is found that up to $d_b = 80$ mm, the data does show identical results.

From the results above, it can be concluded that from 2110 images, DIA yields reproducible data as long as a single class is provided with enough data. The remaining duplicate measurements were also verified in this manner. Good reproducibility was achieved. Henceforth, duplicate data series are not shown in the given graphs for the sake of visibility.

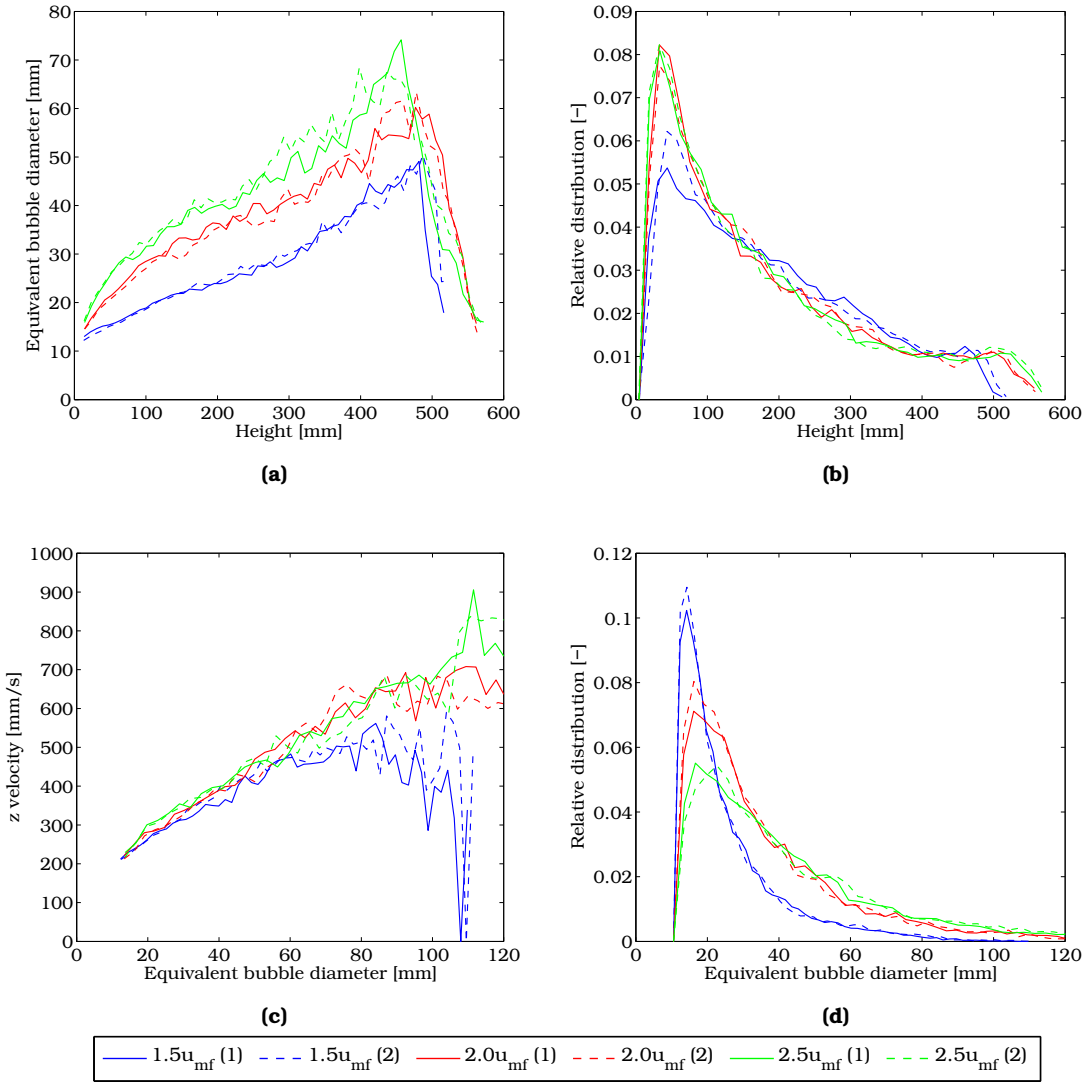

Figure 5.5: Reproducibility experiments show that DIA produces similar output for identical conditions. Similar colors represent similar velocities, dashed and solid lines represent the first and second measurement series. Parameters: d_{bed} = 0.30 m; u_0 = 1.5,2.0,2.5u_{mf}; h = 0.45 m; n = 60 classes. **(a)** Bubble diameter d_b as a function of the height h in the bed **(b)** Relative distribution of bubbles over the height of the reactor **(c)** Vertical bubble velocity u_z as a function of its diameter d_b **(d)** Relative distribution of bubbles of a certain diameter.

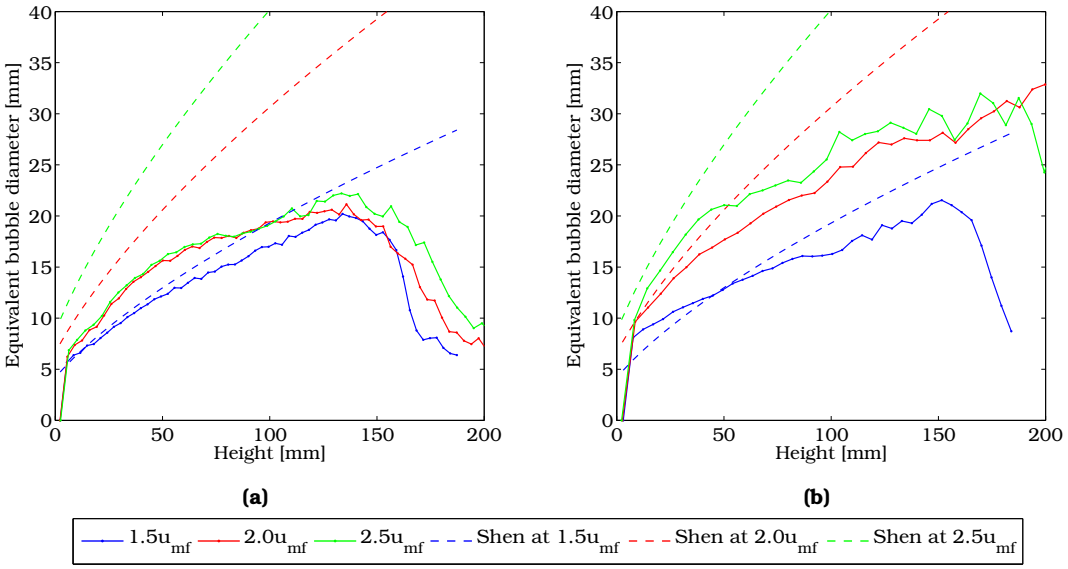

Figure 5.6: The relation of Shen *et al.* is plotted with experimental data. Parameters: u_0 = 1.5,2.0,2.5u_{mf}; h = 0.15 m; n = 40 class. **(a)** Small pseudo-2D bed (0.15 m) **(b)** Wide pseudo-2D bed (0.30 m).

5.2.2 Bubble size

From figure 5.5b, it can also be seen that the total number of bubbles observed in the lower region of the bed is smaller for u_0 = 1.5u_{mf}. This can be explained by the fact that a relative large part ($\geq 75\%$) of the gas moves through the interstitial volume of the particle phase. The bubble size distribution broadens at higher superficial gas velocities, caused by coalesce and faster growth at higher superficial gas flows.
The sudden decrease of the bubble diameter above 0.5 m is caused by leakage of the bubbles to the freeboard. A similar phenomenon was also observed by Shen *et al.*[23] as shown in figure 2.4a (page 11). Also, small satellite bubbles are visible when bubbles erupt at the surface, which have a significant influence on the bubble diameter.
The Shen-correlation (eq. 2.10) was checked for agreement with the current results. Figure 5.7 shows that some agreement can be found in case the wide bed was used, but only at low superficial gas velocities. At these conditions, the bubbles experience little wall effects compared to other experiments in the small bed, or at higher superficial gas velocities. The disagreement between the correlation and the experimental data is therefore attributed to the bed width and depth differences between the current experiments, and those of Shen *et al.*. The correlation is based on data obtained in a bed with aperture 0.68×0.07 m, in which wall effects play a smaller role than in the current setup. Bubbles in a wide bed grow larger at higher superficial gas velocities, whereas they are being constrained in a smaller bed, explaining the main part of the differences. The restriction by the walls is best shown at high superficial gas velocities. Figure D.1 on page 68 shows the distribution of bubble diameter d_b at different heights in both beds. Increasing the bed height causes bubbles to grow larger, because their path through the bed is longer. In the small bed (d_{bed} = 0.15 m), the limitation of bubble growth appears as an identical bubble size distribution for bed heights of 0.30 m and 0.45 m. In the wide bed of d_{bed} = 0.30 m, bubbles *do* grow larger when the bed is raised to 0.45 m. Also, the distribution is much broader than in the d_{bed} = 0.15 m case at similar bed heights. It is therefore noted that the walls do not only induce a maximum

	Bed width (d_{bed})	A	C
Shen	0.68 m	0.89	0.67
Wide	0.30 m	0.45	0.54
Small	0.15 m	0.30	0.50

Table 5.1: Values for coefficient A and power C in different bed sizes.

bubble size, but also affect the bubble size distribution in the lower diameter range. Appendix D also gives the comparison with the relation of Shen *et al.* for the other cases. Here, it can also be concluded that the bed in the current setup is too narrow to validate the correlation of Shen *et al.* Therefore, the correlation of Shen is adjusted to fit the current experimental data.

Bubble diameter correlations

A more generic description of bubble growth seems necessary. By adjusting the Shen-correlation, a attempt has been made to find a new expression which fits current experimental data and still complies with the original Shen-correlation. The generic expression is:

$$d_{b,2D} = A\left(u_0 - u_{mf}\right)\left(z + 3\frac{A_0}{t}\right)^C g^{-1/3} \tag{5.1}$$

in which parameters A and C are the parameters under investigation. These parameters are adjusted to fit the current experimental results. The results are given in table 5.1. It is assumed that the relation between d_{bed} and A or C is linear. The following expressions can be derived from the data in table 5.1:

$$A = 1.12 d_{bed} + 0.124 \tag{5.2a}$$

$$C = 0.318 d_{bed} + 0.45 \tag{5.2b}$$

The values for A and C are identical to the original Shen-correlation when a bed diameter of 0.68 m is substituted. The correlation now also fits bubble growth data obtained with the current setup. Results are given in figure D.3, page 70. However, the correlation does not restrict the bubble size, as it predicts that bubbles continue to grow. Therefore it still overestimates the bubble growth in the small bed. It is proposed that a threshold value must be used to restrict bubble growth at a certain point in the bed. An attempt will not be made in this report.

5.2.3 Bubble rise velocity

Investigating the bubble rise velocity equations is best performed with a broad bubble size distribution. These measurements provide enough data over a large d_b range. As shown in figure D.1b, the broadest distribution is obtained with bed heights at $h \geq$ 0.30 m. The bubble rise velocity is determined and compared to eq. 2.11 and eq. 2.12. The result is shown in figure 5.7. It is found that the correlation predicting the bubble rise velocity for a single bubble predicts the measured velocities quite well. However, the constant K_B, which is set to 0.711 for 3D beds has to be decreased slightly, to approximately $K_B = 0.6$, as is suggested by e.g. Mudde *et al.*[25]. The correction for wall effects proposed by Werther (eq. 2.13, page 11) incorporates the excess gas flow. This correlation shows less correspondence with experimental results than the correlation

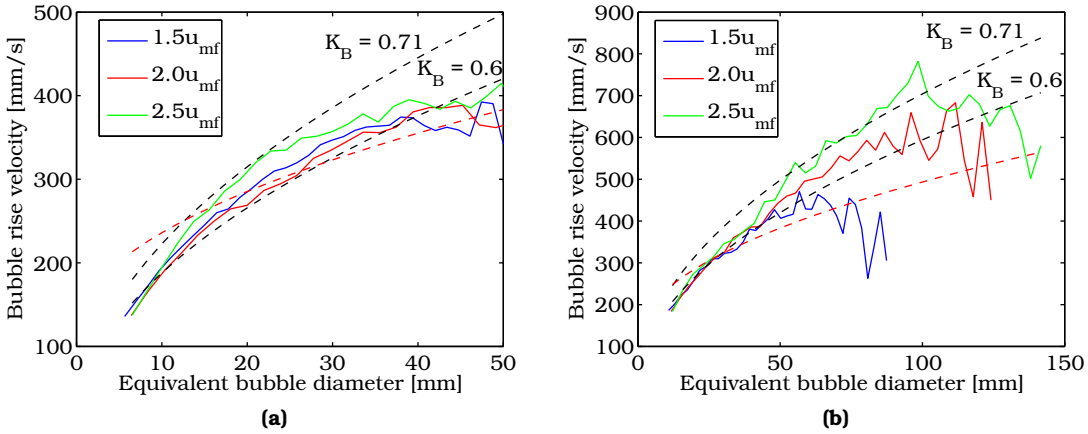

Figure 5.7: The experimental bubble rise velocity data compared to theoretical correlations. The black dashed lines represent the rise velocity for single bubbles; the red dashed lines give the predicted velocity for a swarm of bubbles at $2.5u_{mf}$, using Werthers correction for column diameter. Parameters: u_0 = 1.5,2.0,2.5u_{mf}; n = 40 classes. **(a)** $d_{bed} = 0.15$ m; h = 0.15 m; **(b)** $d_{bed} = 0.30$ m; h = 0.30 m.

for a single bubble. Therefore it is noted that Werthers correction is not suitable in its current form for pseudo-2D fluidized beds. The constants in his equation will have to be adapted in order to describe the bubble velocity in a pseudo-2D bed. However, the results are accurately described by a slightly adapted form of the single bubble rise velocity.
Due to the fact that small bubbles are disregarded by DIA, and the amount of bubbles with large diameters are scarce, the data is in the case of a small bed only reliably averaged in the range $10 \leq d_b \leq 50$ mm. This range extends to 80 mm in the case of the wide bed. This was verified by analysis of the bubble diameter distribution for these cases.

5.2.4 Bubble aspect ratio

Bubble-bubble interaction is observed when two bubbles are close to each other. The gas flows from the bubble at lower axial position to the higher positioned bubble, and the tailing bubble accelerates. Hereby, the leading bubble is flattened whereas the tailing bubble is elongated[3;9]. Detecting the aspect ratio of a bubble could give insight in this phenomenon.
The bubble aspect ratio is determined by the horizontal and vertical span of a single bubble. An investigation has shown that the aspect ratio is generally distributed between $0.2 \leq A_b \leq 3$, see figure 5.8a. At low superficial gas velocities, the bubbles are generally more flat than at higher superficial velocities. This is probably caused due to the increasing bubble-bubble interaction at higher superficial gas velocities. It was observed that low aspect ratios were mainly found in relatively small bubbles, whereas tall bubbles ($A_b \geq 1$) appeared to be of all sizes.
As Lim *et al.* suggested[30], a relation could be found between the aspect ratio of a bubble and the rise velocity. As seen in figure 5.8b, the superficial gas velocity barely has an influence on this relation. At this point, the velocity of a bubble for aspect ratio's between 0 and 2 can be described with a fitted equation:

$$u_b = 260\,(A_b)^{0.6} \tag{5.3}$$

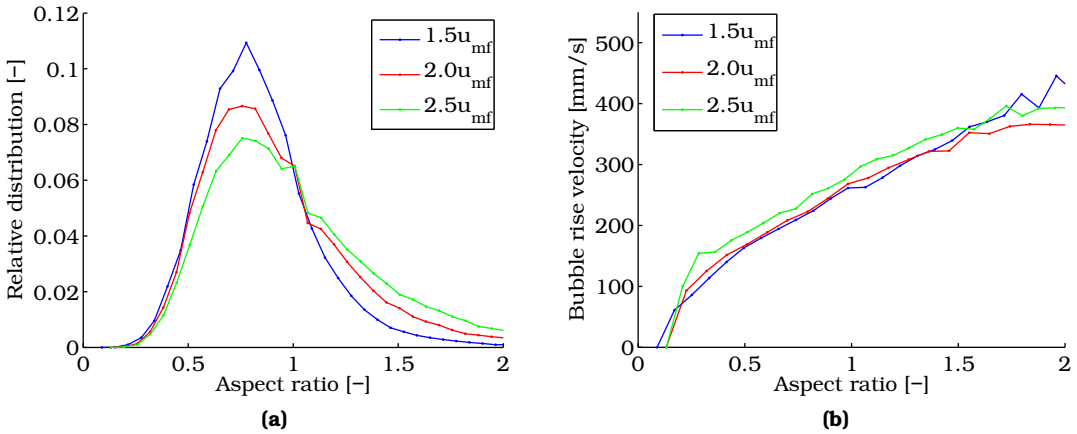

Figure 5.8: Selected results for aspect ratio studies Parameters: u_0 = 1.5,2.0,2.5u_{mf}; $d_{bed} = 0.15$ m; h = 0.15 m; n = 40 classes. **(a)** The distribution of the aspect ratio at different superficial gas velocities; Approximately 100000 bubbles were detected in each case; **(b)** The bubble rise velocity as a function of the aspect ratio.

It was found that for all other cases, this relation proved to predict the bubble rise velocity with the detected aspect ratio reasonably well. Figure D.4 on page 70 shows aspect ratio results for the wide bed.
With current results it can be shown that the rise velocity of a bubble and its aspect ratio share a relation. However, this trend has only been given in average terms, and besides bubble-bubble interaction other processes (e.g. break-up) take place. More research is required on the formation of elongated bubbles, before models can actually take advantage of this knowledge. It could be researched, for example, at what inter-bubble distances the bubbles tend to elongate. Only then a suitable correlation can be found to enhance models with shape-varying bubbles.

5.3 Two-way coupling

An investigation between bubble movement and emulsion phase flow gives insight into the relevant parameters for the coupling between the two phases. A method to describe the axial particle phase response to bubble movement is proposed in this section. First, a correlation will be derived. Consequently, experimental data will be used to test the correlation.

Correlation between particle and bubble movement

Experimental data of the time-averaged emulsion phase flow was presented in section 5.1. Because the lateral velocity profile is different at different heights in the bed, a comparison can only be made between bubble phase and emulsion phase at a single height z.
The DIA program was used to obtain the bubble parameters. The lateral and axial position of the bubbles were both divided into classes. A grid was defined as presented in figure 5.4. Every detected bubble was arranged in a single grid cell. A bubble is accounted for if it resides in the class at the axial position of interest. When all bubbles are placed on the grid, the properties of the bubble for every grid cell are averaged.
The particle phase is affected by various bubble properties. First of all, the diameter of a bubble d_b is of importance. A large bubble drags more particles in its wake than a small

bubble does. It also thrusts more particles aside. The wake area however, decreases when a bubble is elongated. Therefore, the aspect ratio A_b of a bubble is of importance to correct for the bubble shape. In addition, the emulsion phase moves faster if the bubble velocity u_b is higher. Finally, the frequency of bubbles in an area is used, as the emulsion phase shows little to no upward movement at locations where bubbles barely exist.
The emulsion phase upward flow u_p at height z as a function of the lateral position x can be described as a combination of these factors:

$$u_p(x,z) \propto \sqrt{\frac{\overline{u}_b(x,z)\overline{d}_b(x,z)}{\overline{A}_b(x,z)} f_b(x,z)} \tag{5.4}$$

In this thesis, the predicted value for u_p is compared to the time-averaged emulsion phase flow.

The correlation compared to the emulsion phase velocity

First, it must be mentioned that u_p obtained from eq. 5.4 is never negative. In fact, this is also true for the bubble properties derived from DIA. As the emulsion phase velocity is obviously also flowing down, hence encountering negative axial velocity, a comparison is made on the observed trend, and not on the absolute values.
For two cases, at two different heights, the experimental results are shown in figure 5.9. DIA information was classified by dividing the horizontal axis into 20 classes, and only accounting bubbles at desired height z up to z + 30 mm. After averaging the data per class, the average velocity, diameter, aspect ratio and bubble frequency can be substituted into equation 5.4. It can be seen that the trend of the equation (presented by the dashed lines labelled as 'Bubble') is comparable to the measured emulsion phase velocity (solid lines, obtained by PIV) at the same height.
A few remarks can be made based on these figures. First of all, the emulsion phase velocity profile is quite smooth, whereas the DIA result fluctuates severely. This is caused by the scarce availability of DIA information due to arrangement of bubbles into classes. Much of the DIA information has been disregarded because the bubbles were not found at the desired height. A validation of the proposed equation can therefore only be performed accurately with more bubble data.
Attempts have been made to modify equation 5.4 so that it would predict the absolute emulsion phase velocity. Obviously, the resulting velocity u_p from equation 5.4 has to be translated downward in order to yield the negative axial emulsion phase velocity at the walls. As the emulsion phase velocity (either up or down) increases at higher superficial gas velocities, the excess gas flow should be accounted for in the translation. A resulting correlation would look like:

$$u_p(x,z) \simeq F\left(-0.65\,(u_0 - u_{mf}) + \sqrt{\frac{\overline{u}_b(x,z)\overline{d}_b(x,z)}{\overline{A}_b(x,z)} f_b(x,z)}\right) \tag{5.5}$$

in which F is an unknown factor. An attempt has been made to obtain a value for F, and to acquire verification of the translation step. With the current data, unfortunately, these values remain elusive. Results of the latter equation are therefore not presented here, as they require more study.

The bubble velocity is typically found in the range of 0.1 - 0.7 m/s. The upward emulsion phase velocity of the equivalent PIV case is about 1/3 - 1/2 of the bubble velocity. Similar numbers are reported in literature (Stein *et al.*[13]). However, Stein *et al.* did not measure the bubble properties, but they used theoretical relations to obtain them. Besides studying the *average* bubble and emulsion phase velocities, the interaction

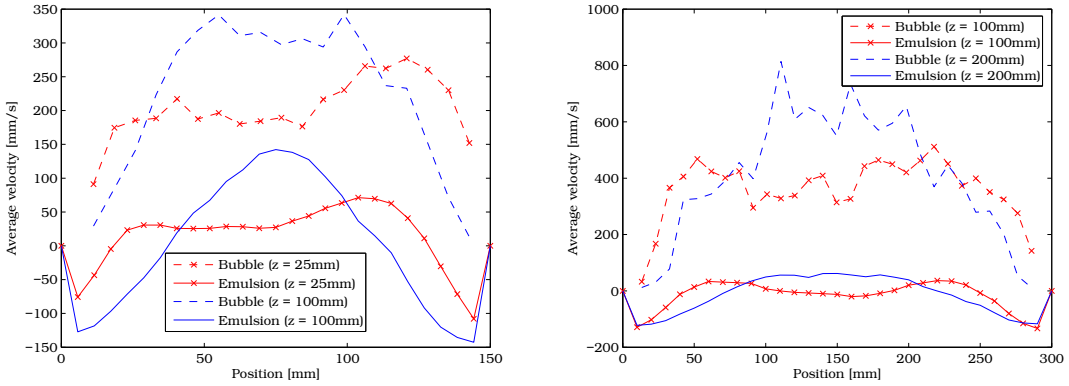

Figure 5.9: The result of eq. 5.4 ('Bubble') compared to the measured emulsion phase velocity in two cases at two heights **(a)** u_0 = 2.5u_{mf}; $d_{bed} = 0.15$ m; h = 0.15 m; n = 20 classes. z = 25, 50 mm; **(b)** u_0 = 2.5u_{mf}; $d_{bed} = 0.30$ m; h = 0.30 m; n = 30 classes. z = 100, 200 mm;.

between the bubble and particle phase can also be studied from instantaneous flow patterns. Dedicated experiments have to be performed, creating images for both PIV and DIA analysis. A single bubble experiment is performed (see e.g. figure 3.3), but a series of similar experiments are required to quantify the interaction. The flow of particles below the bubble can then be quantified.
In this section, it was shown that it is likely that the average emulsion phase velocity can be determined with results from the DIA program. It would be highly desirable to accurately predict the vertical emulsion phase flow, only with bubble data. Existing correlations are able to predict the bubble properties accurately. If these properties could yield a good description of the emulsion phase, a new model based on phenomenological correlations can be proposed.
Additional experiments, gaining large amounts of data for the DIA program, should be performed in order to investigate the coupling in more detail. It has been investigated which bubble parameters are supposedly of importance when studying the interaction phenomenon.

Chapter 6

Conclusions and Recommendations

6.1 Conclusions

The hydrodynamics of the particle phase and the behavior of the bubble phase in a gas-solid fluidized bed were experimentally investigated using two non-invasive optical techniques. The bed consisted of glass beads in the Geldart B range. The superficial gas velocity was varied between 1.5 and 3.5u_{mf}, and the aspect ratio of the bed ranges from 0.3 to 2. To conduct the investigation, several programs have been developed as described in this thesis.

A novel method has been proposed to perform PIV analysis on granular systems reliably. Due to particle raining through the bubbles, the raw PIV vector data contains many large downward vectors, based on only a few particles, that have a severe impact on the time-averaged emulsion phase flow pattern. The new method combines two non-invasive measuring techniques. The first technique yields the location of bubbles on an image. The second is PIV, needed to obtain the instantaneous flow pattern. The proposed method combines both results to filter instantaneous vectors that are located in a bubble. The correction algorithm was found to have a significant influence on the emerging time-averaged emulsion phase flow patterns. The method results in a more pronounced upward flow of particles, which is found for all cases.

Several other algorithms supporting PIV analysis were developed. Large bed areas cannot be photographed as a whole due to restrictions on PIV image resolution. The bed behavior can be recorded in several instances. Each instance covers a different part of the full bed, which in total cover the full bed area. The time-averaged flow patterns of the individual instances can be combined by a stitching program. Moreover, a method to investigate the reproducibility of PIV experiments was developed. It was shown that the PIV recording schemes used for this investigation yielded reproducible time-averaged results, when at least 200 instantaneous vector fields are employed.

Using a pseudo-2D setup, the hydrodynamics of the particles was investigated using PIV and the proposed correction algorithm. Downflow was observed at the walls and the upward flow area stretch from the lower wall region up to the center of the bed. The velocity of the particles was shown to increase significantly at increasing superficial gas flow. Increasing the bed height does not influence the main bubble path; at low aspect ratios bubbles erupt at the surface before shifting to the center.

Furthermore, a digital image analysis algorithm has been developed. The algorithm obtains bubble parameters from a series of images. Among others, it accounts for the position, velocity and shape of the bubbles on the images. The algorithm was validated using synthetic images. Also, the bubble parameters obtained with DIA showed a good reproducibility when importing more than 2000 images into DIA.

The walls of the reactor do not only restrict the bubbles to a maximum size. Changing the bed width also affects the distribution of smaller bubbles. A correlation, describing the bubble growth as a function of the height in a pseudo-2D bed, was obtained from literature. The correlation largely overpredicts the bubble size in the current setup due to differences in bed width. Therefore, the correlation was adapted to fit both the experiments of Shen *et al.* and the results of the present studies. The adapted correlation shows good agreement with current experiments, however, it has to be verified whether the correlation shows good predictions of other bed sizes.

The bubble rise velocity was best predicted by the equation for a single rising bubble, although with a slightly different coefficient K_B of 0.6. This result confirms literature reports on this subject. Besides, the aspect ratio of a bubble and the rise velocity are shown to be related. The derived equation is found to be valid for different superficial gas flows, bed diameters and aspect ratios.

A proposal has been formulated to study the two phase interaction. Current experiments provide too little data to formulate a generic expression for the coupling. However, the relevant parameters d_b, u_b, A_b and f_b were identified by observing a similar trend between emulsion phase velocity and the derived equation.
The experiments have shown that the developed DIA program is able to measure a large variety of parameters accurately. PIV results are improved by the correction algorithm. While all the tools needed are complete and have been tested thoroughly, the next step is to study the coupling between the phases in more detail.

6.2 Recommendations

The correction algorithm can be set more strictly, by completely disregarding vectors that are partially based on a low packed bed area. The current implementation still considers these vectors for a part. This might be necessary to prevent the velocity of the wake particles, which adjoin the bubble, to be filtered out. Another way is to decrease the size of a PIV interrogation zone. If a PIV algorithm and the DIA algorithm can be combined in a single program, the bubble areas on the images can be marked before PIV takes place. These parts should then not even take part in the correlation step of PIV. If this is possible, filtering erroneous vectors is not necessary anymore.
The effect of the correction algorithm should be investigated on larger and smaller particle systems. Because PIV gains more and more attention for measurements of granular systems, it is necessary to state new PIV design rules when correction is absolutely necessary, and when conventional PIV might suffice.

This work does not extrapolate the obtained pseudo-2D results, of neither PIV nor DIA, to a 3D geometry. In order to quantify the differences in particle flow for these geometries, experiments have to be performed in 3D beds. The experiments will be performed using the PEPT technique. Experiments should be performed preferably in a bed with d_{bed} = 0.30 m. These results suffer the least from an asymmetric flow profile and are obtained at a higher resolution. Also, the effect of wall influences is smaller than experiments in the 0.15 m bed. Once the differences between pseudo-2D and 3D are quantified, experiments investigating the bubble-particle phase interaction in detail can be

interpreted well.

The minimum fluidization velocity of the particles used for this investigation was determined experimentally. The obtained u_{mf} was found to be slightly lower than the theory predicts. For 3D experiments, the u_{mf} should be determined again in a 3D geometry. It should also be investigated why bubbles in the small bed are collapsing, yielding asymmetric and unexpected results.

The adapted Shen-correlation must be tested with different bed diameters. The correlation currently fits results obtained in three beds with a different diameter, but if the equation is generic it should also predict the bubble size in other bed sizes. The same applies to the expression relating the bubble aspect ratio and rise velocity. Once these expressions are validated, the results can be used in model studies.

The coupling between the phases should be investigated thoroughly. By recording images suitable for both PIV and DIA, instantaneous flow patterns and bubble properties can be determined from a single images series. These simulations and experiments can only be performed on a small scale (0.12×0.15 m), but can yield valuable information considering the direct bubble-particle phase interaction. Besides instantaneous comparison between the phases, a comparison between the average behavior of bubbles and emulsion phase should take place. The proposed equation for coupling can only be verified using more DIA information than in the current work.
The coupling equation requires bubble parameters that can be obtained using phenomenological correlations. If such a correlation is verified, a new model can be proposed, predicting the emulsion phase behavior from bubble phase input data.

Bibliography

[1] J. Werther. *Ullmans Encyclopedia of Industrial Chemistry*. Wiley-VCH Verlag GmbH Co. KGaA, 2002.

[2] J.I. Holcomb and J.F. Hoke Jr. Patent: Popcorn-machine. patent number: Us 1195017 (filing date: 28/12/1914), August 1916.

[3] D. Kunii and O. Levenspiel. *Fluidization Engineering*. Butterworth-Heinemann, 1991.

[4] G.A. Bokkers. *Multi-Level Modelling of the Hyrodynamics in Gas Phase Polymerisation Reactors*. PhD thesis, University of Twente, 2005.

[5] R. Beetstra. *Drag Force in Random Arrays of Mono- and Bidisperse Spheres*. PhD thesis, University of Twente, 2005.

[6] M.A. van der Hoef, M. Ye, M. van Sint Annaland, A.T. Andrews, S. Sundaresan, and J.A.M. Kuipers. Multiscale modeling of gas-fluidized beds. *Advances in Chemical Engineering*, 31:65–149, 2006.

[7] J.A.M. Kuipers, K.J. Van Duin, F.P.H. Van Beckum, and W.P.M. Van Swaaij. A numerical model of gas-fluidized beds. *Powder Technology*, 47(8):1913–1924, 1992.

[8] G.A. Bokkers, J.A. Laverman, M. van Sint Annaland, and J.A.M. Kuipers. Modelling of large-scale dense gas-solid bubbling fluidised beds using a novel discrete bubble model. *Chem. Eng. Sci.*, 61(17):5590–5602, 2006.

[9] R. Clift and J.R. Grace. *Continuous Bubbling and Slugging in: FLUIDIZATION, 2nd ed.* Academic Press, 1985.

[10] D. Geldart. Types of gas fluidization. *Powder Technology*, 7(5):285–292, 1973.

[11] S. Deshmukh. *Membrane Assisted Fluidized Bed Reactor: Experimental Demonstration for Partial Oxidation of Methanol*. PhD thesis, University of Twente, 2004.

[12] F. Larachi, J. Chaouki, G. Kennedy, and M.P. Duduković. *Non-Invasive Monitoring of Multiphase Flows, pp. 335-406 (Chapter 11).* Elsevier, New York, 1997.

[13] M. Stein, Y.L. Ding, J.P.K. Seville, and D.J. Parker. Solids motion in bubbling gas fluidised beds. *Chem. Eng. Sci.*, 55:5291–5300, 2000.

[14] N. Mostoufi and J. Chaouki. Flow structure of the solids in gas-solid fluidized beds. *Chem. Eng. Sci.*, 59:4217–4227, 2004.

[15] J.M. Link. *Development and validation of a Discrete Particle Model of a Spout-Fluid Bed Granulator*. PhD thesis, University of Twente, 2006.

[16] G.A. Bokkers, M. van Sint Annaland, and J.A.M. Kuipers. Mixing and segregation in a bi-disperse gas-solid fluidised bed: A numerical and experimental study. *Powder Technology*, 140:176–186, 2004.

[17] J. Westerweel. Fundamentals of digital particle image velocimetry. *Meas. Sci. Technol.*, 8:1379–1392, 1997.

[18] R.J. Adrian. Dynamic ranges of velocity and spatial resolution of particle image velocimetry. *Meas. Sci. Technol.*, 8:1393–1398, 1997.

[19] D. Geldart. The size and frequency of bubbles in two- and three-dimensional gas-fluidised beds. *Powder Technology*, 4:41–55, 197071.

[20] D. Gera and M. Gautam. Effect of bubble coalescence on throughflow velocity in a 2d fluidized bed. *Powder Technology*, 83:49–53, 1995.

[21] D.J. Patil. *An Experimental and Computational Study of Dense Gas-Solid Fluidized Beds*. PhD thesis, University of Twente, 2003.

[22] K.S. Lim, V.S. Gururajan, and P.K. Agarwal. Mixing of homogeneous solids in bubbling fluidized beds: Theoretical modelling and experimental investigation using digital image analysis. *Chem. Eng. Sci.*, 48(12):2251–2265, 1993.

[23] L. Shen, F. Johnsson, and B. Leckner. Digital image analysis of hydrodynamics two-dimensional bubbling fluidized beds. *Chem.Eng.Sci.*, 59:2607–2617, 2004.

[24] A.S. Hull, Z. Chen, J.W. Fritz, and P.K. Agarwal. Influence of horizontal tube banks on the behavior of bubbling fluidized beds: 1. bubble hydrodynamics. *Powder Technology*, 103(3):230–242, 1999.

[25] R.F. Mudde, H.B.M. Schulte, and H.E.A. van den Akker. Analysis of a bubbling 2-d gas-fluidized bed using image processing. *Powder Technology*, 81(2):149–159, 1994.

[26] R. Collins. The effect of a containing cylindrical boundary on the velocity of a large gas bubble in a liquid. *J. Fluid Mech.*, 28:97–112, 1967.

[27] R. Krishna and J.M. van Baten. Using cfd for scaling up gas-solid fluidised beds reactors with geldart a powders. *Chemical Engineering Journal*, 82:247–257, 2001.

[28] K.S. Lim, P.K. Agarwal, and B.K. O'Neill. Measurement and modelling of bubble parameters in a two-dimensional gas-fluidized bed using image analysis. *Powder Technology*, 60:159–171, 1990.

[29] G. Ramos Caicedo, J.J. Prieto Marqués, M. García Ruíz, and J. Guardiola Soler. Measurement and modelling of bubble parameters in a two-dimensional gas-fluidized bed using image analysis. *Powder Technology*, 60:159–171, 1990.

[30] K.S. Lim and P.K. Agarwal. Bubble velocity in fluidized beds: the effect of non-vertical rise on its measurement using submersible probes and its relationship with bubble size. *Powder Technology*, 69:239–248, 1992.

[31] P.K. Agarwal, A.S. Hull, and K.S. Lim. *Non-Invasive Monitoring of Multiphase Flows, pp. 335406 (Chapter 12).* Elsevier Science BV, New York, 1996.

[32] N. Kobayashi, R. Yamazaki, and S. Mori. A study on the behavior of bubbles and solids in bubbling fluidized beds. *Powder Technology*, 113:327–344, 2000.

[33] J. Villa Briongos and Jesús Guardiola. New mothodology for scaling hydrodynamic data from a 2d-fluidized bed. *Chemical Engineering Science*, 60:5151–5163, 2005.

[34] P. Harriott. *Chemical Reactor Design*. CRC Press, 2003.

[35] Y. Sugii, S. Nishio, T. Okuno, and K. Okamoto. A highly accurate iterative piv technique using a gradient method. *Meas. Sci. Technol.*, 11:1666–1673, 2000.

[36] J. Collignon. Experimental validation of a discrete particle model for vibrated beds. Master's thesis, University of Twente, 2005.

[37] R.D. Keane and R.J. Adrian. Optimization of particle image velocimeters: Ii. multiple pulsed systems. *Meas. Sci. Technol.*, 2:963–974, 1991.

[38] W. Dijkhuizen. Validation of a continuum model, based on the kinetic theory of granular flow, with discrete particle simulations and experiments based on particle image velocimetry. Master's thesis, University of Twente, 2003.

Appendix A

PIV Design Rules

Many refinements have been made to improve the accuracy of PIV. The velocity bias is an important aspect which has to be dealt with. Also, accuracy on sub-pixel scales has been investigated. Some basic rules needed to perform accurate experiments with PIV are explained in this section.
In order to optimally identify the displacement peak R_D, design rules have been specified[17;18;35;36] by Adrian and Keane (e.g.[37]) after Monte Carlo simulations. Westerweel (1997) has summarized them for high image density PIV[17]:

$$N_I F_I F_O > 7 \tag{A.1}$$

The number of particles in each interrogation area, N_I, is multiplied by the in-plane particle loss calculated (see equation A.3b) and the out-of-plane particle movement, F_O. Both F_I and F_O should be larger than 0.75. This means that less than one quarter of all particles in an interrogation window are allowed to move out of this window. To calculate N_I we use a cubically packed structure of particles which are being tracked[36]:

$$N_I = \left(\frac{N}{d_p \cdot M} \right)^2 \cdot f_t \tag{A.2}$$

in which N is the total number of particles, d_p is the diameter of the particles and M a factor to convert pixels to millimeters. The fraction of tracer particles f_t is set to 1 as all particles in the field of view are being tracked.
Fast moving particles or velocity gradients in an interrogation area account for an error termed velocity bias. Because the number of particle-image pairs decreases at higher velocities, the system is biases towards lower velocities (see figure A.1). Dividing the spatial correlation by $F_I(x, y)$ (equation A.3), or the use of window shifting with different sizes compensates for the decrease of interrogation area.

$$R(x, y) = \frac{\hat{R}(x, y)}{F_I(x, y)} \tag{A.3a}$$

$$F_I(x, y) = \left(1 - \frac{x - x_c}{N_x} \right) \left(1 - \frac{y - y_c}{N_y} \right) \tag{A.3b}$$

Window shifting creates a ballpark estimate of the flow field with large interrogation areas, followed by correlation of smaller areas. Because the general displacement is known, the correlation window can be shifted in the direction of the estimate. As stated before, gradients can also cause a velocity bias. The displacement correlation peak is

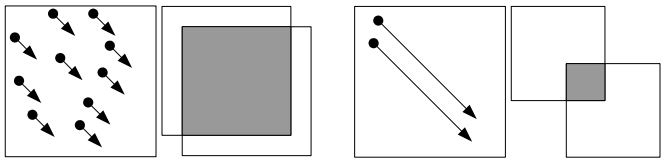

Figure A.1: The velocity bias principle explained by (left) slow moving particles yielding many correlated particles and (right) fast moving particles, decreasing the size of the interrogated zone. From Westerweel (1997)[17].

broadened as particles in the interrogation window have different velocities. The velocity distribution can be assumed to be Gaussian and the peak can be corrected, ruling out velocity differences within the interrogation zone. To consider uniform displacement however, the following relation has to be taken into account:

$$M|\Delta u|\Delta t \ll d_t \tag{A.4}$$

Small interrogation windows might yield mismatched correlation, which is why typically windows of 32x32 or more pixels are chosen[35]. A typical error margin for 32x32 pixel windows is estimated to be 0.05 – 0.1 pixels[17], which is expected to be adequate for our measurements.
Furthermore, it was determined that a tracked particle should be represented by at least three picture elements (pixels)[36–38]. The ultimate spatial resolution of a PIV result is determined by one's ability to track individual particles[18].

Appendix B

Edge Detection

Edge detection is a part of the DIA program. It was initially implemented to separate bubbles from emulsion phase, but it was shown that the edge between bubbles and emulsion phase is a gradient rather than a strong edge. The edge detection can however be used to separate the freeboard from the particles, as this border is usually quite sharp.
The edge between the freeboard and the particles in the bed is not a static horizontal line due to eruptions of bubbles, waves at the surface and bed expansion which is why a removal of a static number of rows from the top would not work. But, it can be assumed that the difference of intensity between pixels on the bed and pixels of the background is high. A differentiation operator, commonly known as an edge detection algorithm, can detect such intensity differences, based on a combinarion of the vertical and horizontal gradient. Further explanation can be found in figure B.1. Several finite difference edge detection algorithms were tested, because they are fast and easy to implement. A 5×5 convolution mask is less sensitive to changes in a small area. It was observed that a Sobel mask, which takes direct (horizontal, vertical) neighbors more strongly into account than diagonally adjacent pixels, performed better than, for example, a Prewitt mask. The result of the edge detection can be found in the first image of figure 3.1b. Obviously, a large part of the edge can be detected, but when a bubble erupts, the freeboard boundary is still not specified clearly. Using empirical techniques, the freeboard is defined throughout the bed without having to rely on edge detection solely. The final resulting freeboard can be found in the second image of figure 3.1b.

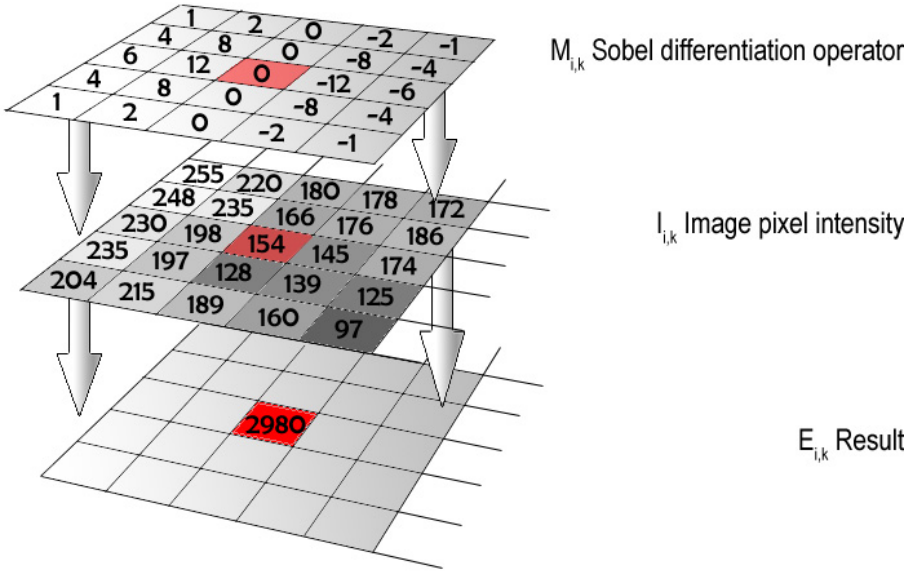

Figure B.1: Explanation of the 5×5 Sobel Edge Detection; The Sobel operator (upper layer) is over all of the pixels of the image (second layer). The values of the mask $M_{i,j}$ are multiplied by the pixel intensities $I_{i,j}$ directly below it, and summed for the center pixel. This yields a high value if an intensity gradient is found, or a low value if surrounding pixels around the red square are quite similar. With the mask shown, edges only in 1 direction are found (e.g. vertical). The mask must be rotated $90°$ to find edges with another orientation (e.g. horizontal). The values of the edge matrix $E_{i,j}$ can be found after taking the root of their squared sum.

Appendix C

Particle flow patterns

This appendix outlines the resulting time averaged flow patterns for the cases which were not given in the report. It also gives the vertical velocity component as a function of the lateral position for different heights. Note that the scale of the figures is adjusted according to the velocities encountered.
The experimental parameters are given in the captions of the figures. A short list of all results is given here, with the bed diameter d_{bed}, unfluidized bed height h, bed aspect ratio h/d_{bed} and the superficial gas velocities u_0.

Bed size	d_{bed} [m]	h [m]	$h/d_{bed}[-]$	u_0/u_{mf} [-]	Figure	Page
Wide	0.30	0.1	0.33	1.5; 2.0; 2.5; 3.5	C.1	59
Wide	0.30	0.15	0.5	1.5; 2.0; 2.5; 3.5	C.2	60
Wide	0.30	0.30	1.0	1.5; 2.0;	C.3	61
Wide	0.30	0.30	1.0	2.5; 3.5;	C.4	62
Wide	0.30	0.45	1.5	1.5; 2.0; 2.5;	5.2	37
Small	0.15	0.075	0.5	1.5; 2.0; 2.5; 3.5	C.5	63
Small	0.15	0.15	1.0	1.5; 2.0; 2.5	C.6	64
Small	0.15	0.15	1.0	3.5; 6.0	C.7	65
Small	0.15	0.30	2.0	1.5; 2.0	C.8	66
Small	0.15	0.30	2.0	2.5; 3.5	C.9	67

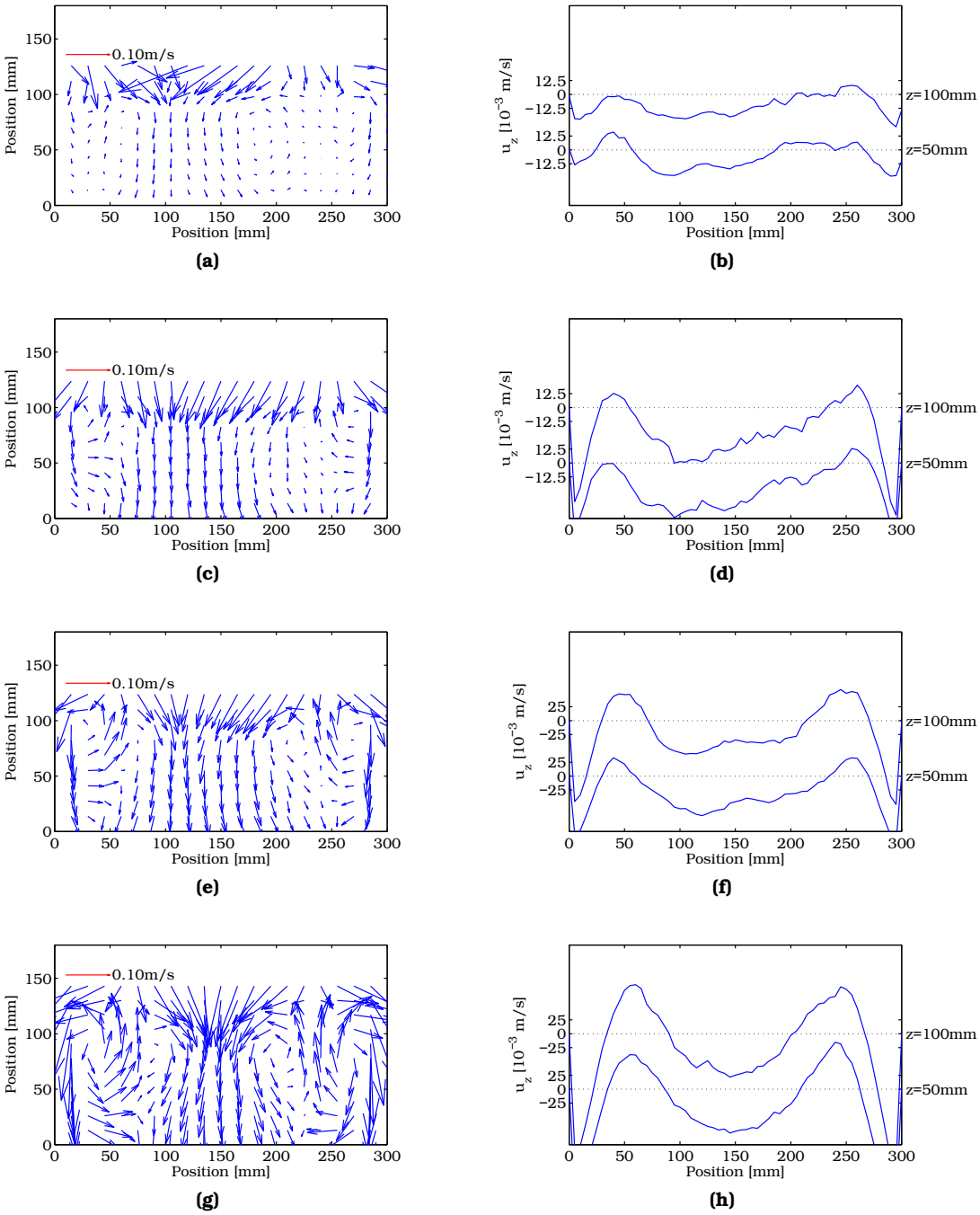

Figure C.1: Parameters: d_{bed} = 0.30 m; h_{bed} = 0.1 m; **(a)+(b)** u_0 = $1.5u_{mf}$; **(c)+(d)** u_0 = $2.0u_{mf}$; **(e)+(f)** u_0 = $2.5u_{mf}$; **(g)+(h)** u_0 = $3.5u_{mf}$;

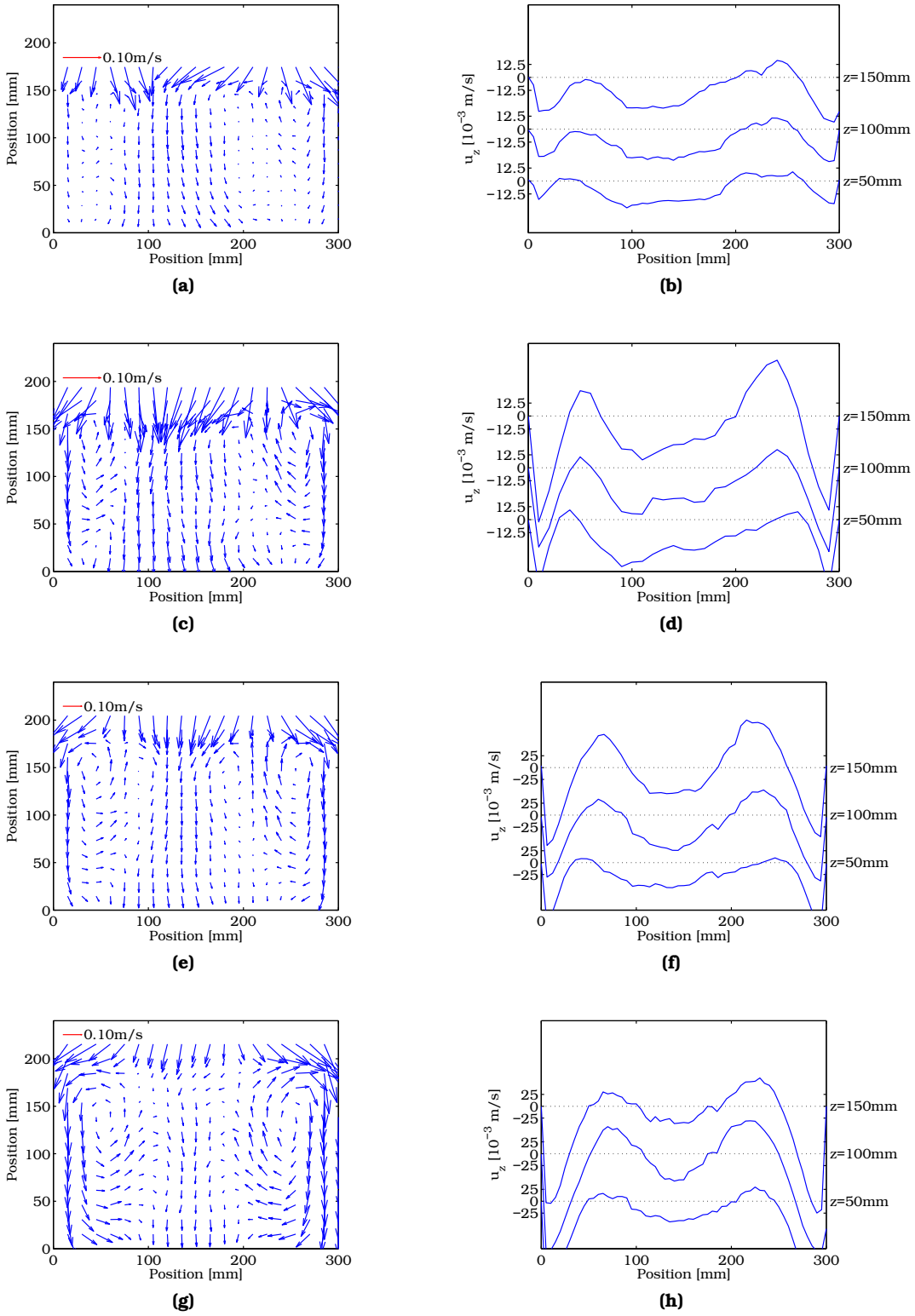

Figure C.2: Parameters: d_{bed} = 0.30 m; h_{bed} = 0.15 m; **(a)+(b)** $u_0 = 1.5u_{mf}$; **(c)+(d)** $u_0 = 2.0u_{mf}$; **(e)+(f)** $u_0 = 2.5u_{mf}$; **(g)+(h)** $u_0 = 3.5u_{mf}$;

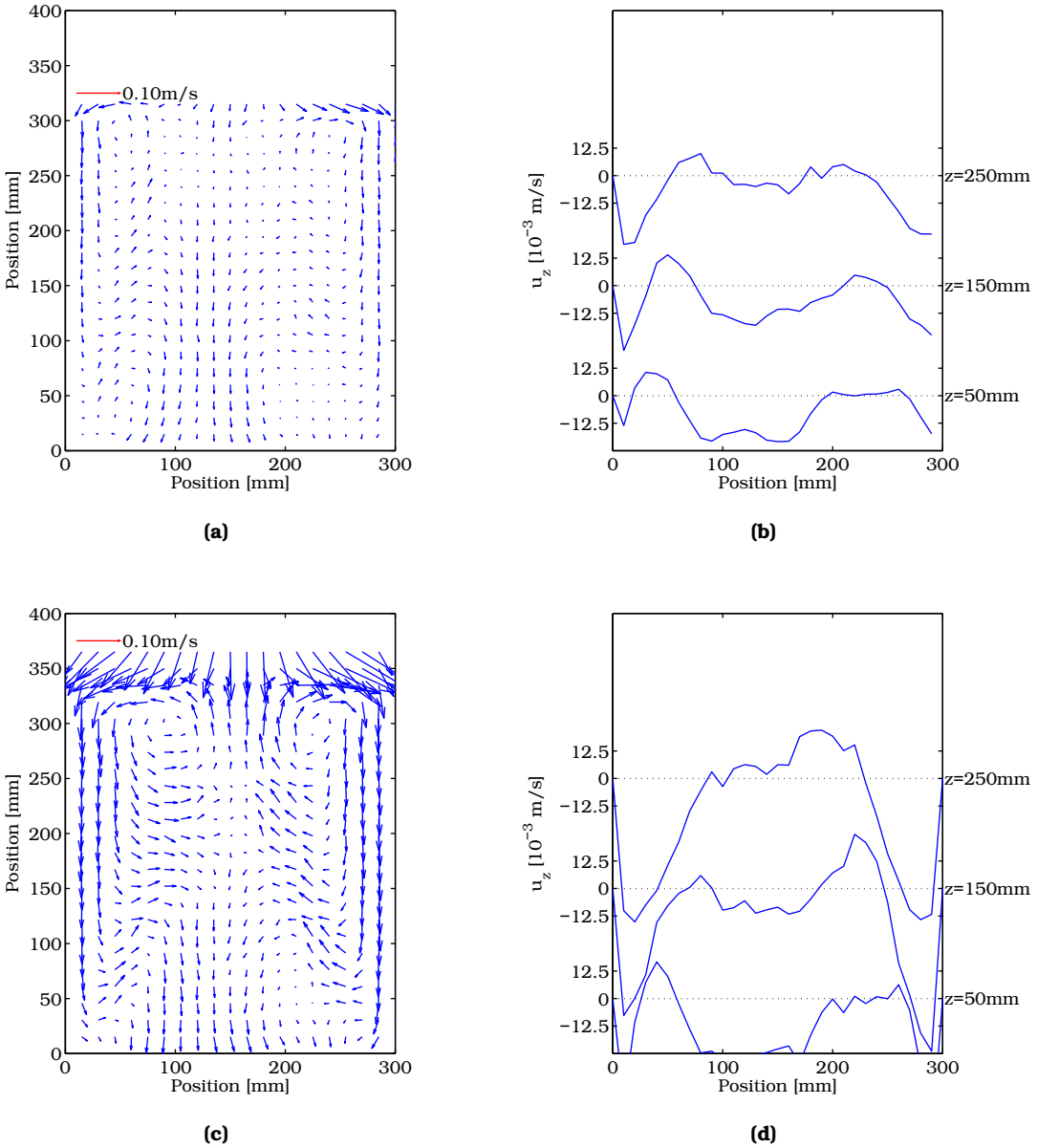

Figure C.3: Parameters: d_{bed} = 0.30 m; h_{bed} = 0.30 m; **(a)+(b)** u_0 = 1.5u_{mf}; **(c)+(d)** u_0 = 2.0u_{mf};

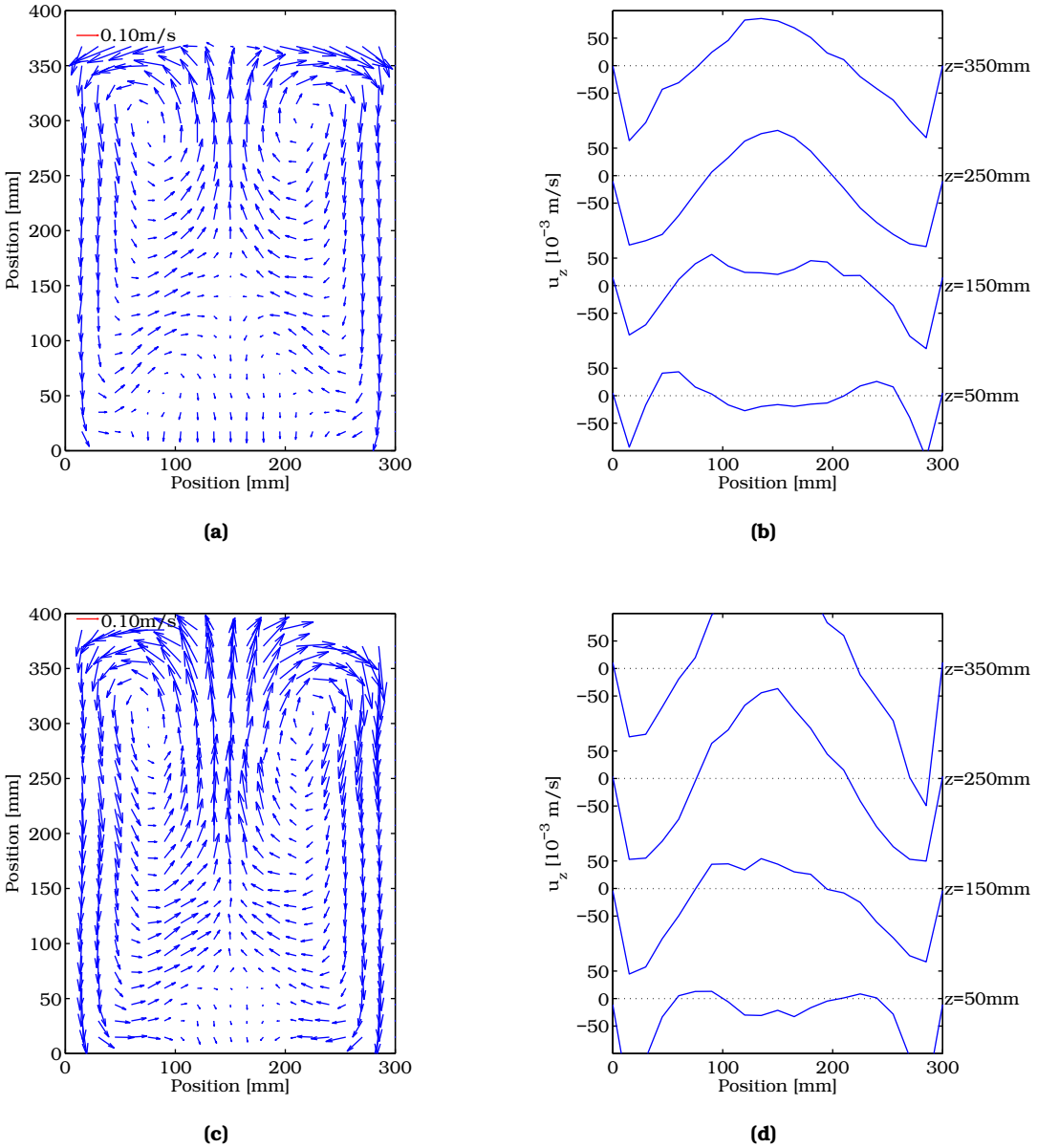

Figure C.4: Parameters: d_{bed} = 0.30 m; h_{bed} = 0.30 m; **(a)+(b)** $u_0 = 2.5u_{mf}$; **(c)+(d)** $u_0 = 3.5u_{mf}$;

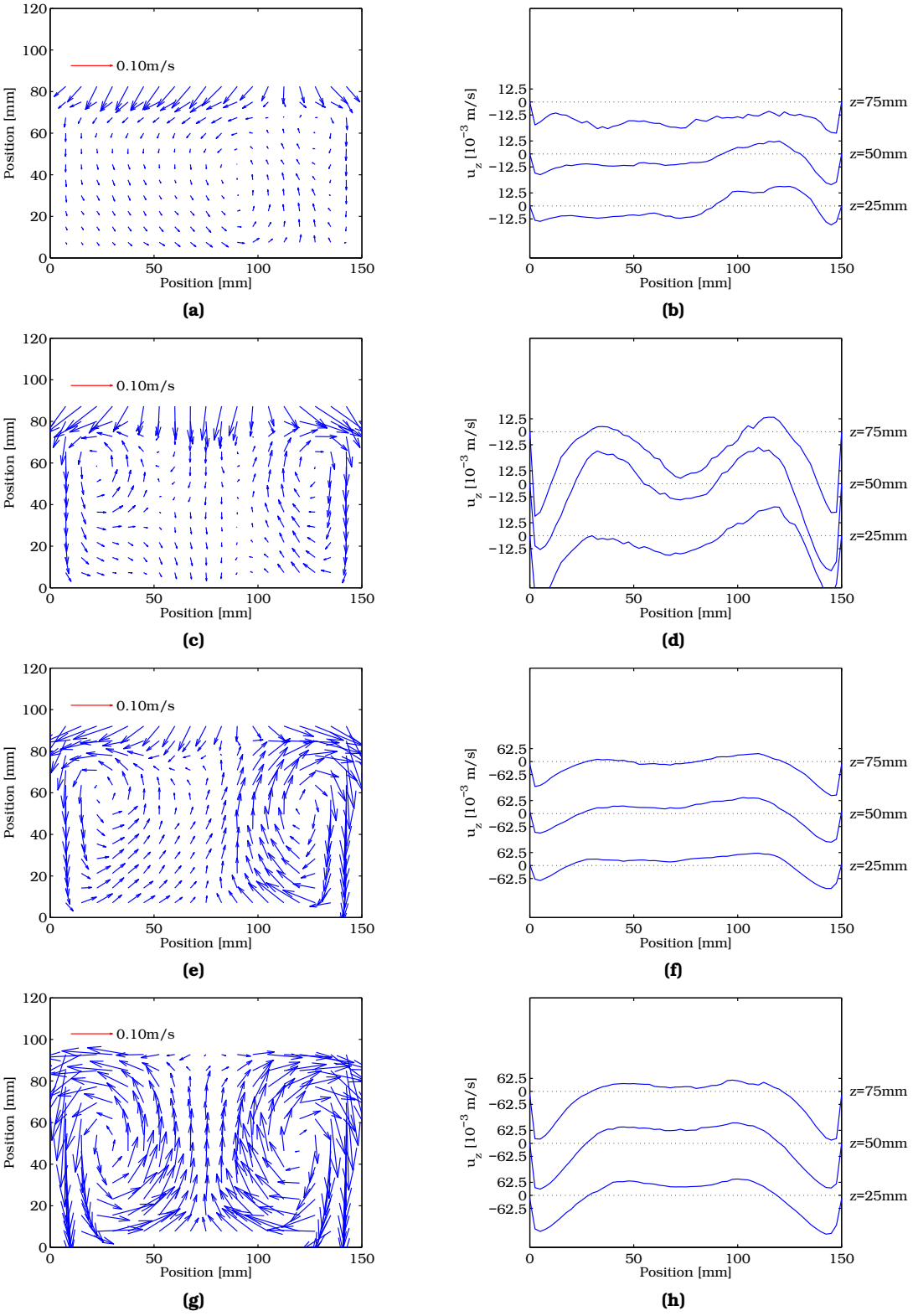

Figure C.5: Parameters: d_{bed} = 0.15 m; h_{bed} = 0.075 m; **(a)+(b)** u_0 = $1.5u_{mf}$; **(c)+(d)** u_0 = $2.0u_{mf}$; **(e)+(f)** u_0 = $2.5u_{mf}$; **(g)+(h)** u_0 = $3.5u_{mf}$;

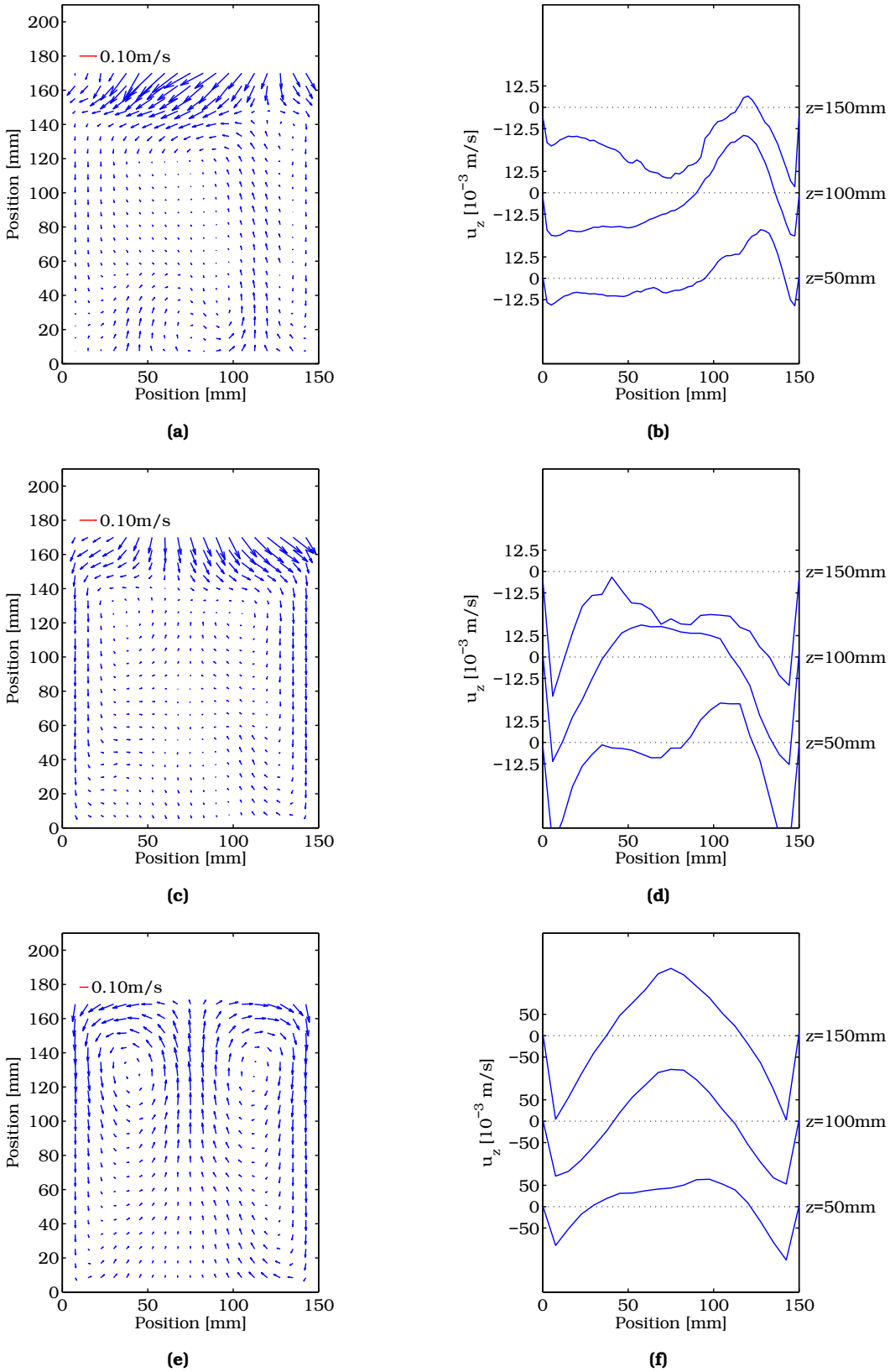

Figure C.6: Parameters: d_{bed} = 0.15 m; h_{bed} = 0.15 m; **(a)+(b)** u_0 = 1.5u_{mf}; **(c)+(d)** u_0 = 2.0u_{mf}; **(e)+(f)** u_0 = 2.5u_{mf};

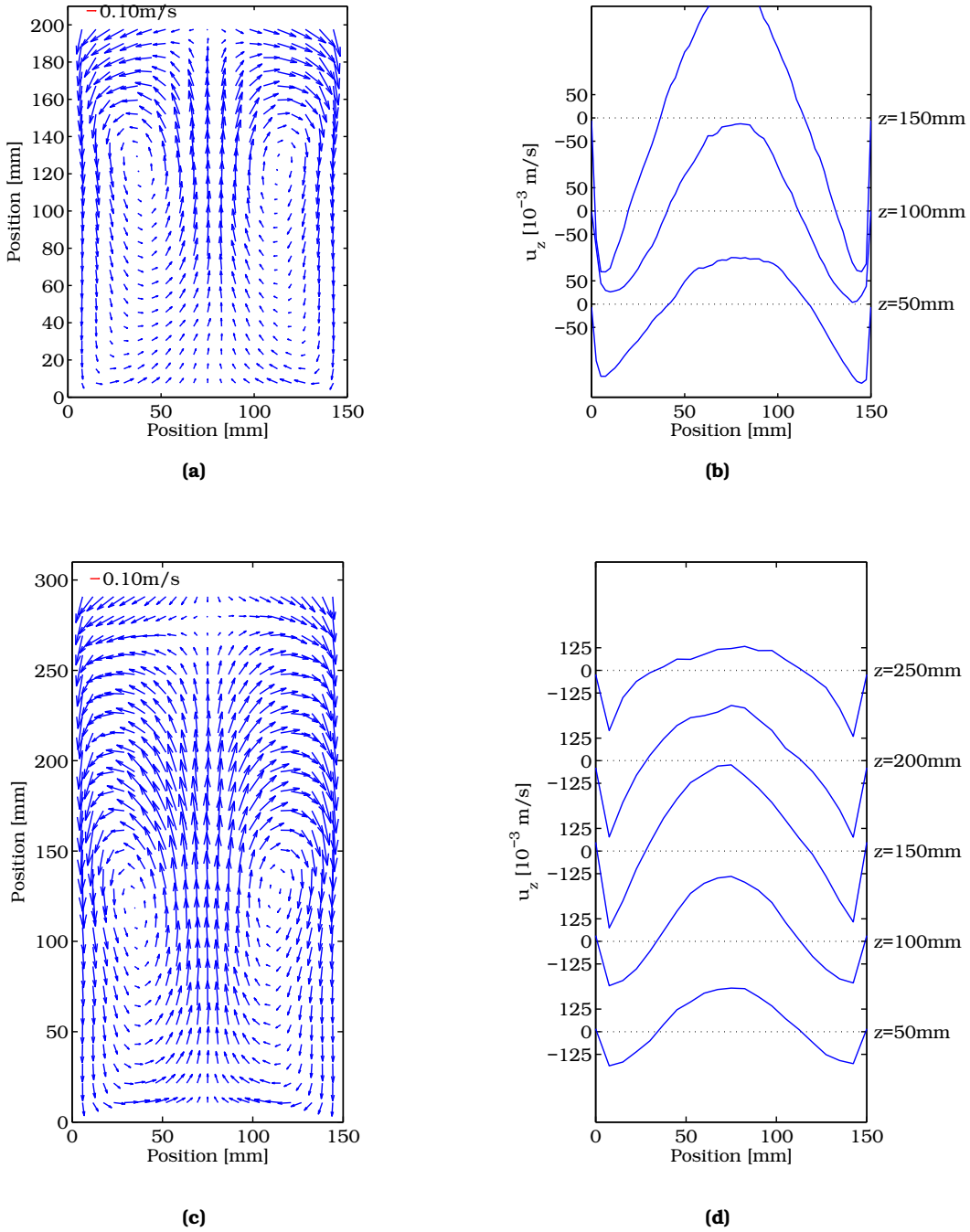

Figure C.7: Parameters: d_{bed} = 0.15 m; h_{bed} = 0.15 m; **(a)+(b)** $u_0 = 3.5u_{mf}$; **(c)+(d)** $u_0 = 6.0u_{mf}$;

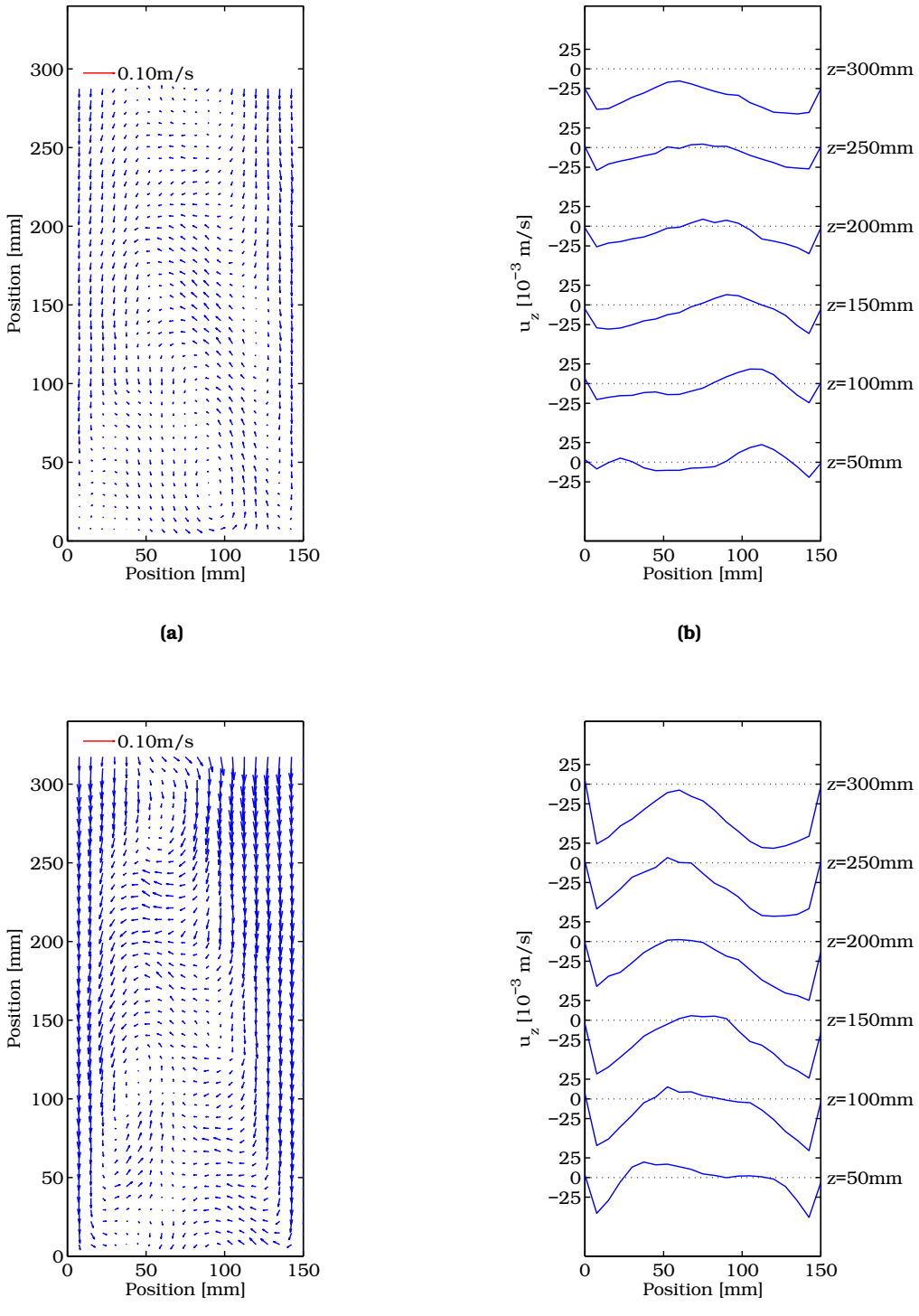

Figure C.8: Parameters: d_{bed} = 0.15 m; h_{bed} = 0.30 m; **(a)+(b)** $u_0 = 1.5u_{mf}$ **(c)+(d)** $u_0 = 2.0u_{mf}$

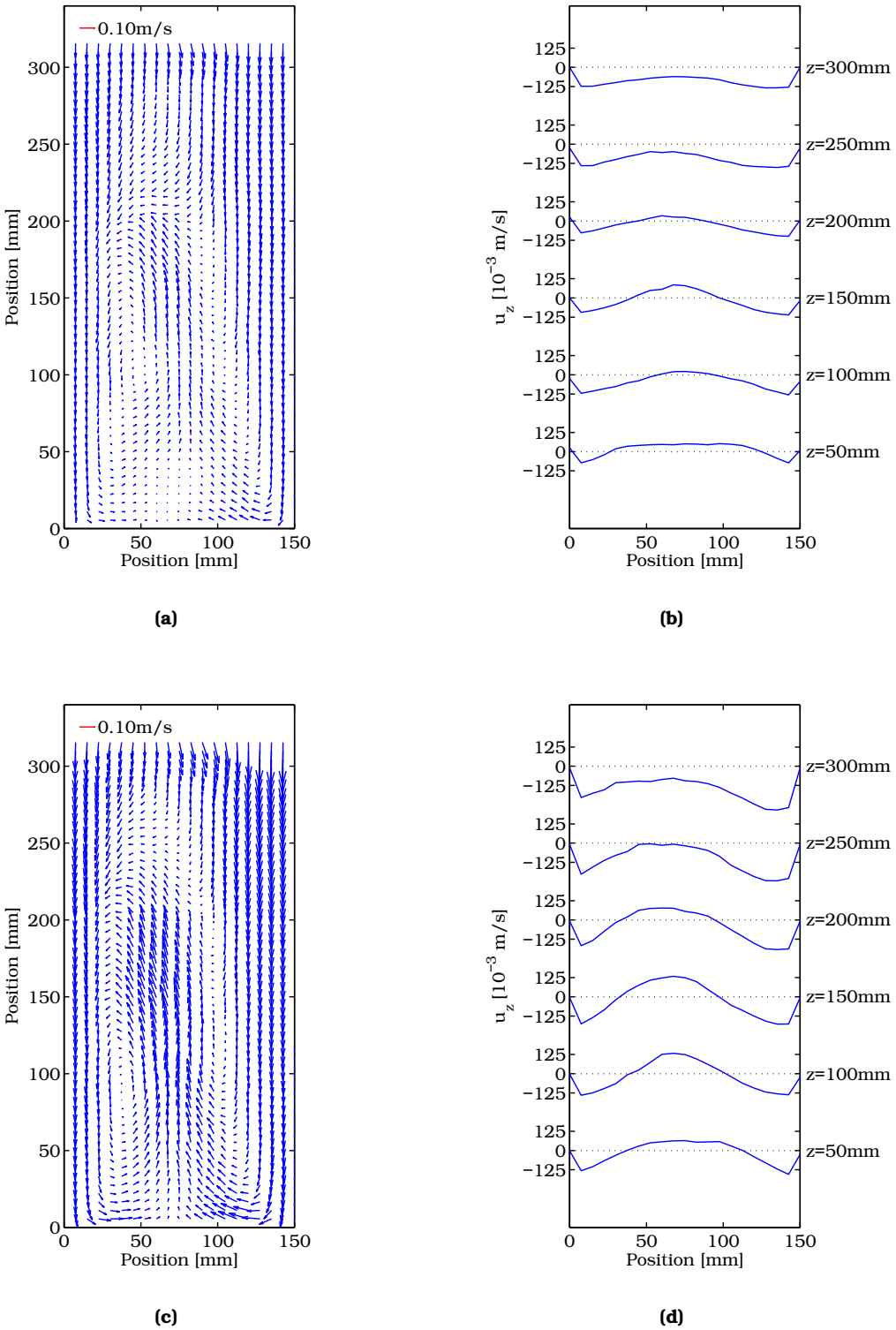

Figure C.9: Parameters: d_{bed} = 0.15 m; h_{bed} = 0.30 m; **(a)+(b)** $u_0 = 2.5u_{mf}$ **(c)+(d)** $u_0 = 3.5u_{mf}$

Appendix D

DIA results

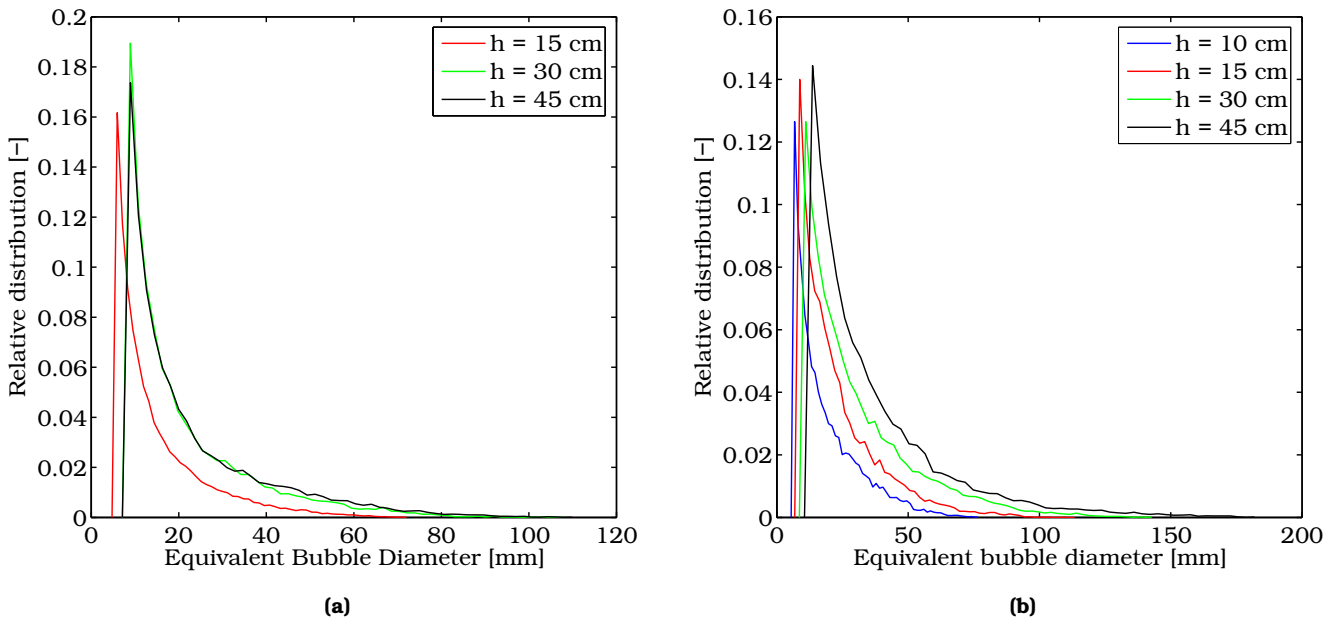

Figure D.1: Bubble diameter distribution in different bed heights. Parameters: u_0 = 2.5u_{mf}; n = 40 categories. **(a)** $d_{bed} = 0.15$ m; h_{bed} varies; **(b)** $d_{bed} = 0.30$ m; h_{bed} varies.

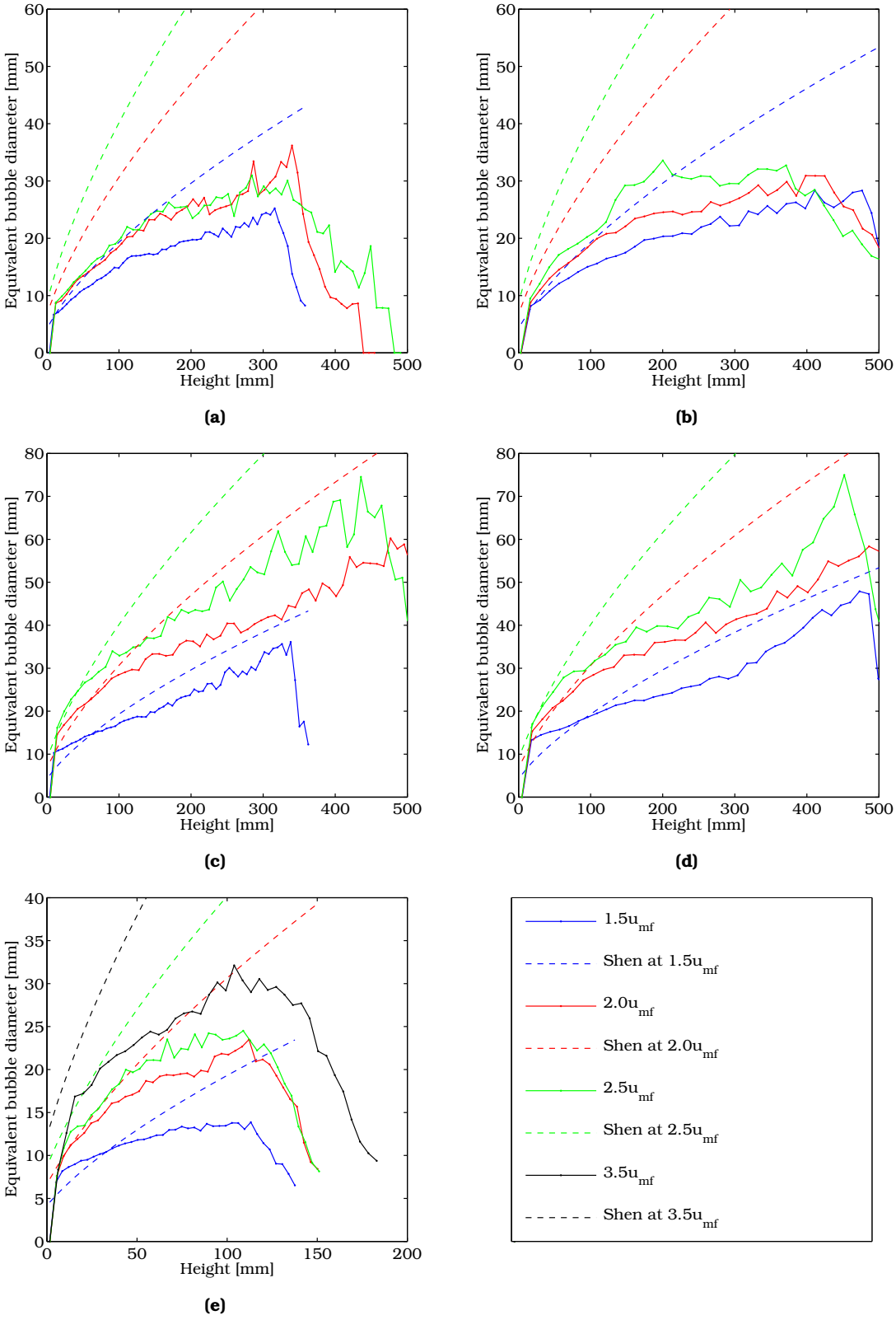

Figure D.2: The relation of Shen *et al.* is plotted with experimental data. Parameters: u_0 = 1.5,2.0,2.5 and $3.5u_{mf}$; n = 40 categories. **(a)** d_{bed} = 0.15 m; h_{bed} = 0.30 m **(b)** d_{bed} = 0.15 m; h_{bed} = 0.45 m **(c)** d_{bed} = 0.30 m; h_{bed} = 0.30 m; **(d)** d_{bed} = 0.30 m; h_{bed} = 0.45 m; **(e)** d_{bed} = 0.30 m; h_{bed} = 0.10 m.

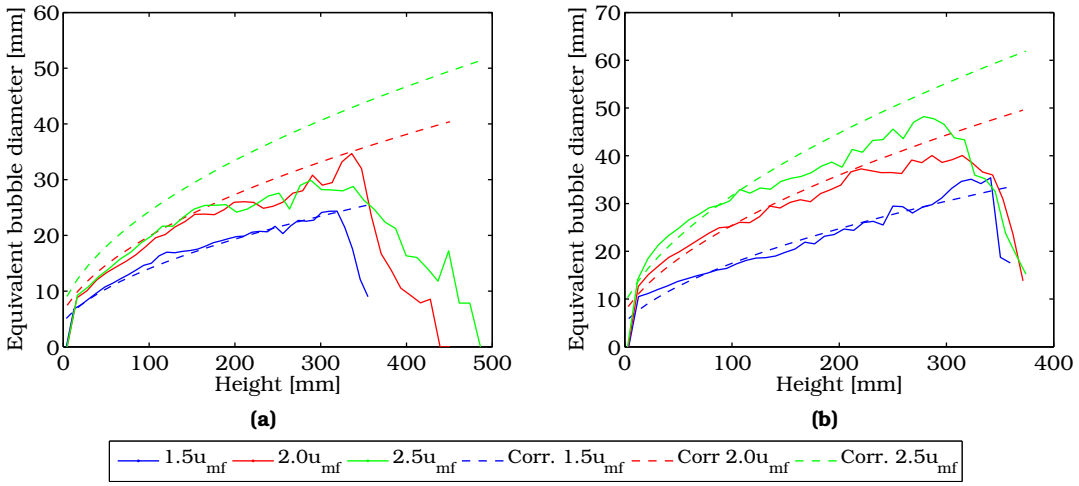

Figure D.3: The adapted Shen-correlation fits good with current experiments. The only discrepancies are found at high superficial gas velocities, probably due to restriction of the maximum bubble size. Parameters: u_0 = 1.5,2.0,2.5u_{mf}; h_{bed} = 0.30 m; n = 40 categories. **(a)** d_{bed} = 0.15 m; **(b)** d_{bed} = 0.30 m.

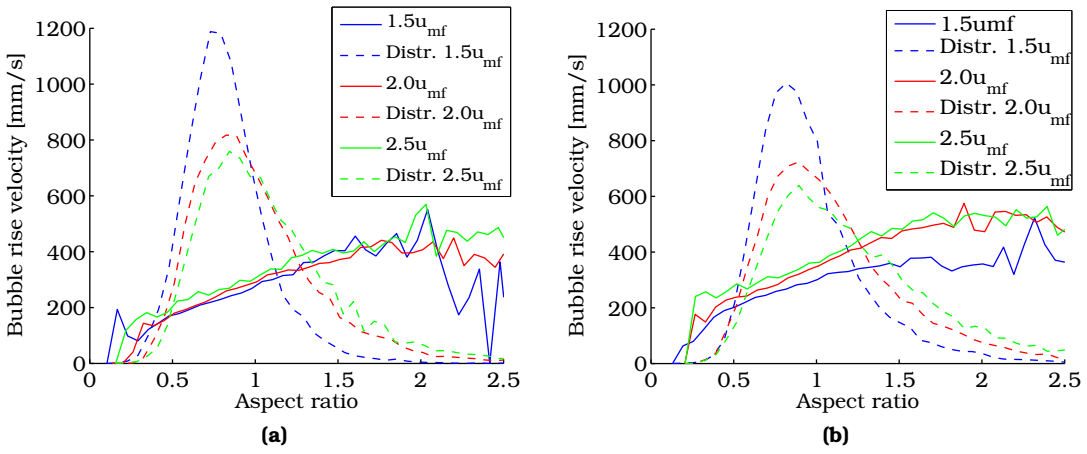

Figure D.4: Bubble rise velocity as a function of the aspect ratio, and the distribution thereof. Parameters: u_0 = 1.5,2.0,2.5u_{mf}; d_{bed} = 0.30 m; n = 80 categories. **(a)** h_{bed} = 0.15 m; **(b)** h_{bed} = 0.45 m.